STABILIZATION OF MOBILE MANIPULATORS

A Dissertation
Presented to
The Academic Faculty

By

Michael LiBretto

In Partial Fulfillment
of the Requirements for the Degree
Doctor of Philosophy in the
Woodruff School of Mechanical Engineering
Department of Mechanical Engineering

Georgia Institute of Technology

August 2021

STABILIZATION OF MOBILE MANIPULATORS

Thesis committee:

Dr. Ueda, Advisor
School of Mechanical Engineering
Georgia Institute of Technology

Dr. Ferri
School of Mechanical Engineering
Georgia Institute of Technology

Dr. Rogers
School of Aerospace Engineering
Georgia Institute of Technology

Dr. Hutchinson
School of Interactive Computing
Georgia Institute of Technology

Dr. Sadegh
School of Mechanical Engineering
Georgia Institute of Technology

Date approved: April 14, 2021

Always remember that the most important thing in a good marriage is not happiness, but stability.

Gabriel Garcia Marquez

For my chosen family; thank you all for showing me I can be more than I am.

ACKNOWLEDGMENTS

First and foremost I would like to acknowledge my PI, Dr. Jun Ueda for his tireless charge and motivation as I went through this program. Despite entering my PhD studies with no research experience, Dr. Ueda's multidisciplinary experience cultivated an encouraging environment for me to grow into the researcher I am today. I will never forget the excitement he showed in our recruitment interview and that got me through a lot of the doubts I had moving forward.

I would like to thank my reading committee; Dr. Aldo Ferri, Dr. Seth Hutchinson, Dr. Jon Rogers, and Dr. Nader Sadegh. I appreciate the avenues of inquiry they opened and the time they took from their own schedules to sit on my committee.

I would like to extend my deepest gratitude to my cohort in the Biorobotics and Human Modeling Lab for tolerating the prattling that occurred when I would hit a wall in my work and for creating a welcoming environment for someone who was not sure they would fit in. Waiman, Yingxin, Danny, Antonio, Euisun, Alex, and Rohan have all helped me in their own ways and I can never repay that. Jared Elinger, while not a member of the lab, has been an integral part in keeping on the straight and narrow during my PhD studies – thank you for not giving up on me.

To the support system I've pieced together during my time here in Atlanta: without you all I would not have made it this far. Chris Jarrette provided unofficial academic competition that was invaluable to my experience with mathematics that I can never give back. My best friends, Michelle and Zena, I am eternally grateful for the unconditional love you both have shown me.

TABLE OF CONTENTS

LIST OF TABLES

LIST OF FIGURES

SUMMARY

The focus of this work is to generate a method of stabilization in a system generated through the marriage of a mobile robot and a manipulator. While the stability of a rigid manipulator is a solved problem, upon the introduction of flexibilities into the manipulator base structure there is the simultaneous introduction of an unmodeled, induced, oscillatory disturbance to the manipulator system from the mobile base suspension and mounting. Under normal circumstances, the disturbance can be modeled through experimentation and then a form of vibration suppression control can be employed to damp the induced oscillations in the base. This approach is satisfactory for disturbances that are measured, however the hardware necessary to measure the induced oscillations in the manipulator base is generally not included in mobile manipulation systems. Because of this lack of sensing hardware it becomes difficult to directly compensate for the induced disturbances in the system. Rather than developing a direct method for compensation, efforts are made to find postures of the manipulator where the flexibilities of the system are passive. In these postures the manipulator behaves as if it is on a rigid base, this allows the use of higher feedback gains and simpler control architectures.

CHAPTER 1
MOTIVATION AND BACKGROUND

1.1 Motivation

Growth in telerobotics has increased the development of manipulators on mobile-robotic bases. While this coupling can open the door to new avenues of rescue and exploratory robotics, complications may arise from introducing unknown base parameters to the manipulator and requiring high maneuverability with a small form factor. In separating these issues into kinematic control of the mobile robot and the stability of the manipulator on the flexible base allows creates the opportunity for solving both of these issues.

As a result of the trajectory in automation, the necessity for intelligent mobile platforms has increased to match industry needs. These platforms typically fall into a category of differential drive, automobile robots with fixed wheels and steerable casters, or an omnidirectional platform [1]. While each of these has their merits, in order to satisfy the general specification of a high planar mobility while minimizing the platform's footprint, the need for omnidirectional or pseudo-omnidirectional motion arises. Optimization methods exist for stationary manufacturing equipment with transport robots within the context of robot-work cells [2], but this does not take into account the mobility of the necessary robotics.

Within the context of disaster relief, there are myriad potential health risks due to elevated radiation at a nuclear disaster site. The use of remotely operated robots for tasks such as measurement and reorganization of damaged objects at the site, instead of human responders, is a preferred option. Nuclear plant inspection robots were extensively studied back in 1980's [3]. Since then, a number of rescue and first-responder robots have been developed in a variety of forms. International Atomic Energy Agency (IAEA) hosted the first robotics competition in 2017 to promote the research and development of small ground

and surface autonomous robots that could handle safeguards inspection tools [4]. This idea extends beyond just nuclear disaster relief. Both earthquakes and hurricanes create unmodeled environments that could, depending on locale, be dangerous for humans to explore and provide relief in. To this end, the coupling between some form of mobile robot and a manipulator system becomes necessary to avoid putting a human being in a dangerous environment.

1.2 Overview

Independent of application, the necessity for stability in mobile manipulation systems is constant. Intuitive kinematics and simple control structures enable the rapid outfitting of new and existing mobile manipulation systems. For the purposes of this work, the concepts of wheeled mobile robot control (in this case just inverse kinematics) and the stabilization rigid systems that are mounted upon flexible bases (referred to hereafter as flexi-rigid systems) are decoupled. It is understood that while the base motion will affect the stability of the upper structure, in many cases the composite mobile manipulator system can be considered to be quasi-static and as such the mobile base can be considered to be a redundancy in the system.

This work will address inadequacies in inverse kinematic methods as they relate to degenerate wheeled mobile robots, and the disturbance rejection of induced oscillation in flexi-rigid systems.

1.3 Research Questions

This work aims to accomplish the following goals:

- **Aim 1:** In order to make definitive claims about the passivity of flexi-rigid systems, the normalized coprime factor (NCF)-based and the modal passivity-based stability margins are analyzed with respect to the system dynamical description these systems.

Several proofs are presented regarding the constant value of the NCF stability margin, as well as conditions to remain within a robust posture.

- **Aim 2:** In order to employ simple feedback control to manipulators with bases of unknown flexibility, modal-space and H_∞-based stability metrics are used to characterize the passivity of the base flexibility and the manipulator's robustness to induced oscillations in that flexibility. These metrics will be used to optimize the manipulator posture in order to improve closed-loop stability of the flexible, marginally-stable, open-loop plant.

- **Aim 3:** In order to prevent divergent kinematic behavior in degenerate mobile robots, a singularity-free analytical inverse kinematics method will be developed. Rather than relying on numerical accuracy in inverse matrix methods, the proposed method generates a set of equations specific to the mobile robot which do not have numerical singularity.

CHAPTER 2

LITERATURE REVIEW

2.1 Passivity-Based Control

The motivating theory behind the use of the modal passivity index and the normalized coprime factor robustness is to be able to describe the target flexible system's ability to function under high feedback gain without directly compensating for the flexibilities. At its root, passivity theory and passivity-based control can do just that. Through inherent robustness guarantees available as a result of passive systems and the small-gain theorem, it is possible to have no theoretical limit to feedback gain for the target linear system.

The small-gain theorem states that the feedback connection of two systems, $\boldsymbol{G}_1$ and

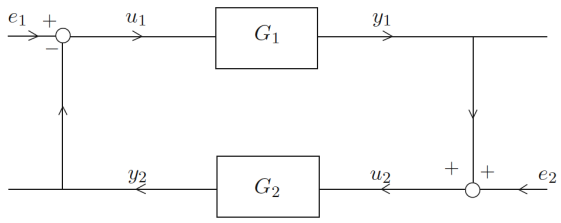

Figure 2.1: Standard feedback configuration, $\boldsymbol{G}_1 \|_f \boldsymbol{G}_2$, [5]

$\boldsymbol{G}_2$; shown in Figure 2.1 has closed-loop stability given that the product of their L_q-gains is less than 1 ($\gamma_q(\boldsymbol{G}_1)\gamma_q(\boldsymbol{G}_2) < 1$). This implies a robustness to perturbations in the feedback configuration so long as the loop-gain remains "small." Existing work has equated systems that satisfy the small-gain theorem as being passive [6, 7]. Furthermore, because these two properties are equivalent, for a perturbed system that satisfies the small-gain theorem, it should also be passive.

Whereas when a linear system is considered to be passive it is also positive real [8, 9]. Positive realness occurs when the elements of the transfer matrix of is analytic in the right half of the imaginary plane, the transfer matrix has real values for all values of s, and

the hermite sum of the transfer matrix is positive semi-definite for all values of s in the right-half plane. It should also be known that the poles of the transfer matrix are within the closed left-half plane of the s-domain.

The relationship between Lyapunov stability and passivity is also well established. Systems that are strictly passive are at least asymptotically stable about the origin. This can be easily proven by using the storage function that describes the passivity of the system as a candidate Lyapunov function. While passivity has guaranteed stability at the origin of the system, it is certainly a conservative metric and might not capture the "upper limit" of controller gain. That said, when approached from the realm of small-gain theory, one can follow this extension to determine that a pair of connected systems that satisfy the small gain theory are asymptotically stable at the origin.

Positive reality is also closely related to a system's other properties, namely the minimum-phase property. Necessarily, a positive real system will be minimum-phase [9, 10] as well as be roughly equivalent to having an in-phase property for lightly-damped flexible systems. The in-phase property is known to be advantageous as it coordinates motion of the flexible modes with the rigid mode. For an negative feedback of error in a system with out-of-phase modes the closed-loop becomes unstable as the feedback gain increases [11, 12].

The sum-total of these relationships results in a concise statement: the concepts of passivity, positive-reality, and in-phase modes all remove the theoretical upper limit of controller gain. These concepts are also intrinsically linked to the concept of normalzied coprime factor robustness which will be explored later in this work.

2.2 Vibration Suppression in End-Point Control of Flexible-Base Systems

When considering the control of a mechanical system, it is reasonable to expect that the designer might first move to employ simple feedback control and treat the system as rigid in its totality. The exclusion of modeled flexible dynamics in the system-dynamical descrip-

tion severely limits the control bandwidth due to unmodeled disturbance oscillation [13, 14]. The ability to measure these disturbances provides avenues to generate a model for the oscillations [15] and use gain scheduling or to even introduce active damping to suppress these vibrations [16]. Being able to characterize these disturbances is powerful as it opens the door to passive suppression methods (such as tuned mass-spring-damper systems [14]) or pre-compensators in control [17].

The current state of the art in vibration suppression control relies on this ability. Knowing the frequency range of the flexibility allows for the introduction of robust control and rejection of the nonlinearity in the system [18] or for the shaping of sensitivity functions in the controller [19]. Sliding mode and fuzzy controllers are also used to compensate for unknown dynamics [20, 21, 22, 23, 24, 25]. When such systems have kinematic redundancy it is also known to lever those redundancies so as to pose the system in a more robust posture. Macro-micro manipulators on flexible bases use this concept to minimize the initial excitation of oscillation [26, 27, 28, 29, 30]. In the case of redundant *manipualtor* control, it is commonplace to utilize nullspace augmentation [31, 32, 33].

2.3 Degenerate Mobile Robot Kinematics

Wheeled mobile robots (WMR) are well studied mechanical systems that contain unintegrable kinematic constraints that, overall, complicate the modeling process [34, 35, 36]. These complications give rise to multitudinous descriptors for the overall structures of these systems; namely degrees of *mobility* and *steerability*. These terms can be considered as an analogue to degrees of freedom one might see in traditional mechanism analysis and are dependent not only on the number of wheels a WMR has, but also the style of each wheel (fixed-conventional wheels, orientable conventional wheels, caster wheels, Swedish wheels, and spherical wheels; each of these has their own kinematic constraints generated through the no-slip condition). The degree of mobility is a measure of how many wheel

constraints are unsatisfied from fixed and orientable conventional wheels. Obviously, the more of these wheels that exist along different axes of rotation the overall resolvability of planar robot motion decreases. Mathematically, this exists as:

$$\delta_m = \dim \mathcal{N}\left[\boldsymbol{C}^*(\varphi_c)\right] \tag{2.1}$$

where $\boldsymbol{C}^*(\varphi_c)$ is the constraint matrix whose rows are formed from the fixed and centered-orientable conventional wheel constraints and φ_c is a vector of steering angles for each of those wheels. Because this is a planar system (with x, y, and angular velocities), the maximum $\mathrm{rank}\left[\boldsymbol{C}^*(\varphi_c)\right]$ is 3. Intuitively, the larger the nullspace of this constraint matrix is, the more directions the WMR can move immediately move given an input. The second metric, the degree of steerability is defined as the number of conventional centered-orientable wheels that may be oriented independently in order to steer the robot. This is expressed as

$$\delta_s = \mathrm{rank}\, \boldsymbol{C}_c(\varphi_c) \tag{2.2}$$

where $\boldsymbol{C}_c(\varphi_c)$ is a constraint matrix whose rows are formed from the constraints from *only* the centered-orientable conventional wheels. Reasonably, this matrix is always rank deficient and has limits of 0 and 2. When a robot designer employs more centered-orientable wheels than the degree of steerability there is a requirement that the extra wheels must be moved in concert in order to resolve motion. The sum of these two descriptors is known as the degree of *maneuverability*, $\delta_M = \delta_m + \delta_s$, $0 \leq \delta_M \geq 5$. This metric is, qualitatively, the number of degrees of freedom afforded by both the effective number of steerable wheels and the mobility that comes directly from the velocity input. Due to the structural nature of these indices, two robots may have the same overall maneuverability but have different steerability and mobility.

It is through these indices that one may descriptively term a WMR as degenerate. By defintion, degeneracy is the condition under which the posture kinematic model is rank-

deficient. Practically this resolves to the nonexistence of an instantaneous center of rotation for all given configurations of the WMR. This necessitates that all fixed-direction conventional wheels share a common axis that will not be colinear with the axes of any of the centered-orientatable conventional wheels, as well as that there are no redundant centered-orientable wheels.

The singularity of the posture-kinematic model raises the question of solvability of the robot's *inverse* kinematics. In general, the solution of WMR inverse kinematics requires first the construction of the posture kinematic model from either homogenous transform or wheel constraint methods. The resulting wheel-Jacobian is then inverted to achieve the desired inverse kinematics of the WMR [37, 38, 39, 40, 41], and these kinematics are then used with control systems to ensure proper robot motion (with necessary care for velocity singularity avoidance or management of redundancy) [42, 43, 44, 45, 46, 47]. Fundamentally this is a concise way of solving the problem of inverse kinematics, however when a robot is degenerate and has a singular posture-kinematic model that singularity prevents the inversion of the wheel Jacboian.

The structural nature of this problem has lead to discourse on wheel structures themselves [48, 49, 50, 51, 52, 53]. Generally the consensus is to limit the number of centered-orientable wheels present in the system to avoid the limiting effect on the holonomy of the platform. Instead, in order to maintain the nonholonomy and omnidirectionality of the robotic platform there is a clear advantage This, however, marginalizes the efficacy of this wheel style; for most applications where both torque transmission and load capacity are required these wheels are the superior choice [1].

CHAPTER 3

PASSIVITY OF FLEXI-RIGID SYSTEMS

3.1 Motivation

The normalized coprime factor-based stability (NCF stability or the ε_{max} metric) and the modal-space stability index (modal stability index or w_i) are both used to describe the stability of a system[54, 55], however they describe the system from two different perspectives. The former examines the system's robustness to external disturbances for all classes of feedback controller, and the latter is a measure of the system's distance from a positive-real configuration for a particular vibration mode. While these two concepts are removed from one another, it is theorized that there is an analytical relationship between the two metrics. This chapter introduces both of these metrics and analyzes their relationship.

3.2 Relationship between Normalized Coprime Factor Robustness and Manipulator Passivity

Theorem 1. *If a posture exists where the modal space stability index, $w_i = 0, \forall i = 1...m$, the manipulator's flexible dynamics are passive, and the NCF stability margin will indicate that the total system will perform at least as well as the rigid system. Furthermore, all double-integrator (rigid) systems share the same NCF stability margin.*

The above statement hinges on the following predicates:

1. The theorem requires that the posture have all of its modal stability indices are 0.
2. The value of the NCF stability margin for the flexible manipulator in this posture is at greater than or equal to the NCF stability margin for the system's rigid mode.
3. This value of the NCF stability margin is known for rigid systems.

3.3 The Modal Stability Index and Determination of Robust Arm Configurations

The first predicate of Theorem 1 requires the manipulator to be in a posture with all modal space stability indices, $w_i, \forall i$, to be identically 0; this is a robust arm configuration (RAC, or just a robust configuration when considering systems that are not robot arms).

3.3.1 System Model

The linearized dynamics of the manipulator system that contains m lightly-damped flexibilities and n rigid components in a task-space with d dimensions can be described by the second order differential equation:

$$\boldsymbol{M}(\boldsymbol{q})\ddot{\boldsymbol{q}} + \boldsymbol{D}\dot{\boldsymbol{q}} + \boldsymbol{K}(\boldsymbol{q}) = \boldsymbol{\tau} \in \mathbb{R}^{m+n} \tag{3.1}$$

where $\boldsymbol{M}(\boldsymbol{q})$, $\boldsymbol{D}$, and $\boldsymbol{K}$ are symmetric mass, viscosity, and stiffness matrices. The system posture, $\boldsymbol{q}$, is a collection of positions of each of the joints in the system and is partitioned such that $\boldsymbol{q} = \left[\boldsymbol{q}_p^T,\ \boldsymbol{q}_a^T\right]^T \in \mathbb{R}^{m+n}$. Here, $\boldsymbol{q}_p$ is a position vector containing the displacements or angles of the passive joints in the system and $\boldsymbol{q}_p$ is a position vector containing the displacements and angles for the active (driven) joints in the composite system. The partition of joint states induces a similar partition in the torque vector $\boldsymbol{\tau}$. The torque vector can be described by:

$$\boldsymbol{\tau} = \boldsymbol{S}\boldsymbol{T}(\boldsymbol{q})\boldsymbol{f} \tag{3.2}$$

where $\boldsymbol{f} \in \mathbb{R}^d$ is the force command in the task space, $\boldsymbol{T}(\boldsymbol{q}) \in \mathbb{R}^{n\times d}$ is the map between the task space and the joint space, and $\boldsymbol{S} \in \mathbb{R}^{(m+n)\times n}$ is a selection matrix to apply the joint-space input command to the appropriate joints, $\boldsymbol{q}_a$.

Considering a state-space system derived from the above dynamics using the state vector $\boldsymbol{x} = \left[\boldsymbol{q}^T,\ \dot{\boldsymbol{q}}^T\right]^T$. The resulting system has the representation (for conciseness the func-

tional dependence on $\boldsymbol{q}$ may be omitted):

$$\boldsymbol{A} = \begin{bmatrix} \boldsymbol{O}_{m+n} & \boldsymbol{I}_{m+n} \\ -\boldsymbol{M}^{-1}\boldsymbol{K} & -\boldsymbol{M}^{-1}\boldsymbol{D} \end{bmatrix} \in \mathbb{R}^{2(m+n)\times 2(m+n)} \tag{3.3}$$

$$\boldsymbol{B} = \begin{bmatrix} \boldsymbol{O}_{(m+n)\times d} \\ \boldsymbol{M}^{-1}\boldsymbol{S}\boldsymbol{T} \end{bmatrix} \in \mathbb{R}^{2(m+n)\times d} \tag{3.4}$$

$$\boldsymbol{C} = \begin{bmatrix} \boldsymbol{J}_{tot}(\boldsymbol{q}) & \boldsymbol{O} \end{bmatrix} \in \mathbb{R}^{d\times 2(m+n)} \tag{3.5}$$

with output $\boldsymbol{y} = \boldsymbol{C}\boldsymbol{x}$. In the matrix $\boldsymbol{C}$, $\boldsymbol{J}_{tot}$ is the manipulator Jacobian including the flexibilities in the system.

Through Jordan decomposition of the $\boldsymbol{A}$ matrix (namely $\boldsymbol{V}\boldsymbol{A}\boldsymbol{U} = \mathbf{J}$, where $\boldsymbol{V} = \boldsymbol{U}^{-1}$) it is possible to retrieve each of the spectral projectors for the system $\boldsymbol{\Omega}_j = \boldsymbol{u}_j\boldsymbol{v}_j,\ \forall\lambda_j\ j = 2n, \ldots, 2(m+n)-1$. $\boldsymbol{u}_j$ and $\boldsymbol{v}_j$ are the j^{th} columns and rows of $\boldsymbol{U}$ and $\boldsymbol{V}$ respectively. Given the partial fraction expansion of the manipulator system:

$$\boldsymbol{G}(s,\boldsymbol{q}) = \frac{\boldsymbol{R}_0(\boldsymbol{q})}{s^2} + \sum_{j=2n}^{2(m+n)-1} \frac{\boldsymbol{\rho}_j(\boldsymbol{q})}{s-\lambda_j} \tag{3.6}$$

$$\boldsymbol{R}_0(\boldsymbol{q}) = \boldsymbol{C}\left(\sum_{i=0}^{n-1} \boldsymbol{u}_{2i}\boldsymbol{v}_{2i+1}\right)\boldsymbol{B} \tag{3.7}$$

$$\boldsymbol{\rho}_j(\boldsymbol{q}) = \boldsymbol{C}\boldsymbol{\Omega}_j\boldsymbol{B} \tag{3.8}$$

Through the modal analysis we can represent the same transfer function as a linear combination of the rigid and flexible modes:

$$\boldsymbol{G}(s,\boldsymbol{q}) = \frac{\boldsymbol{R}_0(\boldsymbol{q})}{s^2} + \sum_{i=1}^{m} \frac{\boldsymbol{R}_i(\boldsymbol{q})}{s^2 + 2\zeta_i\omega_{ni}s + \omega_{ni}^2} \tag{3.9}$$

with ζ_i as the damping coefficient of the i^{th} flexible mode and ω_{ni} is its natural (resonant) frequency. Being that the two above constructions should be equivalent, comparing the two

yields:

$$\frac{\boldsymbol{R}_i(\boldsymbol{q})}{s^2 + 2\zeta_i\omega_{ni}s + \omega_{ni}^2} = \frac{\boldsymbol{\rho}_{2j}(\boldsymbol{q})}{s - \lambda_{2j}} + \frac{\boldsymbol{\rho}_{2j+1}(\boldsymbol{q})}{s - \lambda_{2j+1}} \tag{3.10}$$

insofar as the i^{th} mode, λ_i, is equal to λ_{2j} and its conjugate $\bar{\lambda}_i$ is equal to λ_{2j+1}. Expanding the above equality yields:

$$\frac{\boldsymbol{R}_i(\boldsymbol{q})}{s^2 + 2\zeta_i\omega_{ni}s + \omega_{ni}^2} = \boldsymbol{C}\frac{s(\boldsymbol{\Omega}_{2j} + \boldsymbol{\Omega}_{2j+1}) - \lambda_{2j}\boldsymbol{\Omega}_{2j} - \lambda_{2j+1}\boldsymbol{\Omega}_{2j+1}}{(s - \lambda_{2j})(s - \lambda_{2j+1})}\boldsymbol{B} \tag{3.11}$$

The modulus of s is a constant 0 due to the structural properties of the sum $(\boldsymbol{\Omega}_{2j} + \boldsymbol{\Omega}_{2j+1})$ in the product $\boldsymbol{C}(\boldsymbol{\Omega}_{2j} + \boldsymbol{\Omega}_{2j+1})\boldsymbol{B}$ yielding 0. Therefore the equality resolves to:

$$\frac{\boldsymbol{R}_i(\boldsymbol{q})}{s^2 + 2\zeta_i\omega_{ni}s + \omega_{ni}^2} = -\boldsymbol{C}\frac{\lambda_{2j}\boldsymbol{\Omega}_{2j} + \lambda_{2j+1}\boldsymbol{\Omega}_{2j+1}}{(s - \lambda_{2j})(s - \lambda_{2j+1})}\boldsymbol{B} \tag{3.12}$$

ultimately yielding that $\boldsymbol{R}_i(\boldsymbol{q}) = -2\Re\left(\bar{\lambda}_i\boldsymbol{C}\boldsymbol{\Omega}_i\boldsymbol{B}\right)$ (adapted from [12]).

3.3.2 Modal Stability Index

For a manipulator system describable by the formulation in the preceding section, it may be represented as an MIMO transfer function of the form:

$$\boldsymbol{G}(s, \boldsymbol{q}) = \frac{\boldsymbol{R}_0(\boldsymbol{q})}{s^2} + \sum_i^m \frac{\boldsymbol{R}_i(\boldsymbol{q})}{s^2 + 2\zeta_i\omega_{ni}s + \omega_{ni}^2} \in \mathbb{C}^{d\times d} \tag{3.13}$$

$$\boldsymbol{R}_0(\boldsymbol{q}) = \boldsymbol{J}_v(\boldsymbol{q})\hat{\boldsymbol{M}}(\boldsymbol{q})^{-1}\boldsymbol{T}(\boldsymbol{q}) \in \mathbb{R}^{d\times d} \tag{3.14}$$

$$\boldsymbol{R}_i(\boldsymbol{q}) = -2\Re\left(\bar{\lambda}_i\boldsymbol{C}\boldsymbol{\Omega}_i\boldsymbol{B}\right) \in \mathbb{R}^{d\times d} \tag{3.15}$$

where: $\boldsymbol{R}_0(\boldsymbol{q})$ and $\boldsymbol{R}_i(\boldsymbol{q})$ are the rigid and i^{th} flexible mode (residual) respectively; ζ_i is the damping coefficient of the i^{th} flexible mode and ω_{ni} is its natural (resonant) frequency. The variable d represents the dimension of the space the system lies in ($d = 1$ is a linear space, $d = 2$ is a planar space, etc). $\boldsymbol{J}_v$ is the "rigid" Jacobian of the flex-rigid system, $\hat{\boldsymbol{M}}(\boldsymbol{q})^{-1}$ is the rigid portion of the inverse of the inertia matrix for the system, and $\boldsymbol{T}(\boldsymbol{q})$ is the map

between the task-space and the state-space. Lastly, $\bar{\lambda}_i$ is the conjugate of the eigenvalue associated with the i^{th} mode, Ω_i is the spectral projector for the i^{th} flexible mode.

The modal stability index, w_i is defined as [54]:

$$w_i = \lambda_{min}(\mathbf{R}_i + \mathbf{R}_i^T) \leq 0 \tag{3.16}$$

These measures indicate the distance from the current robot configuration to a robust arm configuration (RAC) [54]. A robust arm configuration is a joint configuration $\mathbf{q}$ which satisfies $w_i = 0$. The linearized system in this configuration is positive real, and therefore passive. In this posture, the residual must satisfy [54]:

$$\boldsymbol{R}_i = \boldsymbol{R}_i^T \tag{3.17}$$

$$\boldsymbol{R}_i \succcurlyeq 0 \tag{3.18}$$

Knowing this, the stability index in that posture becomes $w_i^{RAC} = \lambda_{min}(2R_i)$.

3.3.3 Locating Robust Postures

For ease of analysis, the elements of the residual will be broken into blocks such that:

$$\hat{\boldsymbol{B}} = \boldsymbol{M}^{-1}\boldsymbol{S}\boldsymbol{T} = \begin{bmatrix} | & & | & & | \\ \boldsymbol{b}_1 & , \cdots , & \boldsymbol{b}_k & , \cdots , & \boldsymbol{b}_d \\ | & & | & & | \end{bmatrix} \tag{3.19}$$

$$\hat{\boldsymbol{C}} = \boldsymbol{J}_{tot} = \begin{bmatrix} — & \boldsymbol{c}_1 & — \\ & \vdots & \\ — & \boldsymbol{c}_j & — \\ & \vdots & \\ — & \boldsymbol{c}_d & — \end{bmatrix} \tag{3.20}$$

$$\boldsymbol{\Omega}_i = \begin{bmatrix} \boldsymbol{\Omega}_1 & \boldsymbol{\Omega}_2 \\ \boldsymbol{\Omega}_3 & \boldsymbol{\Omega}_4 \end{bmatrix} \tag{3.21}$$

Assuming $\boldsymbol{B} = [\boldsymbol{0}^T,\ \hat{\boldsymbol{B}}^T]^T$ and $\boldsymbol{C} = [\hat{\boldsymbol{C}},\ \boldsymbol{0}]$, the residual can be rewritten as:

$$R_i = -2\Re\left(\bar{\lambda}_i \begin{bmatrix} \boldsymbol{c}_1\boldsymbol{\Omega}_2\boldsymbol{b}_1 & \cdots & \boldsymbol{c}_1\boldsymbol{\Omega}_2\boldsymbol{b}_d \\ \vdots & \ddots & \vdots \\ \boldsymbol{c}_d\boldsymbol{\Omega}_2\boldsymbol{b}_1 & \cdots & \boldsymbol{c}_d\boldsymbol{\Omega}_2\boldsymbol{b}_d \end{bmatrix}\right) \tag{3.22}$$

Expansion of each term has shown that each of the terms in the matrix can be represented as:

$$[\boldsymbol{R}_i]_{jk} = -2\Sigma\Sigma\left[(\boldsymbol{b}_k\boldsymbol{c}_j)^T \circ \Re(\bar{\lambda}_i\boldsymbol{\Omega}_2)\right] \tag{3.23}$$

The symmetry condition from (Equation 3.18) obviously requires that $\boldsymbol{b}_k\boldsymbol{c}_j = \boldsymbol{b}_j\boldsymbol{c}_k$ for all pairs of j and k. The positive semi-definite condition requires a 0-minimum eigenvalue of $\boldsymbol{R}_i$ which is only possible should the $\det(\boldsymbol{R}_i) = 0$. This comes from the general form of a matrix characteristic polynomial:

$$\mathrm{p}_{\boldsymbol{R}_i}(X) = \prod_i^d (X - \lambda_i) = X^d + \cdots + \prod_i^d (\lambda_i) \tag{3.24}$$

$$\det(\boldsymbol{R}_i) = \prod_i^d (\lambda_i) \tag{3.25}$$

where λ_i is an eigenvalue of $\boldsymbol{R}_i$. In addition, by [56, 57], all principal minors of $\boldsymbol{R}_i$ must be nonnegative for the residual to be positive semidefinite.

Remark. *As a result of the above analysis, it has been shown that C and/or B must be rank deficient in order for the manipulator posture to be an RAC. These correspond to uncontrollable and observable conditions on the flexible modes of the system.*

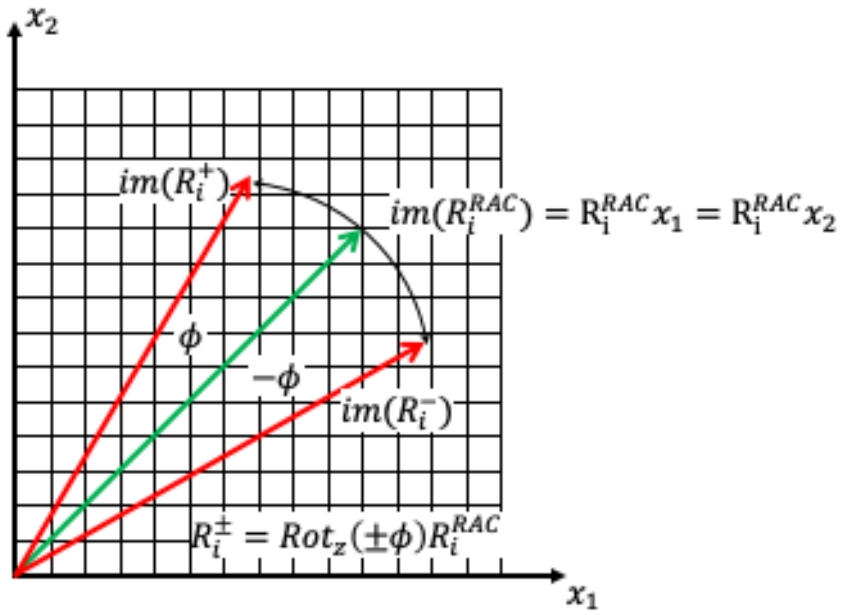

Figure 3.1: Visualization of the angular perturbation of the residual in the plane

3.3.4 Remaining in a Robust Posture

It is reasonable to expect that once a system enters a passive posture it would be desirable to stay in a passive posture. Being that the modal passivity index has no dependence on the rigid mode, one might consider only a small perturbation in residual. This perturbation is additive in the flexible mode such that:

$$\boldsymbol{G}'(s) = \boldsymbol{G}(s) + \sum_{i=1}^{m} \frac{\boldsymbol{\Delta R}_i}{s^2 + 2\zeta_i \omega_{ni} s + \omega_{ni}^2} \tag{3.26}$$

$$\boldsymbol{\Delta R}_i = (\mathrm{rot_z}(\phi_i) - \boldsymbol{I}_d)\boldsymbol{R}_i \tag{3.27}$$

It is understood that while the rigid mode will also change with the system's posture, the change can be considered negligible in this context.

The perturbation of the residual, $\boldsymbol{R'}_i$, can be abstractly visualized as a rotation of $\mathrm{image}(\boldsymbol{R}_i)$ in the plane, shown in Figure 3.1. The domain of the transfer functions discussed in this work is the task-space of the manipulator, and the rank of the residual ($\mathrm{rank}(\boldsymbol{R}_i) = 1$) implies that the image forms the span of a line in this space. The rota-

tion of matrix's image is equivalent to the rotation of the residual due to the linearity of the image function. For mathematical convenience, in order to introduce the concept of a residual perturbation, the rotational perturbation will be discussed. The effect of rotating the residual away from the robust posture is shown in Figure 3.2 for a planar system. The two eigenvalues are the spectra of the residual after a rotation by ϕ. Obviously, these postures are not robust as the minimum eigenvalue (the lower curve) moves away from 0.

This can be extended to a spatial manipulator by using rotation matrices about the normal and bi-normal vectors for the image of the residual. The planar case can use the general rotational formalism for the "z" direction, however when the residual spans a line in 3-space, in order to decompose the rotational perturbation into convenient matrices, two vectors normal to the span of the residual must be described. These are the normal and bi-normal vectors of the residual and lie within the plane that is described by the span of the residual.

In order to classify the structure of perturbations that are allowable to remain at a robust posture, the spectra of the perturbed residual must be analyzed. The proceeding analysis is conducted for a planar manipulator system, but can be extended to a manipulator in $\mathbb{R}^3$.

Theorem 2. *A rigid manipulator on a flexible base can remain in a robust arm posture for a subset of all perturbations in its point of linearization.*

Proof. Beginning with the classic eigenvalue problem, we find the spectra of a perturbed Hermite matrix $\boldsymbol{H}_i = 2\boldsymbol{R}_i^{RAC}$ for a particular perturbation that maintains the RAC condition: $\boldsymbol{\Delta H}_i = 2\boldsymbol{\Delta R}_i$. If the original spectra of $\boldsymbol{H}_i$ is denoted by λ with unit eigenvectors, $\boldsymbol{v}$ that form an orthornomal basis of the eigenspace, then the perturbations made to the eigenvalues and eigenvectors can be denoted by $\delta\lambda$ and $\boldsymbol{\delta v}$ respectively. The resulting problem formulation becomes:

$$(\boldsymbol{H}_i + \boldsymbol{\Delta H}_i)(\boldsymbol{v}_j + \boldsymbol{\delta v}_j) = (\lambda_j + \delta\lambda_j)(\boldsymbol{v}_j + \boldsymbol{\delta v}_j) \tag{3.28}$$

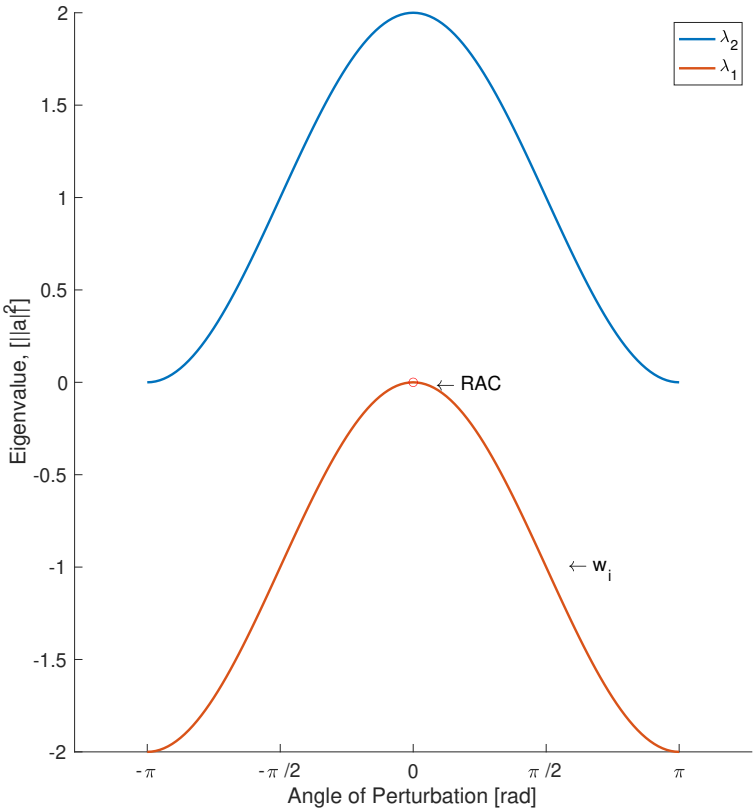

Figure 3.2: Perturbation of residual by rotation for d=2. Eigenvalues normalized by length of generating vector, a

Expanding the above expression and removing second order terms (they are typically very small), the eigenvalue problem becomes:

$$\boldsymbol{\Delta H}_i \boldsymbol{v}_j + \boldsymbol{H}_i \boldsymbol{\delta v}_j = \delta\lambda_j \boldsymbol{v}_j + \lambda_j \boldsymbol{\delta v}_j \tag{3.29}$$

The perturbation in eigenvector can be represented in the basis spanned by the orthogonal, original eigenvectors. After some manipulation, the resulting eigenvalue perturbation is:

$$\lambda'_j = \lambda_j + \frac{\boldsymbol{v}_j^T \boldsymbol{\Delta H}_i \boldsymbol{v}_j}{\boldsymbol{v}_j^T \boldsymbol{v}_j} \tag{3.30}$$

Utilizing this it becomes possible to generate restrictions on $\boldsymbol{\Delta H}_i$ (and therefore on $\boldsymbol{\Delta R}_i$). The original spectra of $\boldsymbol{H}_i$ is $\lambda = \{0, 2\rho^2(\alpha^2+1\}$ with $\rho, \alpha \in \mathbb{R}$ with corresponding eigenvectors, $\boldsymbol{v} = \left\{[-\alpha, 1]^T, [1/\alpha, 1]^T\right\}$.

Looking first at the 0 eigenvalue, the resulting perturbed eigenvalue should be

$$\lambda'_1 = \frac{\boldsymbol{v}_1^T \boldsymbol{\Delta H}_i \boldsymbol{v}_1}{\boldsymbol{v}_1^T \boldsymbol{v}_1} = 0 \implies \langle \boldsymbol{v}_1, \boldsymbol{\Delta H}_i \boldsymbol{v}_1 \rangle = 0 \tag{3.31}$$

This implies either orthogonality between $\boldsymbol{v}_1$ and $\boldsymbol{\Delta H}_i \boldsymbol{v}_1$ or that $\boldsymbol{v}_1$ lies within the nullspace of $\boldsymbol{\Delta H}_i$. The second eigenvalue gives a condition on the structure of $\boldsymbol{\Delta H}_i$. For the perturbed system to still be in a robust configuration, the second eigenvalue must satisfy

$$\lambda'_2 = 2\rho^2(\alpha^2+1) + \frac{\boldsymbol{v}_2^T \boldsymbol{\Delta H}_i \boldsymbol{v}_2}{\boldsymbol{v}_2^T \boldsymbol{v}_2} \geq 0 \tag{3.32}$$

in order to maintain the positive semi-definiteness of the residual at a robust posture. Noticing that the second eigenvalue is $2\|\boldsymbol{a}\|^2$, where $\boldsymbol{a}$ is the vector used to construct the residual at the robust configuration, the inequality becomes

$$-2\|\boldsymbol{a}\|^2 \leq \frac{\boldsymbol{v}_2^T \boldsymbol{\Delta H}_i \boldsymbol{v}_2}{\boldsymbol{v}_2^T \boldsymbol{v}_2} \tag{3.33}$$

$$-2\|\boldsymbol{a}\|^2 \leq \frac{\lambda_{min}(\boldsymbol{\Delta H}_i)\|v_2\|^2}{v_2^T v_2} \leq \frac{\boldsymbol{v}_2^T \boldsymbol{\Delta H}_i \boldsymbol{v}_2}{\boldsymbol{v}_2^T \boldsymbol{v}_2} \tag{3.34}$$

$$-2\|\boldsymbol{a}\|^2 \leq \lambda_{min}(\boldsymbol{\Delta H}_i) \leq \frac{\boldsymbol{v}_2^T \boldsymbol{\Delta H}_i \boldsymbol{v}_2}{\boldsymbol{v}_2^T \boldsymbol{v}_2} \tag{3.35}$$

This inequality gives an lower bound on the spectra of $\boldsymbol{\Delta H}_i$; combined with the inner-product condition from (Equation 3.31) there are now two conditions upon $\boldsymbol{\Delta H}_i$.

Being that the matrix $\boldsymbol{H} + \boldsymbol{\Delta H}_i$ is still a residual of a flexible mode, its guaranteed to have one positive eigenvalue in addition to its lower eigenvalue of 0. Therefore, the second condition on $\boldsymbol{\Delta H}_i$ is intrinsically satisfied and the only condition needed to be satisfied is the inner product of the eigenvector $\boldsymbol{v}_1$ with the perturbation due to the residual, $\boldsymbol{\Delta H}_i \boldsymbol{v}_1$. ■

Remark. *The above theorem requires the use of* $\boldsymbol{v}_1$*, the eigenvector associated with the* 0 *eigenvalue. The resulting contour of where the inner product condition equals* 0*, generally, runs parallel to the curve of maximum modal passivity in the manipulator workspace. If the inner product condition is evaluated erroneously with the* other *eigenvector, the resulting* 0 *contour will be* perpendicular *to the robust postures due to the orthogonal basis spanned by eigenvectors.*

3.4 Normalized Coprime Factor Robustness and its Value for Rigid Systems

3.4.1 The NCF Stability Margin

The focus of discussion is the NCF stability margin [58, 59]. This metric is used to measure the ability for a perturbed plant system to remain stable for all classes of stabilizing controller. In most texts, this metric is defined as:

$$\varepsilon_{max} = \sqrt{1 - \left\| \left[\tilde{\boldsymbol{N}}, \tilde{\boldsymbol{M}} \right] \right\|_H} \tag{3.36}$$

with a similar definition given in Appendix A. Here, the matrices $\tilde{\boldsymbol{N}}$ and $\tilde{\boldsymbol{M}}$ are the normalized left coprimse factors of the plant system being analyzed. This definition of the NCF stability margin takes the Hankel norm of the normalized left coprime factors (NLCF) of the target plant system. The Hankel norm [60], denoted by $\|\bullet\|_H$, is a measure of how much energy (in an H_∞ sense) from past inputs gets passed to future output, and is equal to the largest Hankel singular value of the target minimal state-space system, σ_1. The Hankel singular values [61] are defined as $\sigma_i \triangleq \sqrt{\lambda_i(\boldsymbol{PQ})}$ where $\boldsymbol{P}$ and $\boldsymbol{Q}$ are the controllability and observability Gramians of a stable plant system with balanced state-space realization, and $\lambda_i(\boldsymbol{PQ})$ is used to denote the i^{th} eigenvalue of the product $\boldsymbol{PQ}$.

While the definition in (Equation 3.36) is valid, computing the NLCF of the plant system can be computationally intensive. Equivalent formulations exist in the form of [55]:

$$\left\| \left[\tilde{\boldsymbol{N}}, \tilde{\boldsymbol{M}} \right] \right\|_H = \lambda_{max}(\boldsymbol{PQ}) = \lambda_{max}(\boldsymbol{ZX}(\boldsymbol{I} + \boldsymbol{ZX})^{-1}) \tag{3.37}$$

making ε_{max}, after some manipulation,

$$\varepsilon_{max} = \frac{1}{\sqrt{1 + \lambda_{max}(\boldsymbol{ZX})}} \tag{3.38}$$

$\boldsymbol{Z}$ and $\boldsymbol{X}$ in (Equation 3.38) are the solutions to the Generalized Filtering Algebraic Riccati Equation (GFARE) and the Generalized Controllability Algebraic Riccati Equation (GCARE) respectively [55]. These equations, in their full form are expressed as:

$$\begin{aligned}(\boldsymbol{A} - \boldsymbol{BS}^{-1}\boldsymbol{D}^*\boldsymbol{C})^*\boldsymbol{X} + \boldsymbol{X}(\boldsymbol{A} - \boldsymbol{BS}^{-1}\boldsymbol{D}^*\boldsymbol{C}) \\ - \boldsymbol{XBS}^{-1}\boldsymbol{B}^*\boldsymbol{X} + \boldsymbol{C}^*\boldsymbol{\Gamma}^{-1}\boldsymbol{C} = \boldsymbol{0}\end{aligned} \tag{3.39}$$

$$\begin{aligned}(\boldsymbol{A} - \boldsymbol{BD}^*\boldsymbol{\Gamma}^{-1}\boldsymbol{C})\boldsymbol{Z} + \boldsymbol{Z}(\boldsymbol{A} - \boldsymbol{BD}^*\boldsymbol{\Gamma}^{-1}\boldsymbol{C})^* \\ - \boldsymbol{ZC}^*\boldsymbol{\Gamma}^{-1}\boldsymbol{CZ} + \boldsymbol{BS}^{-1}\boldsymbol{B}^* = \boldsymbol{0}\end{aligned} \tag{3.40}$$

3.4.2 Evaluating the NCF Stability Margin a General Rigid System

Theorem 3. *For a rigid system with no flexible modes ($d \geq 2, m = 0$), the value of the NCF stability margin takes on a specific value for all configurations of the system.*

Proof. The generalized rigid system is given by:

$$\boldsymbol{G}(s, \boldsymbol{q}) = \frac{\boldsymbol{R}_0}{s^2} \iff \boldsymbol{P}_s(\boldsymbol{q}) = (\boldsymbol{A}, \boldsymbol{B}, \boldsymbol{C}, \boldsymbol{D}) \tag{3.41}$$

$$\boldsymbol{A} = \begin{bmatrix} \mathbf{0}_d & \boldsymbol{I}_d \\ \mathbf{0}_d & \mathbf{0}_d \end{bmatrix} \in \mathbb{R}^{2d \times 2d} \tag{3.42}$$

$$\boldsymbol{B} = \begin{bmatrix} \mathbf{0}_d \\ \boldsymbol{F}\boldsymbol{R}_0(\boldsymbol{q}) \end{bmatrix} \in \mathbb{R}^{2d \times d} \tag{3.43}$$

$$\boldsymbol{C} = \begin{bmatrix} \boldsymbol{F}^{-1} & \mathbf{0}_d \end{bmatrix} \in \mathbb{R}^{d \times 2d} \tag{3.44}$$

$$\boldsymbol{D} = \mathbf{0}_d \tag{3.45}$$

The matrix $\boldsymbol{F} \in \mathbb{R}^{d \times d}$ (invertible) is used to decompose the rigid mode between the input and output sides of the system for state space realization. Because the $\boldsymbol{D}$ matrix is $\mathbf{0}$, both the $\boldsymbol{\Gamma}$ and $\boldsymbol{S}$ are identity. This makes the GCARE (Equation 3.39) and GFARE (Equation 3.40)

$$\boldsymbol{A}^*\boldsymbol{X} + \boldsymbol{X}\boldsymbol{A} - \boldsymbol{X}\boldsymbol{B}\boldsymbol{B}^*\boldsymbol{X} + \boldsymbol{C}^*\boldsymbol{C} = \mathbf{0} \tag{3.46}$$

$$\boldsymbol{A}\boldsymbol{Z} + \boldsymbol{Z}\boldsymbol{A}^* - \boldsymbol{Z}\boldsymbol{C}^*\boldsymbol{C}\boldsymbol{Z} + \boldsymbol{B}\boldsymbol{B}^* = \mathbf{0} \tag{3.47}$$

While these are matrix equations, the system in (Equation 3.41) can remain partitioned in block-form during evaluation. This enables the assumption that the solutions to the above

equations, $\boldsymbol{X}$ and $\boldsymbol{Z}$, are symmetric and defined blockwise as

$$\boldsymbol{X} = \begin{bmatrix} \boldsymbol{X}_1 & \boldsymbol{X}_2 \\ \boldsymbol{X}_2^T & \boldsymbol{X}_3 \end{bmatrix}, \ \boldsymbol{Z} = \begin{bmatrix} \boldsymbol{Z}_1 & \boldsymbol{Z}_2 \\ \boldsymbol{Z}_2^T & \boldsymbol{Z}_3 \end{bmatrix} \tag{3.48}$$

Substituting the rigid-manipulator model, Equations (Equation 3.42)-(Equation 3.45), into (Equation 3.46), the result is the following system of matrix equations:

$$\boldsymbol{X}_2 \boldsymbol{F} \boldsymbol{R}_0 \boldsymbol{R}_0^T \boldsymbol{F}^T \boldsymbol{X}_2^T = \boldsymbol{F}^{-T} \boldsymbol{F}^{-1} \tag{3.49}$$

$$\boldsymbol{X}_1 - \boldsymbol{X}_3 \boldsymbol{F} \boldsymbol{R}_0 \boldsymbol{R}_0^T \boldsymbol{F}^T \boldsymbol{X}_2^T = \boldsymbol{0} \tag{3.50}$$

$$\boldsymbol{X}_1 - \boldsymbol{X}_2 \boldsymbol{F} \boldsymbol{R}_0 \boldsymbol{R}_0^T \boldsymbol{F}^T \boldsymbol{X}_3 = \boldsymbol{0} \tag{3.51}$$

$$\boldsymbol{X}_2^T + \boldsymbol{X}_2 - \boldsymbol{X}_3 \boldsymbol{F} \boldsymbol{R}_0 \boldsymbol{R}_0^T \boldsymbol{F}^T \boldsymbol{X}_3 = \boldsymbol{0} \tag{3.52}$$

Being that this set of equations is quadratic, it is not always possible to generate a unique solution, however, a positive definite, Hermitian stabilizing solution is guaranteed for the GCARE (GFARE) if the system is both stable and controllable (detectable) [55]. Beginning this process by solving for $\boldsymbol{X}_2$:

$$\begin{aligned} \boldsymbol{X}_2 \boldsymbol{F} \boldsymbol{R}_0 \boldsymbol{R}_0^T \boldsymbol{F}^T \boldsymbol{X}_2^T &= \boldsymbol{F}^{-T} \boldsymbol{F}^{-1} \\ \boldsymbol{X}_2 \boldsymbol{F} (\boldsymbol{R}_0 \boldsymbol{R}_0^T)^{\frac{1}{2}} (\boldsymbol{R}_0 \boldsymbol{R}_0^T)^{\frac{1}{2}} \boldsymbol{F}^T \boldsymbol{X}_2^T &= \boldsymbol{F}^{-T} \boldsymbol{F}^{-1} \\ \boldsymbol{X}_2 \boldsymbol{F} (\boldsymbol{R}_0 \boldsymbol{R}_0^T)^{\frac{1}{2}} &= \boldsymbol{F}^{-T} \\ \boldsymbol{F}^{-T} (\boldsymbol{R}_0 \boldsymbol{R}_0^T)^{-\frac{1}{2}} \boldsymbol{F}^{-1} &= \boldsymbol{X}_2 \end{aligned} \tag{3.53}$$

It is possible to split the quantity $\boldsymbol{R_0 R_0}^T$ into a product of its unique square roots because it is positive symmetric [62]. This allows the symmetry of the problem to be maintained in the solution. Utilizing the solution of $\boldsymbol{X}_2$ the solution to $\boldsymbol{X}_3$ can be found:

$$\boldsymbol{X}_2^T + \boldsymbol{X}_2 - \boldsymbol{X}_3 \boldsymbol{F} \boldsymbol{R}_0 \boldsymbol{R}_0^T \boldsymbol{F}^T \boldsymbol{X}_3 = \boldsymbol{0}$$

$$\boldsymbol{X}_3\boldsymbol{F}\boldsymbol{R}_0\boldsymbol{R}_0^T\boldsymbol{F}^T\boldsymbol{X}_3 = \boldsymbol{X}_2^T + \boldsymbol{X}_2$$

$$\boldsymbol{F}^{-T}\sqrt{\boldsymbol{2}}(\boldsymbol{R}_0\boldsymbol{R}_0^T)^{-\frac{1}{4}}(\boldsymbol{R}_0\boldsymbol{R}_0^T)^{-\frac{1}{4}}\sqrt{\boldsymbol{2}}\boldsymbol{F}^{-1} = \boldsymbol{X}_3\boldsymbol{F}(\boldsymbol{R}_0\boldsymbol{R}_0^T)^{\frac{1}{2}}(\boldsymbol{R}_0\boldsymbol{R}_0^T)^{\frac{1}{2}}\boldsymbol{F}^T\boldsymbol{X}_3$$

$$\boldsymbol{F}^{-T}\sqrt{\boldsymbol{2}}(\boldsymbol{R}_0\boldsymbol{R}_0^T)^{-\frac{1}{4}} = \boldsymbol{X}_3\boldsymbol{F}(\boldsymbol{R}_0\boldsymbol{R}_0^T)^{\frac{1}{2}}$$

$$\sqrt{\boldsymbol{2}}\boldsymbol{F}^{-T}(\boldsymbol{R}_0\boldsymbol{R}_0^T)^{-\frac{3}{4}}\boldsymbol{F}^{-1} = \boldsymbol{X}_3 \tag{3.54}$$

Using $\boldsymbol{X}_2$ and $\boldsymbol{X}_3$ to solve for $\boldsymbol{X}_1$ the result is:

$$\boldsymbol{X}_1 - \boldsymbol{X}_2\boldsymbol{F}\boldsymbol{R}_0\boldsymbol{R}_0^T\boldsymbol{F}^T\boldsymbol{X}_3 = \boldsymbol{0}$$

$$\boldsymbol{X}_2\boldsymbol{F}\boldsymbol{R}_0\boldsymbol{R}_0^T\boldsymbol{F}^T\boldsymbol{X}_3 = \boldsymbol{X}_1$$

$$\sqrt{\boldsymbol{2}}\boldsymbol{F}^{-T}(\boldsymbol{R}_0\boldsymbol{R}_0^T)^{-\frac{1}{4}}\boldsymbol{F}^{-1} = \boldsymbol{X}_1 \tag{3.55}$$

Compiling the elements of $\boldsymbol{X}$, the solution to the GCARE for the generalized rigid system is:

$$\boldsymbol{X} = \begin{bmatrix} \sqrt{\boldsymbol{2}}\boldsymbol{F}^{-T}(\boldsymbol{R}_0\boldsymbol{R}_0^T)^{-\frac{1}{4}}\boldsymbol{F}^{-1} & \boldsymbol{F}^{-T}(\boldsymbol{R}_0\boldsymbol{R}_0^T)^{-\frac{1}{2}}\boldsymbol{F}^{-1} \\ \boldsymbol{F}^{-T}(\boldsymbol{R}_0\boldsymbol{R}_0^T)^{-\frac{1}{2}}\boldsymbol{F}^{-1} & \sqrt{\boldsymbol{2}}\boldsymbol{F}^{-T}(\boldsymbol{R}_0\boldsymbol{R}_0^T)^{-\frac{3}{4}}\boldsymbol{F}^{-1} \end{bmatrix} \tag{3.56}$$

The system of equations for the GFARE can be generated by substituting (Equation 3.41)-(Equation 3.45), into (Equation 3.47) and can be enumerated as:

$$\boldsymbol{Z}_2 + \boldsymbol{Z}_2^T - \boldsymbol{Z}_1\boldsymbol{F}^{-T}\boldsymbol{F}^{-1}\boldsymbol{Z}_1 = \boldsymbol{0} \tag{3.57}$$

$$\boldsymbol{Z_3} - \boldsymbol{Z}_1\boldsymbol{F}^{-T}\boldsymbol{F}^{-1}\boldsymbol{Z}_2 = \boldsymbol{0} \tag{3.58}$$

$$\boldsymbol{Z_3} - \boldsymbol{Z}_2^T\boldsymbol{F}^{-T}\boldsymbol{F}^{-1}\boldsymbol{Z}_1 = \boldsymbol{0} \tag{3.59}$$

$$\boldsymbol{Z}_2^T\boldsymbol{F}^{-T}\boldsymbol{F}^{-1}\boldsymbol{Z}_2 = \boldsymbol{F}\boldsymbol{R}_0\boldsymbol{R}_0^T\boldsymbol{F}^T \tag{3.60}$$

Following similar procedure to the above GCARE formulation, the solution process begins

with solving for $\boldsymbol{Z}_2$:

$$\begin{aligned}
\boldsymbol{Z}_2^T \boldsymbol{F}^{-T} \boldsymbol{F}^{-1} \boldsymbol{Z}_2 &= \boldsymbol{F} \boldsymbol{R}_0 \boldsymbol{R}_0^T \boldsymbol{F}^T \\
\boldsymbol{Z}_2^T \boldsymbol{F}^{-T} \boldsymbol{F}^{-1} \boldsymbol{Z}_2 &= \boldsymbol{F} (\boldsymbol{R}_0 \boldsymbol{R}_0^T)^{\frac{1}{2}} (\boldsymbol{R}_0 \boldsymbol{R}_0^T)^{\frac{1}{2}} \boldsymbol{F}^T \\
\boldsymbol{F}^{-1} \boldsymbol{Z}_2 &= (\boldsymbol{R}_0 \boldsymbol{R}_0^T)^{\frac{1}{2}} \boldsymbol{F}^T \\
\boldsymbol{Z}_2 &= \boldsymbol{F} (\boldsymbol{R}_0 \boldsymbol{R}_0^T)^{\frac{1}{2}} \boldsymbol{F}^T
\end{aligned} \tag{3.61}$$

Using $\boldsymbol{Z}_2$, the solution for $\boldsymbol{Z}_1$ can be found:

$$\begin{aligned}
\boldsymbol{Z}_2 + \boldsymbol{Z}_2^T - \boldsymbol{Z}_1 \boldsymbol{F}^{-T} \boldsymbol{F}^{-1} \boldsymbol{Z}_1 &= \boldsymbol{0} \\
2\boldsymbol{F} (\boldsymbol{R}_0 \boldsymbol{R}_0^T)^{\frac{1}{2}} \boldsymbol{F}^T &= \boldsymbol{Z}_1 \boldsymbol{F}^{-T} \boldsymbol{F}^{-1} \boldsymbol{Z}_1 \\
\boldsymbol{F} \sqrt{2} (\boldsymbol{R}_0 \boldsymbol{R}_0^T)^{\frac{1}{4}} (\boldsymbol{R}_0 \boldsymbol{R}_0^T)^{\frac{1}{4}} \sqrt{2} \boldsymbol{F}^T &= \boldsymbol{Z}_1 \boldsymbol{F}^{-T} \boldsymbol{F}^{-1} \boldsymbol{Z}_1 \\
\boldsymbol{F} \sqrt{2} (\boldsymbol{R}_0 \boldsymbol{R}_0^T)^{\frac{1}{4}} &= \boldsymbol{Z}_1 \boldsymbol{F}^{-T} \\
\boldsymbol{F} \sqrt{2} (\boldsymbol{R}_0 \boldsymbol{R}_0^T)^{\frac{1}{4}} \boldsymbol{F}^T &= \boldsymbol{Z}_1
\end{aligned} \tag{3.62}$$

And the solution for $\boldsymbol{Z}_3$:

$$\begin{aligned}
\boldsymbol{Z}_3 - \boldsymbol{Z}_1 \boldsymbol{F}^{-T} \boldsymbol{F}^{-1} \boldsymbol{Z}_2 &= \boldsymbol{0} \\
\boldsymbol{Z}_1 \boldsymbol{F}^{-T} \boldsymbol{F}^{-1} \boldsymbol{Z}_2 &= \boldsymbol{Z}_3 \\
\boldsymbol{F} \sqrt{2} (\boldsymbol{R}_0 \boldsymbol{R}_0^T)^{\frac{3}{4}} \boldsymbol{F}^T &= \boldsymbol{Z}_3
\end{aligned} \tag{3.63}$$

With the total solution for $\boldsymbol{Z}$

$$\boldsymbol{Z} = \begin{bmatrix} \sqrt{2} \boldsymbol{F} (\boldsymbol{R}_0 \boldsymbol{R}_0^T)^{\frac{1}{4}} \boldsymbol{F}^T & \boldsymbol{F} (\boldsymbol{R}_0 \boldsymbol{R}_0^T)^{\frac{1}{2}} \boldsymbol{F}^T \\ \boldsymbol{F} (\boldsymbol{R}_0 \boldsymbol{R}_0^T)^{\frac{1}{2}} \boldsymbol{F}^T & \sqrt{2} \boldsymbol{F} (\boldsymbol{R}_0 \boldsymbol{R}_0^T)^{\frac{3}{4}} \boldsymbol{F}^T \end{bmatrix} \tag{3.64}$$

Using these ARE solutions, it is possible to use (Equation 3.38) to determine the the NCF

stability margin of the rigid-manipulator system. Executing this, we find that:

$$(\boldsymbol{ZX}) = \begin{bmatrix} 3\boldsymbol{I}_n & 2\sqrt{2}\boldsymbol{F}(\boldsymbol{R_0}\boldsymbol{R_0}^T)^{-\frac{1}{4}}\boldsymbol{F}^{-1} \\ 2\sqrt{2}\boldsymbol{F}(\boldsymbol{R_0}\boldsymbol{R_0}^T)^{\frac{1}{4}}\boldsymbol{F}^{-1} & 3\boldsymbol{I}_n \end{bmatrix} \tag{3.65}$$

While this product is still a function of the rigid mode of the manipulator system, upon finding the characteristic equation:

$$p_{(\boldsymbol{ZX})}(\lambda) = \left(\lambda^2 - 6\lambda + 1\right)^n \tag{3.66}$$

The roots of the characteristic equation are $\{3 \pm 2\sqrt{2}\}$ with multiplicity n. Finishing the evaluation of (Equation 3.38), it is found that the NCF stability margin, for rigid manipulator systems, can *only* have the value of $\frac{1}{\sqrt{4+2\sqrt{2}}}$, or 0.38268343 (truncated for conciseness). ■

Remark. *The value of the NCF stability margin for the rigid manipulator with no flexible modes is not dependent on any system parameter, illustrated in the characteristic equation* (Equation 3.66)*, meaning all postures of a rigid manipulator will have this stability margin. Later in this work we will discuss the effect of additional flexible modes on this value.*

Remark. *The solution of the NCF stability margin for a rigid manipulator system, firstly, has no dependence on the inertia matrix or the rigid mode itself. This implies that neither the definiteness nor the structure of the inertia matrix impact the solution.*

Remark. *The above construction holds for redundant manipulators, however, allowances must be made for the redundancy in the $\boldsymbol{T}$ matrix in* (Equation 3.14)*. Further, any double-integrator system in the form of* (Equation 3.41) *will result in the same maximal value.*

The solution above can be confirmed numerically through existing Riccati equation solution methods. Mentioned in Kucera's early work [63], it is possible to find a non-negative, stabilizing solution to an ARE given that the system is controllable and observable. Intro-

ducing a Hamiltonian matrix,

$$\boldsymbol{\Psi} = \begin{bmatrix} \boldsymbol{A} & -\boldsymbol{B}\boldsymbol{B}^T \\ -\boldsymbol{C}^T\boldsymbol{C} & -\boldsymbol{A}^T \end{bmatrix} \tag{3.67}$$

under the assumption that $\boldsymbol{\Psi} \in \mathbb{C}^{2l\times 2l}$ is diagonalizable. This matrix, being real with the above structure has eigenvalues occurring in quadruples. This is to say that for an eigenvalue of $\boldsymbol{A}$, $\lambda \in \mathbb{C}$, the spectrum will also contain $\lambda^*, -\lambda$, and $-\lambda^*$. Given the right-eigenvectors of $\boldsymbol{\Psi}$, $\boldsymbol{u}_i = \begin{bmatrix} \boldsymbol{x}_i^T & \boldsymbol{y}_i^T \end{bmatrix}^T$, the matrix $\boldsymbol{\Lambda} = \boldsymbol{Y}\boldsymbol{X}^{-1} = \boldsymbol{\Lambda}^*$ is a solution to the ARE. The matrices $\boldsymbol{Y} = [\boldsymbol{y}_1, ..., \boldsymbol{y}_l]$ and $\boldsymbol{X} = [\boldsymbol{x}_1, ..., \boldsymbol{x}_l]$ are selected such that the matrix $\boldsymbol{X}$ is invertible.

It should be noted that since the Riccati problem is quadratic, there is a uniqueness issue for $\boldsymbol{\Lambda}$. This can also be seen in the spectral quadruple of $\boldsymbol{\Psi}$. Therefore selections of eigenvalues (and their associated vectors) will give negative solutions as well.

This eigenspace decomposition provides a framework for other, equivalent forms of decomposition: namely Schur decomposition [64] and utilization of the matrix sign function [65, 66]. In essence, these methods function the same way as the eigendecomposition above, but have numerical advantages for certain systems. The matrix sign method is used to validate the analytical solution in section B.1.

3.4.3 Evaluation of the NCF Stability Margin for SISO Systems

It has been shown that the preceding work holds for all classes of system, and that the primary interest of this work is to investigate the stability of MIMO flexible systems. SISO systems, on the other hand, can be considered to be a special case of the MIMO formulation. Consider the modally decomposed SISO system:

$$P(s) = \frac{\kappa_0}{s^2} + \sum_{i=1}^{m} \frac{\kappa_i}{s^2 + 2\zeta_i\omega_{ni}s + \omega_{ni}^2} \tag{3.68}$$

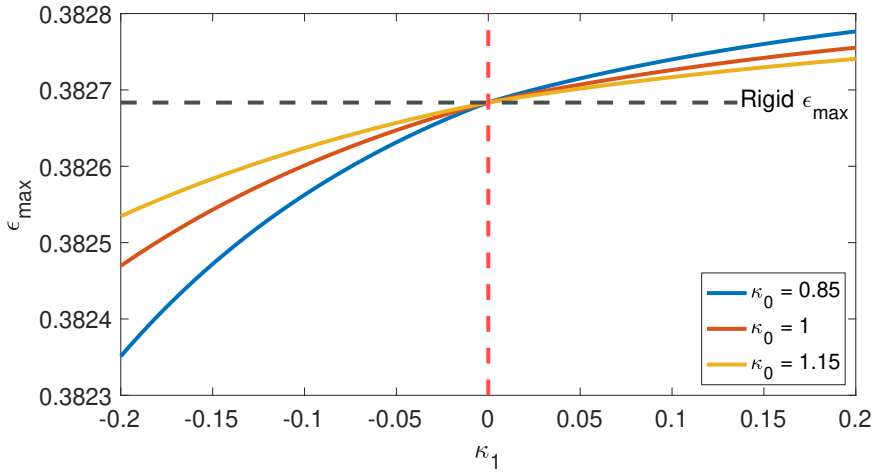

Figure 3.3: NCF stability for an SISO system over various combinations of κ_0 and κ_1. The black dotted line is the theoretical constant for rigid systems proven in subsection 3.4.2, and the red dotted line is the case of a rigid body.

where $\kappa_j \in \mathbb{R}\ \forall j = 0, \ldots, m$, ζ_i is the damping coefficient of the i^{th} mode, and ω_{ni} is the natural frequency of the i^{th} mode. κ_0 is analogous to the rigid mode in the MIMO formulation and the other m κ_i are the flexible residues. Evaluation of the NCF stability margin for various rigid modes over a range of κ_1 yields the curves shown in Figure 3.3.

It can be seen in this figure that the rigid case, where $\kappa_1 = 0$, yields the theoretical maximum NCF stability margin previously shown in this work. As flexibility is introduced into the system however, one of two things can happen. Obviously κ_1 deviates from 0, however if the system has co-located sensors and actuators, this residual is positive. Non-colocated sensors yield a negative residual value. In the case of co-location, it is possible to exceed the theoretical maximum NCF margin for rigid systems due to the resulting in-phase motion between the actuator and the sensor. Negative κ_1 indicates a non-colocated sensor and that the motion between the sensor and actuator are *not* in phase. This lowers the NCF stability margin and will generate instability for large controller gain. The effect of an in-phase flexible mode on an SISO rigid system is demonstrated in section B.2.

The solution of the NCF stability margin for an SISO rigid system can be immediately

extended from equations (Equation 3.64), (Equation 3.56), and (Equation 3.65):

$$\boldsymbol{Z}_{rigid} = f^2 \begin{bmatrix} \sqrt{2\kappa_0} & \kappa_0 \\ \kappa_0 & \sqrt{2\kappa_0^3} \end{bmatrix} \tag{3.69}$$

$$\boldsymbol{X}_{rigid} = \frac{1}{f^2} \begin{bmatrix} \sqrt{\frac{2}{\kappa_0}} & \frac{1}{\kappa_0} \\ \frac{1}{\kappa_0} & \sqrt{\frac{2}{\kappa_0^3}} \end{bmatrix} \tag{3.70}$$

$$\boldsymbol{ZX}_{rigid} = \begin{bmatrix} 3 & 2\sqrt{\frac{2}{\kappa_0}} \\ 2\sqrt{2\kappa_0} & 3 \end{bmatrix} \tag{3.71}$$

where f is the scalar distribution factor analogous to $\boldsymbol{F}$ in (Equation 3.45). With characteristic equation:

$$p(\lambda)_{(\boldsymbol{ZX_{rigid}})} = \lambda^2 - 6\lambda + 1 \tag{3.72}$$

Therefore, the SISO, rigid ε_{max} value is equal to $\frac{1}{\sqrt{4+2\sqrt{2}}}$, the constant for rigid systems.

While the inclusion of a flexible mode decreases the solvability of the algebraic Riccati equations (Equation 3.46) and (Equation 3.47), it is still possible to explore its effect upon the solutions $\boldsymbol{Z}$ and $\boldsymbol{X}$, as well as the NCF stability margin. Consider the modal-based state space construction of the SISO manipulator system extended to encapsulate a flexible mode:

$$\boldsymbol{A}_{SISO} = \begin{bmatrix} \boldsymbol{S}_0 & \boldsymbol{0}_2 \\ \boldsymbol{0}_2 & \boldsymbol{S}_1 \end{bmatrix} \in \mathbb{R}^{4\times4},\ \boldsymbol{S}_0 = \begin{bmatrix} 0 & 1 \\ 0 & 0 \end{bmatrix},\ \boldsymbol{S}_1 = \begin{bmatrix} 0 & 1 \\ -\omega^2 & -2\zeta\omega \end{bmatrix} \tag{3.73}$$

$$\boldsymbol{B}_{SISO} = \begin{bmatrix} 0 \\ \sqrt{\kappa_0} \\ 0 \\ \sqrt{\kappa_1} \end{bmatrix} \in \mathbb{R}^4 \tag{3.74}$$

$$\boldsymbol{C}_{SISO} = \begin{bmatrix} \sqrt{\kappa_0} & 0 & \sqrt{\kappa_1} & 0 \end{bmatrix} \in \mathbb{R}^{1\times4} \tag{3.75}$$

$$\boldsymbol{D}_{SISO} = \mathbf{0} \tag{3.76}$$

It is possible to linearize this system about $\kappa_1 = 0$ and treat the increasing flexible mode as a perturbation. Taking $0 < \gamma << 1$ to be the displacement of the flexible mode, the perturbed state-space can be formulated as:

$$\boldsymbol{B}_{SISO} = \boldsymbol{B}_0 + \boldsymbol{\Delta B} = \begin{bmatrix} 0 \\ \sqrt{\kappa_0} \\ 0 \\ 0 \end{bmatrix} + \begin{bmatrix} 0 \\ 0 \\ 0 \\ \sqrt{\gamma} \end{bmatrix} \tag{3.77}$$

$$\boldsymbol{C}_{SISO} = \boldsymbol{C}_0 + \boldsymbol{\Delta C} = \begin{bmatrix} \sqrt{\kappa_0} & 0 & 0 & 0 \end{bmatrix} + \begin{bmatrix} 0 & 0 & \sqrt{\gamma} & 0 \end{bmatrix} \tag{3.78}$$

It should also be noted that the flexible residual may be negative ($0 > \gamma >> -1$), in which case either the entry corresponding to the flexible residual in either $\boldsymbol{B}_{SISO}$ or $\boldsymbol{C}_{SISO}$ should be negative.

Intuitively, the corresponding solutions to the GCARE (Equation 3.46) and GFARE (Equation 3.47) can be considered to be the sum of solution to the rigid equations (SISO form of solution provided in (Equation 3.71) for $f = \sqrt{\frac{1}{\kappa_0}}$) and a perturbation in the solution:

$$\begin{aligned} \boldsymbol{X}_{SISO} &= \boldsymbol{X}_0 + \boldsymbol{\Delta X} \\ &= \begin{bmatrix} \boldsymbol{X}_r & \mathbf{0}_2 \\ \mathbf{0}_2 & \mathbf{0}_2 \end{bmatrix} + \begin{bmatrix} \boldsymbol{\Delta X}_1 & \boldsymbol{\Delta X}_2 \\ \boldsymbol{\Delta X}_2^T & \boldsymbol{\Delta X}_4 \end{bmatrix} \\ \boldsymbol{X}_r &= \begin{bmatrix} \sqrt{2\kappa_0} & 1 \\ 1 & \sqrt{\frac{2}{\kappa_0}} \end{bmatrix} \end{aligned} \tag{3.79}$$

$$
\begin{aligned}
\boldsymbol{Z}_{SISO} &= \boldsymbol{Z}_0 + \boldsymbol{\Delta Z} \\
&= \begin{bmatrix} \boldsymbol{Z}_r & \boldsymbol{0}_2 \\ \boldsymbol{0}_2 & \boldsymbol{0}_2 \end{bmatrix} + \begin{bmatrix} \boldsymbol{\Delta Z}_1 & \boldsymbol{\Delta Z}_2 \\ \boldsymbol{\Delta Z}_2^T & \boldsymbol{\Delta Z}_4 \end{bmatrix} \\
\boldsymbol{Z}_r &= \begin{bmatrix} \sqrt{\frac{2}{\kappa_0}} & 1 \\ 1 & \sqrt{2\kappa_0} \end{bmatrix}
\end{aligned} \tag{3.80}
$$

This construction is supported by existing work in perturbations of algebraic Riccati equations [67, 68, 69] Substituting all of the perturbed matrices into the GCARE and GFARE yields:

$$
\begin{aligned}
&\boldsymbol{A}_{SISO}^*(\boldsymbol{X}_0 + \boldsymbol{\Delta X}) + (\boldsymbol{X}_0 + \boldsymbol{\Delta X})\boldsymbol{A}_{SISO} \\
&\quad - (\boldsymbol{X}_0 + \boldsymbol{\Delta X})(\boldsymbol{B}_0 + \boldsymbol{\Delta B})(\boldsymbol{B}_0 + \boldsymbol{\Delta B})^*(\boldsymbol{X}_0 + \boldsymbol{\Delta X}) \\
&\quad + (\boldsymbol{C}_0 + \boldsymbol{\Delta C})^*(\boldsymbol{C}_0 + \boldsymbol{\Delta C}) = \boldsymbol{0}
\end{aligned} \tag{3.81}
$$

$$
\begin{aligned}
&\boldsymbol{A}_{SISO}(\boldsymbol{Z}_0 + \boldsymbol{\Delta Z}) + (\boldsymbol{Z}_0 + \boldsymbol{\Delta Z})\boldsymbol{A}_{SISO}^* \\
&\quad - (\boldsymbol{Z}_0 + \boldsymbol{\Delta Z})(\boldsymbol{C}_0 + \boldsymbol{\Delta C})^*(\boldsymbol{C}_0 + \boldsymbol{\Delta C})(\boldsymbol{Z}_0 + \boldsymbol{\Delta Z}) \\
&\quad + (\boldsymbol{B}_0 + \boldsymbol{\Delta B})(\boldsymbol{B}_0 + \boldsymbol{\Delta B})^* = \boldsymbol{0}
\end{aligned} \tag{3.82}
$$

Eliminating the second-order perturbations and the nominal products, the perturbed GCARE and GFARE become:

$$
\begin{aligned}
&\boldsymbol{A}_{SISO}^*\boldsymbol{\Delta X} + \boldsymbol{\Delta X}\boldsymbol{A}_{SISO} + \boldsymbol{\Delta C}^*\boldsymbol{\Delta C} + \boldsymbol{\Delta C}^*\boldsymbol{C}_0 + \\
&\quad \boldsymbol{C}_0^*\boldsymbol{\Delta C} - \boldsymbol{X}_0\boldsymbol{B}_0\boldsymbol{B}_0^*\boldsymbol{\Delta X} - \boldsymbol{\Delta X}\boldsymbol{B}_0\boldsymbol{B}_0^*\boldsymbol{X}_0 \\
&\quad - \boldsymbol{X}_0\boldsymbol{\Delta B}\boldsymbol{\Delta B}^*\boldsymbol{X}_0 = \boldsymbol{0}
\end{aligned} \tag{3.83}
$$

$$
\begin{aligned}
&\boldsymbol{A}_{SISO}\boldsymbol{\Delta Z} + \boldsymbol{\Delta Z}\boldsymbol{A}_{SISO}^* + \boldsymbol{\Delta B}\boldsymbol{\Delta B}^* + \boldsymbol{B}_0\boldsymbol{\Delta B}^* \\
&\quad + \boldsymbol{\Delta B}\boldsymbol{B}_0^* - \boldsymbol{Z}_0\boldsymbol{C}_0^*\boldsymbol{C}_0\boldsymbol{\Delta Z} - \boldsymbol{\Delta Z}\boldsymbol{C}_0^*\boldsymbol{C}_0\boldsymbol{Z}_0 \\
&\quad - \boldsymbol{Z}_0\boldsymbol{\Delta C}^*\boldsymbol{\Delta C}\boldsymbol{Z}_0 = \boldsymbol{0}
\end{aligned} \tag{3.84}
$$

When expanded, these equations can be solved for $\boldsymbol{\Delta X}$ and $\boldsymbol{\Delta Z}$:

$$\boldsymbol{\Delta X}_1 = \mathbf{0}_2 \tag{3.85}$$

$$\boldsymbol{\Delta X}_2 = \begin{bmatrix} \frac{\sqrt{\gamma}\sqrt{\kappa_0}\left(\sqrt{2}+4\,\omega\,\zeta\sqrt{\frac{1}{\kappa_0}}+2\,\omega^3\,\zeta\left(\frac{1}{\kappa_0}\right)^{3/2}+\frac{4\sqrt{2}\,\omega^2\,\zeta^2}{\kappa_0}\right)}{\left(\frac{1}{\kappa_0}\right)^{3/2}\left(\kappa_0^2+\omega^4+4\,\kappa_0\,\omega^2\,\zeta^2+\frac{2\sqrt{2}\,\omega^3\,\zeta}{\sqrt{\frac{1}{\kappa_0}}}+\frac{2\sqrt{2}\,\omega\,\zeta}{\left(\frac{1}{\kappa_0}\right)^{3/2}}\right)} \\ \frac{\sqrt{\gamma}\,\kappa_0^{3/2}\left(\frac{4\,\omega^2\,\zeta^2}{\kappa_0}-\frac{\omega^2}{\kappa_0}+2\sqrt{2}\,\omega\,\zeta\sqrt{\frac{1}{\kappa_0}}+1\right)}{\kappa_0^2+\omega^4+4\,\kappa_0\,\omega^2\,\zeta^2+\frac{2\sqrt{2}\,\omega^3\,\zeta}{\sqrt{\frac{1}{\kappa_0}}}+\frac{2\sqrt{2}\,\omega\,\zeta}{\left(\frac{1}{\kappa_0}\right)^{3/2}}} \end{bmatrix} \tag{3.86}$$

$$\begin{bmatrix} \frac{\sqrt{\gamma}\sqrt{\kappa_0}\left(\kappa_0+\omega^2+2\sqrt{2}\,\kappa_0\,\omega\,\zeta\sqrt{\frac{1}{\kappa_0}}\right)}{\kappa_0^2+\omega^4+4\,\kappa_0\,\omega^2\,\zeta^2+2\sqrt{2}\,\kappa_0^2\,\omega\,\zeta\sqrt{\frac{1}{\kappa_0}}+2\sqrt{2}\,\kappa_0\,\omega^3\,\zeta\sqrt{\frac{1}{\kappa_0}}} \\ \frac{\sqrt{\gamma}\sqrt{\kappa_0}\left(2\,\omega\,\zeta+\sqrt{2}\,\kappa_0\sqrt{\frac{1}{\kappa_0}}\right)}{\kappa_0^2+\omega^4+4\,\kappa_0\,\omega^2\,\zeta^2+2\sqrt{2}\,\kappa_0^2\,\omega\,\zeta\sqrt{\frac{1}{\kappa_0}}+2\sqrt{2}\,\kappa_0\,\omega^3\,\zeta\sqrt{\frac{1}{\kappa_0}}} \end{bmatrix}$$

$$\boldsymbol{\Delta X}_4 = \begin{bmatrix} \frac{\gamma\left(4\,\zeta^2+1\right)}{4\,\omega\,\zeta} & \frac{\gamma}{2\,\omega^2} \\ \frac{\gamma}{2\,\omega^2} & \frac{\gamma}{4\,\omega^3\,\zeta} \end{bmatrix} \tag{3.87}$$

$$\boldsymbol{\Delta Z}_1 = \mathbf{0}_2 \tag{3.88}$$

$$\boldsymbol{\Delta Z}_2 = \begin{bmatrix} \frac{\sqrt{\gamma}\sqrt{\kappa_0}\left(2\,\omega\,\zeta+\sqrt{2}\,\kappa_0\sqrt{\frac{1}{\kappa_0}}\right)}{\kappa_0^2+\omega^4+4\,\kappa_0\,\omega^2\,\zeta^2+2\sqrt{2}\,\kappa_0^2\,\omega\,\zeta\sqrt{\frac{1}{\kappa_0}}+2\sqrt{2}\,\kappa_0\,\omega^3\,\zeta\sqrt{\frac{1}{\kappa_0}}} \\ \frac{\sqrt{\gamma}\,\kappa_0^{3/2}\left(\frac{\omega^2}{\kappa_0}+2\sqrt{2}\,\omega\,\zeta\sqrt{\frac{1}{\kappa_0}}+1\right)}{\kappa_0^2+\omega^4+4\,\kappa_0\,\omega^2\,\zeta^2+\frac{2\sqrt{2}\,\omega^3\,\zeta}{\sqrt{\frac{1}{\kappa_0}}}+\frac{2\sqrt{2}\,\omega\,\zeta}{\left(\frac{1}{\kappa_0}\right)^{3/2}}} \end{bmatrix} \tag{3.89}$$

$$\begin{bmatrix} \frac{\sqrt{\gamma}\sqrt{\kappa_0}\left(\kappa_0-\omega^2\right)}{\kappa_0^2+\omega^4+4\,\kappa_0\,\omega^2\,\zeta^2+2\sqrt{2}\,\kappa_0^2\,\omega\,\zeta\sqrt{\frac{1}{\kappa_0}}+2\sqrt{2}\,\kappa_0\,\omega^3\,\zeta\sqrt{\frac{1}{\kappa_0}}} \\ \frac{\sqrt{\gamma}\,\kappa_0^{3/2}\left(2\,\omega\,\zeta+\sqrt{2}\,\kappa_0\sqrt{\frac{1}{\kappa_0}}\right)}{\kappa_0^2+\omega^4+4\,\kappa_0\,\omega^2\,\zeta^2+2\sqrt{2}\,\kappa_0^2\,\omega\,\zeta\sqrt{\frac{1}{\kappa_0}}+2\sqrt{2}\,\kappa_0\,\omega^3\,\zeta\sqrt{\frac{1}{\kappa_0}}} \end{bmatrix}$$

$$\boldsymbol{\Delta Z}_4 = \begin{bmatrix} \frac{\gamma}{4\,\omega^3\,\zeta} & 0 \\ 0 & \frac{\gamma}{4\,\omega\,\zeta} \end{bmatrix} \tag{3.90}$$

These solutions, found through the symbolic math toolbox (Matlab, Mathworks) can be used to evaluate the matrix product $\boldsymbol{Z}_{SISO}\boldsymbol{X}_{SISO}$ and can then extend to calculating the

NCF stability margin. Expanding the matrix product $\boldsymbol{Z}_{SISO}\boldsymbol{X}_{SISO}$:

$$\begin{aligned}
\boldsymbol{Z}_{SISO}\boldsymbol{X}_{SISO} &= (\boldsymbol{Z}_0 + \boldsymbol{\Delta Z})(\boldsymbol{X}_0 + \boldsymbol{\Delta X}) \\
&= \boldsymbol{Z}_0\boldsymbol{X}_0 + \boldsymbol{Z}_0\boldsymbol{\Delta X} + \boldsymbol{\Delta Z}\boldsymbol{X}_0 + \boldsymbol{\Delta Z}\boldsymbol{\Delta X} \\
&= \begin{bmatrix} \boldsymbol{Z}_r\boldsymbol{X}_r & \boldsymbol{0}_2 \\ \boldsymbol{0}_2 & \boldsymbol{0}_2 \end{bmatrix} + \begin{bmatrix} \boldsymbol{0}_2 & \boldsymbol{Z}_r\boldsymbol{\Delta X}_2 \\ \boldsymbol{0}_2 & \boldsymbol{0}_2 \end{bmatrix} \\
&\quad + \begin{bmatrix} \boldsymbol{0}_2 & \boldsymbol{0}_2 \\ \boldsymbol{\Delta Z}_2^T\boldsymbol{X}_r & \boldsymbol{0}_2 \end{bmatrix} \\
&\quad + \begin{bmatrix} \boldsymbol{\Delta Z}_2\boldsymbol{\Delta X}_2^T & \boldsymbol{\Delta Z}_2\boldsymbol{\Delta X}_4 \\ \boldsymbol{\Delta Z}_4\boldsymbol{\Delta X}_2^T & \boldsymbol{\Delta Z}_2^T\boldsymbol{\Delta X}_2 + \boldsymbol{\Delta Z}_4\boldsymbol{\Delta X}_4 \end{bmatrix}
\end{aligned} \tag{3.91}$$

In terms of powers of γ, this product can be likened to:

$$\boldsymbol{Z}_{SISO}\boldsymbol{X}_{SISO} \propto \left(\begin{bmatrix} 1 & 0 \\ 0 & 0 \end{bmatrix} + \begin{bmatrix} 0 & 0 \\ \gamma^{\frac{1}{2}} & 0 \end{bmatrix} + \begin{bmatrix} 0 & \gamma^{\frac{1}{2}} \\ 0 & 0 \end{bmatrix} + \begin{bmatrix} \gamma & \gamma^{\frac{3}{2}} \\ \gamma^{\frac{3}{2}} & \gamma + \gamma^2 \end{bmatrix} \right) \bigotimes \boldsymbol{I}_2 \tag{3.92}$$

Furthermore, γ is assumed to be much smaller than 1, powers of gamma that are *greater* than 1 can be neglected such that:

$$\begin{aligned}
\boldsymbol{Z}_{SISO}\boldsymbol{X}_{SISO} &\propto \left(\begin{bmatrix} 1 & 0 \\ 0 & 0 \end{bmatrix} + \begin{bmatrix} 0 & 0 \\ \gamma^{\frac{1}{2}} & 0 \end{bmatrix} + \begin{bmatrix} 0 & \gamma^{\frac{1}{2}} \\ 0 & 0 \end{bmatrix} + \begin{bmatrix} \gamma & 0 \\ 0 & \gamma \end{bmatrix} \right) \bigotimes \boldsymbol{I}_2 \\
&\propto \left(\begin{bmatrix} 1+\gamma & \gamma^{\frac{1}{2}} \\ \gamma^{\frac{1}{2}} & \gamma \end{bmatrix} \right) \bigotimes \boldsymbol{I}_2
\end{aligned} \tag{3.93}$$

$$\begin{aligned}
\boldsymbol{Z}_{SISO}\boldsymbol{X}_{SISO} &\approx \begin{bmatrix} \boldsymbol{Z}_r\boldsymbol{X}_r + \boldsymbol{\Delta Z}_2\boldsymbol{\Delta X}_2^T & \boldsymbol{Z}_r\boldsymbol{\Delta X}_2 \\ \boldsymbol{\Delta Z}_2^T\boldsymbol{X}_r & \boldsymbol{\Delta Z}_2^T\boldsymbol{\Delta X}_2 \end{bmatrix} = \tilde{\boldsymbol{Z}\boldsymbol{X}}, \\
\boldsymbol{Z}_r\boldsymbol{X}_r &= \begin{bmatrix} 3 & 2\sqrt{\frac{2}{\kappa_0}} \\ 2\sqrt{2\kappa_0} & 3 \end{bmatrix} = (\boldsymbol{X}_r\boldsymbol{Z}_r)^T
\end{aligned} \tag{3.94}$$

Attempting to find the characteristic equation of the matrix $\boldsymbol{Z}\tilde{\boldsymbol{X}}$ yields (all Δ symbols are removed for conciseness):

$$\begin{aligned} \mathrm{p}_{\boldsymbol{Z}\tilde{\boldsymbol{X}}}(\lambda) &= |\boldsymbol{Z}\tilde{\boldsymbol{X}} - \lambda \boldsymbol{I}_4| \\ &= |\boldsymbol{Z}_r \boldsymbol{X}_r \boldsymbol{Z}_2^T \boldsymbol{X}_2 + \boldsymbol{Z}_2 \boldsymbol{X}_2 \boldsymbol{Z}_2^T \boldsymbol{X}_2 - \boldsymbol{Z}_2^T \boldsymbol{X}_r \boldsymbol{Z}_r \boldsymbol{X}_2 \\ &\quad - \lambda \left(\boldsymbol{Z}_2^T \boldsymbol{X}_2 + \boldsymbol{Z}_r \boldsymbol{X}_r + \boldsymbol{Z}_2 \boldsymbol{X}_2^T \right) + \lambda^2 \boldsymbol{I}_2| \end{aligned} \tag{3.95}$$

Removing second order terms, the characteristic equation can be reduced to:

$$\begin{aligned} \mathrm{p}_{\boldsymbol{Z}\tilde{\boldsymbol{X}}}(\lambda) \approx |&\boldsymbol{Z}_r \boldsymbol{X}_r \boldsymbol{Z}_2^T \boldsymbol{X}_2 - \boldsymbol{Z}_2^T \boldsymbol{X}_r \boldsymbol{Z}_r \boldsymbol{X}_2 \\ &- \lambda \left(\boldsymbol{Z}_2^T \boldsymbol{X}_2 + \boldsymbol{Z}_r \boldsymbol{X}_r + \boldsymbol{Z}_2 \boldsymbol{X}_2^T \right) + \lambda^2 \boldsymbol{I}_2| \end{aligned} \tag{3.96}$$

Regrouping, this becomes:

$$\begin{aligned} \mathrm{p}_{\boldsymbol{Z}\tilde{\boldsymbol{X}}}(\lambda) &\approx |\boldsymbol{S}_0 - \lambda \boldsymbol{S}_1 + \lambda^2 \boldsymbol{I}_2| \\ \boldsymbol{S}_1 &= \boldsymbol{Z}_2^T \boldsymbol{X}_2 + \boldsymbol{Z}_r \boldsymbol{X}_r + \boldsymbol{Z}_2 \boldsymbol{X}_2^T = \begin{bmatrix} S_{1a} & S_{1b} \\ S_{1c} & S_{1d} \end{bmatrix} \\ \boldsymbol{S}_0 &= \boldsymbol{Z}_r \boldsymbol{X}_r \boldsymbol{Z}_2^T \boldsymbol{X}_2 - \boldsymbol{Z}_2^T \boldsymbol{X}_r \boldsymbol{Z}_r \boldsymbol{X}_2 = \begin{bmatrix} S_{0a} & S_{0b} \\ S_{0c} & S_{0d} \end{bmatrix} \end{aligned} \tag{3.97}$$

and evaluates to:

$$\begin{aligned} \mathrm{p}_{\boldsymbol{Z}\tilde{\boldsymbol{X}}}(\lambda) \approx \lambda^4 &- (S_{1a} + S_{1d})\, \lambda^3 \\ &+ (S_{0a} + S_{0d} + S_{1a}\, S_{1d} - S_{1b}\, S_{1c})\, \lambda^2 \\ &+ (S_{0b}\, S_{1c} - S_{0a}\, S_{1d} + S_{0c}\, S_{1b} - S_{0d}\, S_{1a})\, \lambda \\ &+ S_{0a}\, S_{0d} - S_{0b}\, S_{0c} \end{aligned} \tag{3.98}$$

$$\begin{aligned} \mathrm{p}_{\boldsymbol{Z}\tilde{\boldsymbol{X}}}(\lambda) \approx \lambda^4 &- (6 - O(\gamma))\, \lambda^3 + (1 + O(\gamma))\, \lambda^2 \\ &+ O(\gamma)\lambda + O(\gamma) \end{aligned} \tag{3.99}$$

Table 3.1: SISO Example System Parameters

Parameter	Value	Parameter	Value
ω	$20\left[\frac{rad}{s}\right]$	ζ	1×10^{-5}
κ_0	10	γ	$variable$

$$\approx \lambda^2\left(\lambda^2 - 6\lambda + 1\right) + O(\gamma, \lambda) \tag{3.100}$$

Numerical Analysis of SISO Case

The above holds for a rigid system and yields a comparable characteristic equation as in (Equation 3.66) (albeit scalar with two extra roots at 0 and not matrix polynomial). The NCF stability margin of the SISO flexible system is based upon the largest root of the characteristic equation of $\boldsymbol{Z}_{SISO}\boldsymbol{X}_{SISO}$, as γ changes its effect on the maximum root are illustrated in Figure 3.4 for the system described by the parameters in Table 3.1.

Using those same parameters, the characteristic equation in (Equation 3.100) can be expressed as:

$$\begin{aligned} \mathrm{p}_{\tilde{\boldsymbol{Z}\boldsymbol{X}}} \approx\ & \lambda^4 + (2.49 \times 10^{-4}\gamma - 6.0)\lambda^3 \\ & + (1.55 \times 10^{-8}\gamma^2 + 1.57 \times 10^{-7}\gamma + 1.0)\lambda^2 \\ & + (9.33 \times 10^{-8}\gamma^2 - 0.00225\gamma)\lambda + 1.4 \times 10^{-7}\gamma^2 \end{aligned} \tag{3.101}$$

Continuing the assumption that γ is small, the above can be reduced to:

$$\begin{aligned} \mathrm{p}_{\tilde{\boldsymbol{Z}\boldsymbol{X}}} \approx & \lambda^2(\lambda^2 - 6\lambda + 1) \\ & + \gamma(2.49 \times 10^{-4}\lambda^3 \\ & + 1.57 \times 10^{-7}\lambda^2 - 0.00225\lambda) \end{aligned} \tag{3.102}$$

Theorem 4. *For an SISO flexible-base system, the maximum root of the characteristic equation of the product $\boldsymbol{Z}_{SISO}\boldsymbol{X}_{SISO}$ displaces away from the nominal root $\bar{\lambda}_{max} \triangleq 3 + 2\sqrt{2}$ in the direction opposite the change in γ (where γ is the perturbation in κ_1 and is*

assumed to be $|\gamma| << 1$). *That is to say:* $\gamma > 0$ *induces* $\Delta\lambda < 0$ *and* $\gamma < 0$ *induces* $\Delta\lambda > 0$.

Proof. Consider both the scalar version of the nominal characteristic equation in (Equation 3.66) and the approximate characteristic equation given in (Equation 3.102). For a displaced largest root, $\lambda = \bar{\lambda}_{max} + \Delta\lambda > 0$, $|\Delta\lambda| << 1$, to be a root of the approximate characteristic polynomial it must satisfy yields:

$$\begin{aligned} \mathrm{p}_{\tilde{\boldsymbol{Z}\boldsymbol{X}}} \big|_{\lambda=\bar{\lambda}_{max}+\Delta\lambda} \approx\ & (\bar{\lambda}_{max} + \Delta\lambda)^2 \cdot \\ & \big((\bar{\lambda}_{max} + \Delta\lambda)^2 - 6(\bar{\lambda}_{max} + \Delta\lambda) + 1\big) \\ & + \gamma \big(2.49 \times 10^{-4}(\bar{\lambda}_{max} + \Delta\lambda)^3 \\ & + 1.57 \times 10^{-7}(\bar{\lambda}_{max} + \Delta\lambda)^2 \\ & -0.00225(\bar{\lambda}_{max} + \Delta\lambda\big) = 0 \end{aligned} \tag{3.103}$$

Separating the above into the the rigid characteristic polynomial and the perturbation from γ, the above equality becomes:

$$\begin{aligned} & (\bar{\lambda}_{max} + \Delta\lambda)^2 \big((\bar{\lambda}_{max} + \Delta\lambda)^2 - 6(\bar{\lambda}_{max} + \Delta\lambda) + 1\big) \\ & = (\bar{\lambda}_{max} + \Delta\lambda)^2 \big(\bar{\lambda}_{max}^2 + 2\bar{\lambda}_{max}\Delta\lambda + \Delta\lambda^2 \\ & \quad -6\bar{\lambda}_{max} - 6\Delta\lambda + 1\big) \\ & = (\bar{\lambda}_{max} + \Delta\lambda)^2 \big(2\bar{\lambda}_{max}\Delta\lambda - 6\Delta\lambda + \Delta\lambda^2\big) \\ & = -\gamma \big(2.49 \times 10^{-4}(\bar{\lambda}_{max} + \Delta\lambda)^3 \\ & \quad + 1.57 \times 10^{-7}(\bar{\lambda}_{max} + \Delta\lambda)^2 \\ & \quad -0.00225(\bar{\lambda}_{max} + \Delta\lambda\big) \end{aligned} \tag{3.104}$$

The above equality can be further simplified. First, simplifying the left-hand side:

$$\begin{aligned}(\bar{\lambda}_{max} + \Delta\lambda)^2 \left(2\bar{\lambda}_{max}\Delta\lambda - 6\Delta\lambda + \Delta\lambda^2\right) \approx \\ (\bar{\lambda}_{max} + \Delta\lambda)^2 \left(4\sqrt{2}\Delta\lambda\right)\end{aligned} \tag{3.105}$$

And the right:

$$(\bar{\lambda}_{max} + \Delta\lambda)^3 \approx \bar{\lambda}_{max}^3 \tag{3.106}$$

$$(\bar{\lambda}_{max} + \Delta\lambda)^2 \approx \bar{\lambda}_{max}^2 \tag{3.107}$$

$$(\bar{\lambda}_{max} + \Delta\lambda) \approx \bar{\lambda}_{max} \tag{3.108}$$

$$\begin{aligned}-\gamma \big(2.49 \times 10^{-4}(\bar{\lambda}_{max} + \Delta\lambda)^3 \\ + 1.57 \times 10^{-7}(\bar{\lambda}_{max} + \Delta\lambda)^2 \\ -0.00225(\bar{\lambda}_{max} + \Delta\lambda\big)\end{aligned} \tag{3.109}$$

$$\begin{aligned}\approx -\gamma \big(2.49 \times 10^{-4}\,\bar{\lambda}_{max}^3 + 1.57 \times 10^{-7}\bar{\lambda}_{max}^2 \\ -0.00225\bar{\lambda}_{\ max}) = -0.3626\gamma\end{aligned} \tag{3.110}$$

These simplifications yield the condition for sign consistency

$$(\bar{\lambda}_{max} + \Delta\lambda)^2(4\sqrt{2}\Delta\lambda + \Delta\lambda^2) = -0.3626\gamma \tag{3.111}$$

$$\approx (4\sqrt{2}\Delta\lambda) \propto -\gamma \tag{3.112}$$

This logic also holds for a $\gamma < 0$ and $\Delta\lambda > 0$. Numerically, this inverse relationship is expressed in Figure 3.4(b). ■

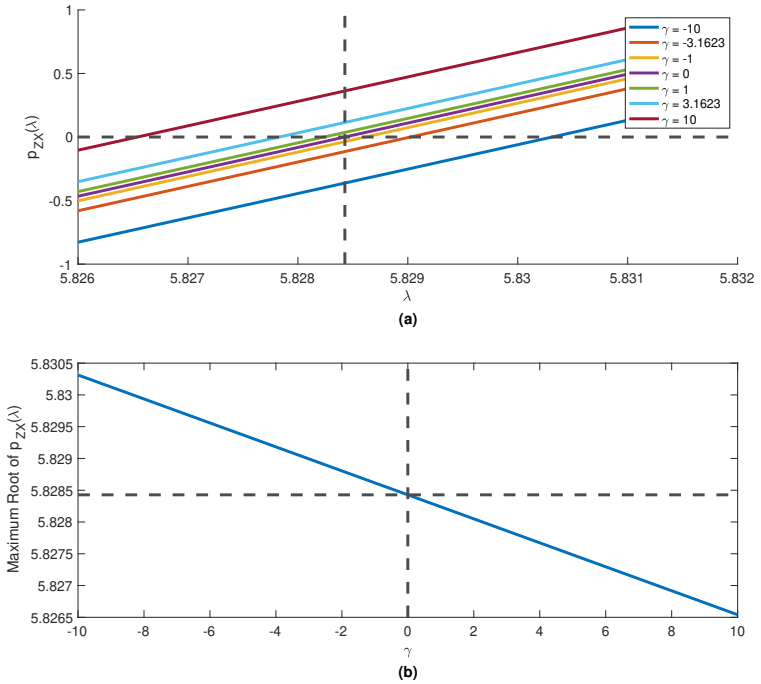

Figure 3.4: (a) Evaluated characteristic polynomials for various values of γ about the nominal maximum eigenvalue of the rigid system. (b) Maximum roots of the characteristic polynomial across various γ. Intersection of dotted lines indicate the nominal values of each parameter.

3.4.4 Numerical Analysis of MIMO Cases

Consider an extension of the preceding analysis to the general MIMO case. The stabilizing solution of an ARE requires the solution of $\frac{2d(m+1)(2d(m+1)+1)}{2}$ simultaneous quadratic equations. While it was feasible for a symbolic math solver to generate a solution for an SISO case with a single flexible mode ($d = 1$, $m = 1 \rightarrow 10$ equations), the addition of an additional dimension ($d = 2$) yields 36 scalar equations. However, leaving the terms in their $d \times d$ blocks, the number of equations left to solve remains 10 (these are matrix equations and will not necessarily be equal to the ones from the SISO case).

Overall the system construction is similar to that of the SISO case:

$$\boldsymbol{A}_{MIMO} = \begin{bmatrix} \boldsymbol{S}_0 & \boldsymbol{0}_2 \\ \boldsymbol{0}_2 & \boldsymbol{S}_1 \end{bmatrix} \bigotimes \boldsymbol{I}_d \in \mathbb{R}^{4d \times 4d} \tag{3.113}$$

$$\boldsymbol{B}_{MIMO} = \begin{bmatrix} \mathbf{0}_d \\ \boldsymbol{R}_0 \\ \mathbf{0}_d \\ \boldsymbol{R}_1 \end{bmatrix} \in \mathbb{R}^{4d \times d} \tag{3.114}$$

$$\boldsymbol{C}_{MIMO} = \begin{bmatrix} \boldsymbol{I}_d & \mathbf{0}_d & \boldsymbol{I}_d & \mathbf{0}_d \end{bmatrix} \in \mathbb{R}^{d \times 4d} \tag{3.115}$$

$$\boldsymbol{D}_{MIMO} = \mathbf{0} \tag{3.116}$$

despite this, the same approximation used for the SISO case will not work. In neglecting the quadratic terms in the ARE, too many terms containing the residual information are neglected. This causes an immediate divergence between the approximated and actual NCF stability margin. This means that the only avenue for analysis is numerical experimentation.

The primary goal of this investigation is to see any emerging trends in the the NCF stability margin. Given a known rigid mode $\left(\boldsymbol{R_0} = \begin{bmatrix} 23.676 & -5.0429 \\ -5.0429 & 4.6265 \end{bmatrix} \right)$ and viscoelastic parameters ($\zeta = 0.2$ and $\omega_n = 10\frac{rad}{s}$) the NCF stability margin can be described as a function of the flexible residual $\boldsymbol{R}_1 = \begin{bmatrix} u & v \\ wu & wv \end{bmatrix}$. The decision to structure the variable residual in this way is so that the rank 1 matrix can be completely described as both a robust posture (that satisfies the outlined properties earlier in the chapter) or a non-robust posture. Illustrated in Figure 3.5 the space of values of u and v that give an RAC (in this case, because $w = 1$, $u = v$ and $u \geq 0$) are similar to the region that is at or exceeds the rigid system NCF stability margin. Largely, we do see that has the flexible residual moves away from the robust posture the NCF stability margin drops.

While not much on its own, this motivates the investigation into how the NCF stability margin varies with a residual that is *guaranteed* to be a robust residual. Redefining the

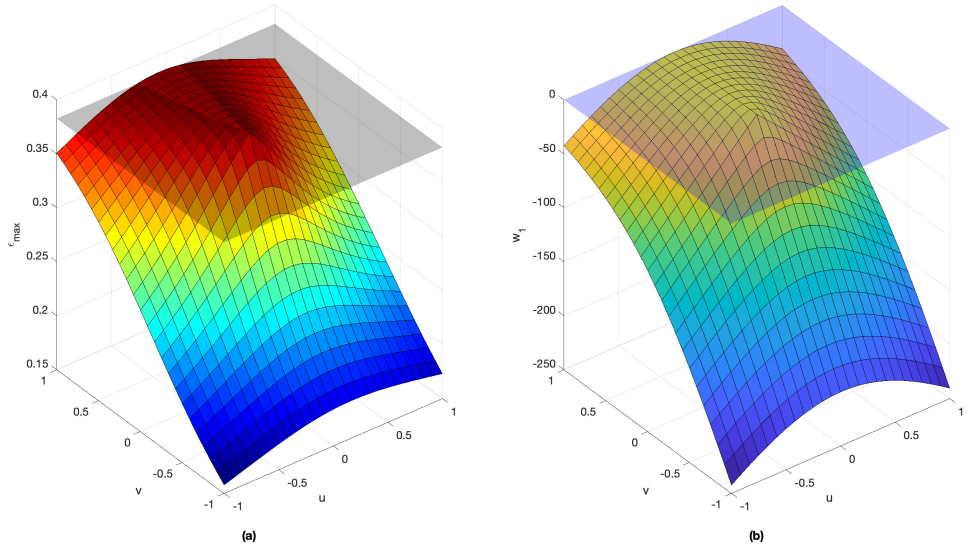

Figure 3.5: (a) NCF stability margin and (b) modal space stability index for residual with $w_1 = 1$. The gray surface in (a) is the value of the NCF stability margin for rigid systems and the blue surface in (b) is the robust condition, $w_1 = 0$.

residual to be $\boldsymbol{R}_1 = \alpha \begin{bmatrix} 1 & \beta \\ \beta & \beta^2 \end{bmatrix}$, one can see that it is rank 1, symmetric. The NCF stability margin can be found for combinations of α and β, shown in Figure 3.6. This supports the existing conjecture: that robust postures have performance that is only as bad as the system's rigid mode (within the context of the NCF stability margin). What is interesting with this data is that there are two points on the plot that are fixed for scaling in the residual (α) and for scaling in the rigid mode. Being that this is invariant with respect to the rigid mode, these points are likely related to the underlying structure of the rigid mode. It is found that when the image of the flexible mode is colinear with a principal axis (eigenvector) of the rigid mode, the NCF stability margin takes its rigid-system value.

Simultaneous Diagonalization of Modes

It was stated previously that when the residual projects on to the principal axes of the rigid mode, the system's NCF stability margin is equivalent to the rigid case. This can be shown simply given the eigenbasis $\boldsymbol{E}$ and diagonal matrix with eigenvalues $\boldsymbol{\Lambda}$ of the rigid mode.

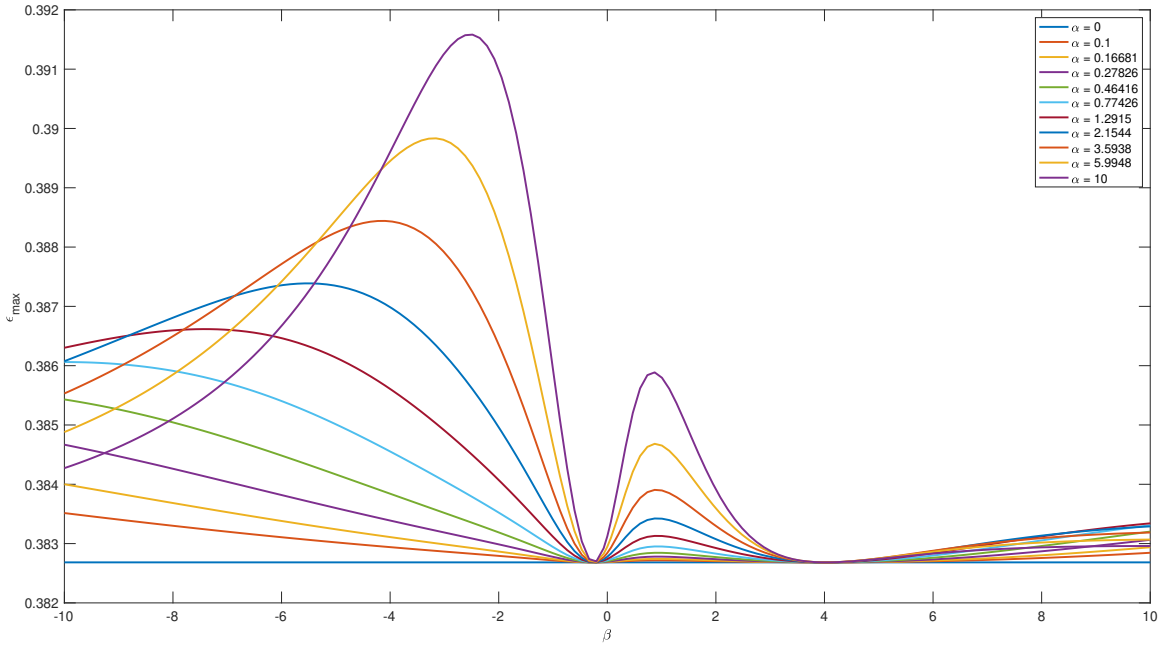

Figure 3.6: NCF stability margin for guaranteed robust postures. Baseline NCF stability margin for rigid systems is equivalent to case of $\alpha = 0$.

Given the MIMO transfer function representation of the flexi-rigid system:

$$\boldsymbol{G}(s) = \frac{\boldsymbol{R}_0}{s^2} + \frac{\boldsymbol{R}_1}{s^2 + 2\zeta\omega_n + \omega_n^2} \tag{3.117}$$

$$= \frac{\boldsymbol{E}\boldsymbol{\Lambda}\boldsymbol{E}^{-1}}{s^2} + \frac{\boldsymbol{R}_1}{s^2 + 2\zeta\omega_n + \omega_n^2} \tag{3.118}$$

if the residual projects on to a principal axis of the rigid mode, the residual must be generated through the outer-product of the associated eigenvector. Mathematically this takes the form of: $\boldsymbol{R}_1 = \delta\boldsymbol{E}\boldsymbol{P}\boldsymbol{E}^{-1}$ where δ is a constant factor to handle scaling of the residual and $\boldsymbol{P}$ is a diagonal selection matrix to select the correct eigenvector. Substituting this into the above:

$$\boldsymbol{G}(s) = \frac{\boldsymbol{E}\boldsymbol{\Lambda}\boldsymbol{E}^{-1}}{s^2} + \frac{\delta\boldsymbol{E}\boldsymbol{P}\boldsymbol{E}^{-1}}{s^2 + 2\zeta\omega_n + \omega_n^2} \tag{3.119}$$

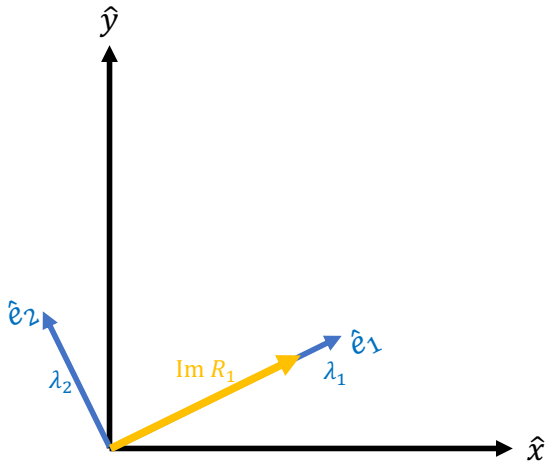

Figure 3.7: Simultaneous diagonalization of modes for the case of an orthogonal eigenbasis of the rigid mode ($\lambda_1, \hat{e}_1$ and $\lambda_2, \hat{e}_2$) with the task-space denoted by ($\hat{x}, \hat{y}$)

the basis can be changed from the task-space to the eigenspace of the rigid mode. This makes a diagonal matrix transfer function that is similar to the original $\boldsymbol{G}(s)$.

$$\boldsymbol{G'}(s) = \boldsymbol{E}^{-1}\boldsymbol{G}(s)\boldsymbol{E} = \frac{\boldsymbol{\Lambda}}{s^2} + \frac{\delta \boldsymbol{P}}{s^2 + 2\zeta\omega_n + \omega_n^2} \tag{3.120}$$

This leads to an interesting special case. Should the eigenbasis of the rigid mode be orthogonal (like in Figure 3.7, and as guaranteed for symmetric matrices by the Spectral Theorem), the diagonal transfer function can be decoupled and treated as individual SISO systems (with a rigid subsystem, $G_r(s)$, and a flexible subsystem, $G_f(s)$):

$$\boldsymbol{G'}(s) = \begin{bmatrix} G_r(s) & 0 \\ 0 & G_f(s) \end{bmatrix} \tag{3.121}$$

These subsystems have their own state-space matrices and the aggregate system, in the state-space can be represented, with appropriate sizes, as:

$$\boldsymbol{A'} = \begin{bmatrix} \boldsymbol{A}_r & \boldsymbol{0} \\ \boldsymbol{0} & \boldsymbol{A}_f \end{bmatrix} \tag{3.122}$$

$$\boldsymbol{B'} = \begin{bmatrix} \boldsymbol{B}_r & \boldsymbol{0} \\ \boldsymbol{0} & \boldsymbol{B}_f \end{bmatrix} \tag{3.123}$$

$$\boldsymbol{C'} = \begin{bmatrix} \boldsymbol{C}_r & \boldsymbol{0} \\ \boldsymbol{0} & \boldsymbol{C}_f \end{bmatrix} \tag{3.124}$$

Substituting these into the GFARE and GCARE in order to calculate the NCF stability margin. Due to the decoupled dynamics between the two subsystems, it is reasonable to assume the solutions $\boldsymbol{Z'}$ and $\boldsymbol{X'}$ are block diagonal:

$$\begin{aligned} &\begin{bmatrix} \boldsymbol{A}_r & \boldsymbol{0} \\ \boldsymbol{0} & \boldsymbol{A}_f \end{bmatrix} \begin{bmatrix} \boldsymbol{Z}_r & \boldsymbol{0} \\ \boldsymbol{0} & \boldsymbol{Z}_f \end{bmatrix} + \begin{bmatrix} \boldsymbol{Z}_r & \boldsymbol{0} \\ \boldsymbol{0} & \boldsymbol{Z}_f \end{bmatrix} \begin{bmatrix} \boldsymbol{A}_r^T & \boldsymbol{0} \\ \boldsymbol{0} & \boldsymbol{A}_f^T \end{bmatrix} \\ &\quad - \begin{bmatrix} \boldsymbol{Z}_r & \boldsymbol{0} \\ \boldsymbol{0} & \boldsymbol{Z}_f \end{bmatrix} \begin{bmatrix} \boldsymbol{C}_r^T \boldsymbol{C}_r & \boldsymbol{0} \\ \boldsymbol{0} & \boldsymbol{C}_f^T \boldsymbol{C}_f \end{bmatrix} \begin{bmatrix} \boldsymbol{Z}_r & \boldsymbol{0} \\ \boldsymbol{0} & \boldsymbol{Z}_f \end{bmatrix} \\ &\quad + \begin{bmatrix} \boldsymbol{B}_r \boldsymbol{B}_r^T & \boldsymbol{0} \\ \boldsymbol{0} & \boldsymbol{B}_f \boldsymbol{B}_f^T \end{bmatrix} = \boldsymbol{0} \end{aligned} \tag{3.125}$$

$$\begin{aligned} &\begin{bmatrix} \boldsymbol{A}_r^T & \boldsymbol{0} \\ \boldsymbol{0} & \boldsymbol{A}_f^T \end{bmatrix} \begin{bmatrix} \boldsymbol{X}_r & \boldsymbol{0} \\ \boldsymbol{0} & \boldsymbol{X}_f \end{bmatrix} + \begin{bmatrix} \boldsymbol{X}_r & \boldsymbol{0} \\ \boldsymbol{0} & \boldsymbol{X}_f \end{bmatrix} \begin{bmatrix} \boldsymbol{A}_r & \boldsymbol{0} \\ \boldsymbol{0} & \boldsymbol{A}_f \end{bmatrix} \\ &\quad - \begin{bmatrix} \boldsymbol{X}_r & \boldsymbol{0} \\ \boldsymbol{0} & \boldsymbol{X}_f \end{bmatrix} \begin{bmatrix} \boldsymbol{B}_r \boldsymbol{B}_r^T & \boldsymbol{0} \\ \boldsymbol{0} & \boldsymbol{B}_f \boldsymbol{B}_f^T \end{bmatrix} \begin{bmatrix} \boldsymbol{X}_r & \boldsymbol{0} \\ \boldsymbol{0} & \boldsymbol{X}_f \end{bmatrix} \\ &\quad + \begin{bmatrix} \boldsymbol{C}_r^T \boldsymbol{C}_r & \boldsymbol{0} \\ \boldsymbol{0} & \boldsymbol{C}_f^T \boldsymbol{C}_f \end{bmatrix} = \boldsymbol{0} \end{aligned} \tag{3.126}$$

Explicitly, the solutions of these ARE's are not important at this point. Looking first at the matrix product $\boldsymbol{ZX'}$ and its characteristic equation,

$$\boldsymbol{ZX'} = \begin{bmatrix} \boldsymbol{Z}_r \boldsymbol{X}_r & \boldsymbol{0} \\ \boldsymbol{0} & \boldsymbol{Z}_f \boldsymbol{X}_f \end{bmatrix} \tag{3.127}$$

$$\mathrm{p}_{\boldsymbol{Z}\boldsymbol{X}'}(\lambda) = \det(\boldsymbol{Z}_r\boldsymbol{X}_r - \lambda\boldsymbol{I})\det(\boldsymbol{Z}_f\boldsymbol{X}_f - \lambda\boldsymbol{I}) \tag{3.128}$$

$$= \mathrm{p}_{\boldsymbol{Z}\boldsymbol{X}_r}(\lambda)\,\mathrm{p}_{\boldsymbol{Z}\boldsymbol{X}_f}(\lambda) \tag{3.129}$$

It can be seen here that this characteristic equation is the product of the rigid system and the flexible system characteristic equations. Unlike the general case of the MIMO system, we have closed form expressions for both of these characteristic equations. Because these characteristic polynomials are multiplied together, their roots are passed through to the total characteristic equation. This means that the largest root between both equations is the largest root for the aggregate, creating the smallest overall NCF stability margin. This implies for the diagonalized flexi-rigid system NCF robustness is equal to that of its *worst* subsystem.

This is intuitive. Take for instance a cartesian robot; motion in one joint does not influence the other. Extend this concept to a cartesian robot with a flexibility in only one of its axes. While each axis can move independently the aggregate system can only be as robust as its least robust member. This is to say that if that flexibility is *in*-phase, then the system will be as robust as its rigid counterpart, however should that flexibility be out of-phase, we know that the aggregate system would take on the lower NCF stability margin.

Asymmetrical Rigid Modes

Until now the examples given have had symmetrical rigid modes because it is common to see these when using Jacobian transpose control. When inverse control is used there is no guarantee on the symmetry of the rigid mode. The above analysis holds, but as stated it is only viable for rigid modes with orthogonal bases. An arbitrary, asymmetrical rigid mode may be able to simultaneously diagonalize the modes, however the resulting basis may not be orthogonal. This is illustrated in Figure 3.8 where the eigenbasis displayed is clearly not orthogonal. The effects of this asymmetry are seen when looking at the NCF stability margin as compared to various guaranteed robust postures. Looking at Figure 3.9 we see

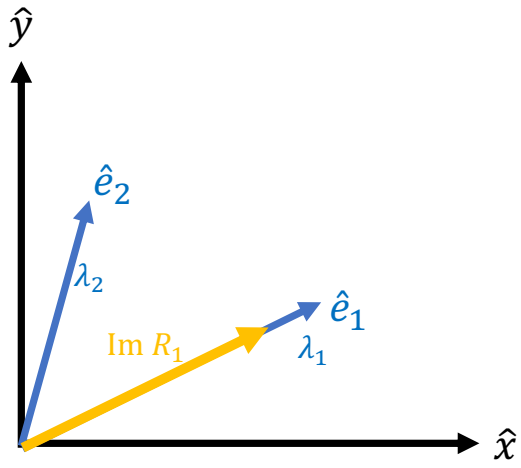

Figure 3.8: Simultaneous diagonalization of modes for the case of an non-orthogonal eigenbasis of an asymmetrical rigid mode ($\lambda_1, \hat{e}_1$ and $\lambda_2, \hat{e}_2$) with the task-space denoted by ($\hat{x}, \hat{y}$)

that there are several points where the NCF stability margin takes on its rigid-system value, and these points do occur when the residual projects on to the principal axes of the rigid mode, however there is clearly a region where the robust system performs *worse* than the rigid system.

It was mentioned in the previous subsection that the for simultaneous diagonalization one can treat the MIMO system as an aggregate of SISO systems and then take the lower NCF stability margin as the margin for the aggregate. In the case of an asymmetric rigid mode, the non-orthogonal basis creates a subset of postures where the flexible mode with a robust residual is out of phase in its subsystem and the NCF stability drops below the nominal value. Returning to the idea of the cartesian robot, this would be similar to the two axes of the machine being not-quite orthogonal. Depending on the degree of non-orthogonality, motion would feed through the system and potentially excite motion in both axes.

When considering the eigenspace of the manipulator with asymmetric rigid mode the dynamics are "skewed" in the transformation, creating the possibility for an unequal distribution of effort in the task space. While these postures exist in the numerical analysis, the regions of subnominal robustness are not realistic postures for real manipulator systems. Therefore, this can be considered to be an exception to the theorem outlined in the

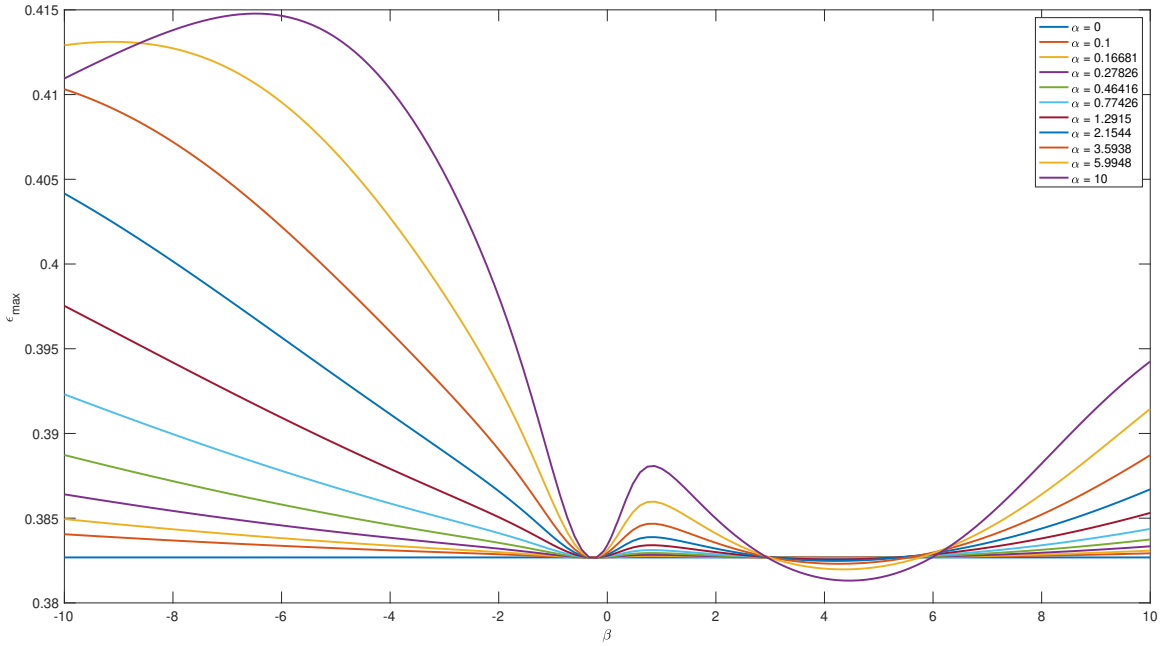

Figure 3.9: NCF stability margin for guaranteed robust postures for a system with an asymmetric rigid mode, $\boldsymbol{R}_0 = \begin{bmatrix} 1 & 3 \\ 2 & 10 \end{bmatrix}$. Baseline NCF stability margin for rigid systems is equivalent to case of $\alpha = 0$.

beginning of the chapter as it is unlikely to appear in practice.

3.5 Contribution of Work

The theory presented in this chapter is integral to the application of these stability metrics to stabilize manipulators. Conditions where outlined to exist and remain in a robust configuration with respect to the modal space stability index. The constant NCF stability margin is presented for all double-integrator systems, and this was demonstrated to be the minimum NCF stability for systems in robust configurations. Moving forward it is possible to use these properties to lever redundancy in the mobile manipulation systems to pose the robot in a locally optimal posture without compromising the reachability of its workspace.

This work, in part, has been submitted to *Journal of Dynamic Systems, Measurement and Control* and is currently under review, [70].

CHAPTER 4
ROBOT MANIPULATOR CASE STUDIES

4.1 Motivation

The material in this chapter is to be seen as a compilation of the theory presented in chapter 3 as applied to various styles of manipulator system. While this will not invoke new material, it will highlight the applications of the presented principles. To this end, the considered systems will be planar systems, for ease of analysis, and will be what can be considered to be "canonical" manipulator systems. Namely the "RR", "RP", and "parallel-drive" planar manipulators. There will also be a brief discussion on the extension of this theory beyond the context of flexible bases and will instead look at flexible link systems.

Each section will include a comparison between the normalized coprime factor and modal-passivity based robustness metrics, an examination of a slice of the workspace around a robust posture, and the conditions necessary to stay in an robust posture as outlined in subsection 3.3.4.

4.2 The RR Manipulator

In most robotics curricula the serial-link RR manipulator is used as an introductory example due to its well established dynamics. Shown in Figure 4.1 this target system has a singular rotational viscoelasticity with two rigid modes. The decision to look at a system with only two links (nonredundant systems) is to ensure that, when only considering end-point position, the manipulator Jacobian is square, which will allow for the examination of Jacobian inverse control without needing to modify the Jacobian. For this system, we consider three states: $[\theta_b, \theta_1, \theta_2]^T$ with the last two being actively driven.

While the system description in the previous chapter will be suitable for the simulation

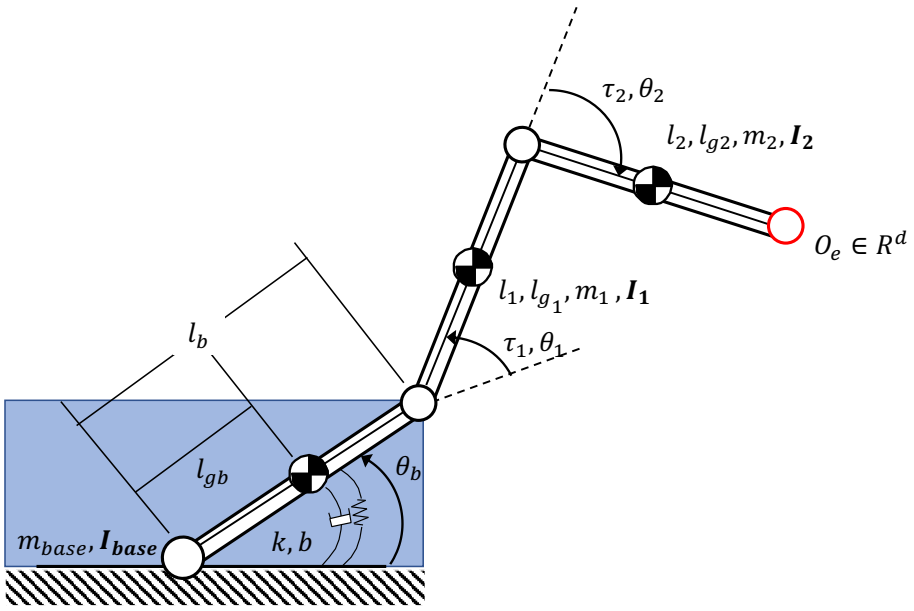

Figure 4.1: Geometric diagram of RR manipulator with single flexibility in its base, shown by generic volume in blue.

of these systems, it is sufficient to adapt the state space system from the dynamics of the system directly such that (noting that all matrices are functions of the system posture):

$$\boldsymbol{A} = \begin{bmatrix} \boldsymbol{O}_3 & \boldsymbol{I}_3 \\ -\boldsymbol{M}^{-1}\boldsymbol{K} & -\boldsymbol{M}^{-1}\boldsymbol{D} \end{bmatrix} \in \mathbb{R}^{6\times 6} \tag{4.1}$$

$$\boldsymbol{B} = \begin{bmatrix} \boldsymbol{O}^{3\times 2} \\ \boldsymbol{M}^{-1} \begin{bmatrix} \boldsymbol{O}^{1\times 2} \\ \boldsymbol{I}^{2\times 2} \end{bmatrix} \end{bmatrix} \boldsymbol{T} \in \mathbb{R}^{6\times 2} \tag{4.2}$$

$$\boldsymbol{C} = \begin{bmatrix} \boldsymbol{J} & \boldsymbol{O} \end{bmatrix} \in \mathbb{R}^{2\times 6} \tag{4.3}$$

where the system parameters $\boldsymbol{D}$ and $\boldsymbol{K}$ are the square viscosity and stiffness matrices with the state-viscosity and -stiffness along their diagonals. The matrix $\boldsymbol{T}$ is chosen as a map between the input and joint-space of the manipualtor system. For the cases considered this is either $\boldsymbol{J}_v^T$ or $\boldsymbol{J}_v^{-1}$, with $\boldsymbol{J}_v$ being the rigid-body Jacobian. The inertia matrix, $\boldsymbol{M} = \boldsymbol{M}^T \geq 0$, and the full-system Jacobian, $\boldsymbol{J}$, are given by the particular robot struc-

ture. It should be noted that the preceding variables are dependent on the robot posture.

Utilizing the two robustness measures discussed in the previous chapter, the workspace

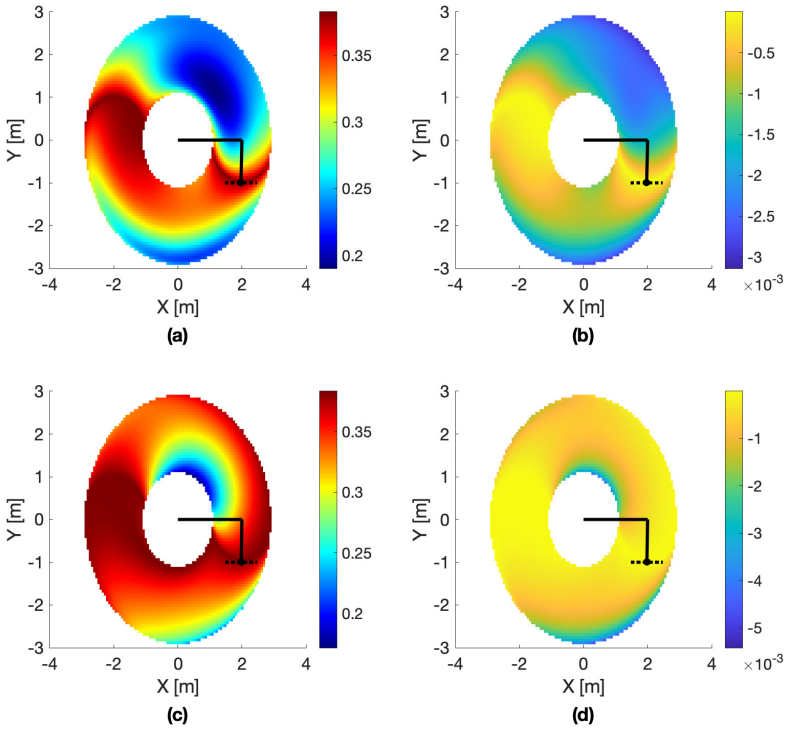

Figure 4.2: NCF Stability (red) and modal passivity index (yellow) across the workspace of a planar RR manipulator with a single rotational flexibility under Jacobian (a-b) transpose and (c-d) inverse control. Posture shown is highly robust.

of the linearized plant can be described in terms of high and and low robustness, shown in Figure 4.2. Qualitatively it is easy to see that the two metrics maximize in similar places, this can be further explored by looking at a local neighborhood of this posture, shown in Figure 4.3. Not only do the the two metrics follow the same overall shape, this demonstrates that a small error in end-point position will allow the manipulator to remain in an a relatively robust posture. Furthermore, this plot illustrates that these ideal postures occur as s continuum within the workspace; that the robust postures are continuous throughout the workspace, as shown in [71].

Furthermore, within the neighborhoods displayed in Figure 4.3, the black regions can

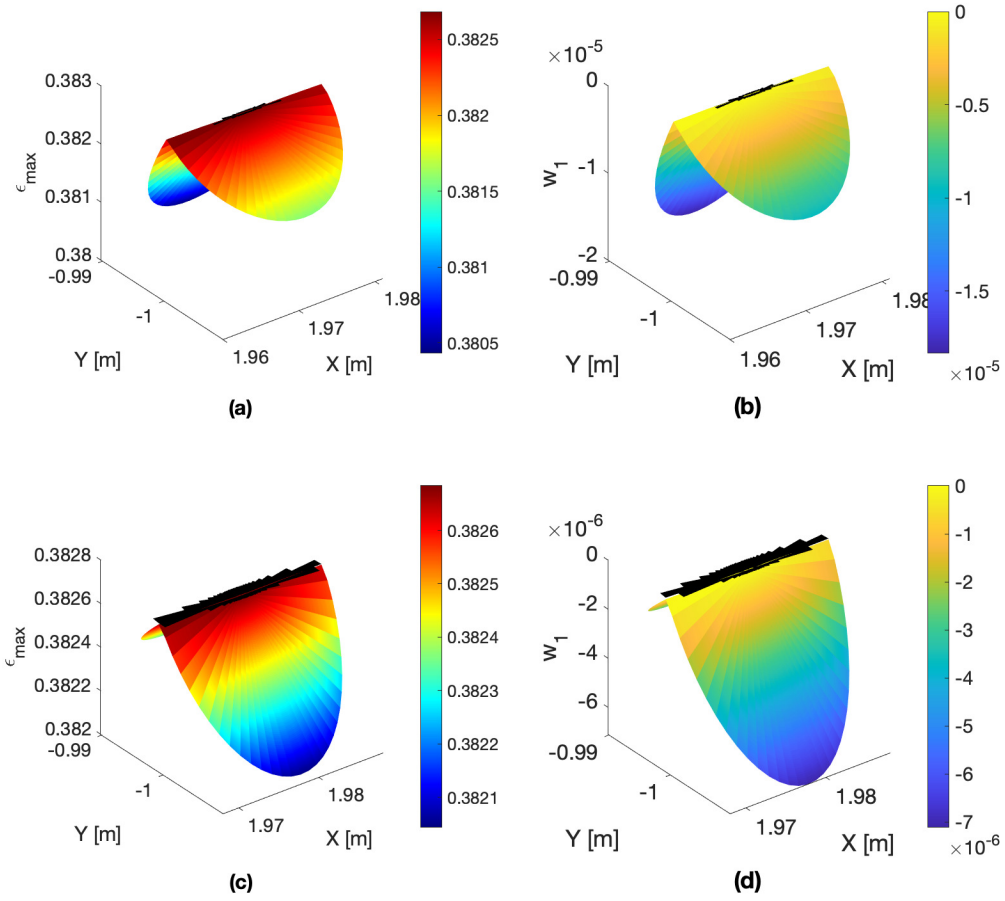

Figure 4.3: NCF Stability (red) and modal passivity index (yellow) around a chosen end-point of a planar RR manipulator with a single rotational flexibility under Jacobian (a-b) transpose and (c-d) inverse control. Posture shown is highly robust and drawn in Figure 4.2. Black regions are postures close to the ideal stability margins for each metric.

be seen approximately following the "0" contour in the figures detailing the inner product condition (Equation 3.31), shown in Figure 4.4. Should the manipualtor end-point be displaced by some small disturbance, this information shows the eligibility for that new posture to be robust.

The preceding discussion has assumed that the manipulator is already in a robust posture. As a result there exists a finite set of displacements that will allow the manipulator to remain in a robust posture. However, when considering a posture that is not robust, it may become necessary to transit to a robust posture. Looking at a slice of the RR manipulator

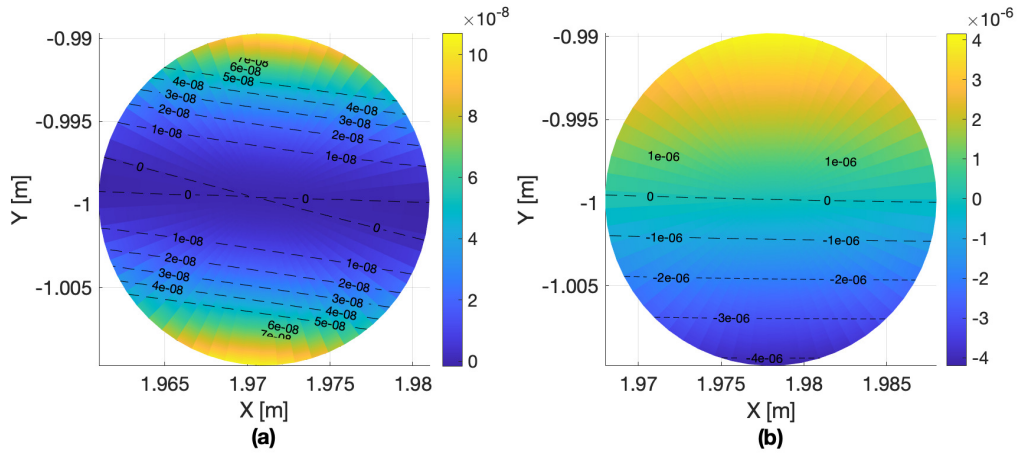

Figure 4.4: Inner product condition to remain in a robust posture around a chosen end-point of a planar RR manipulator with a single rotational flexibility under Jacobian (a) transpose and (b) inverse control. Posture shown is highly robust and drawn in Figure 4.2. When this metric is 0 the manipulator will remain in a robust posture at that location.

workspace, shown in Figure 4.5, it is evident that through shifting the posture along the x-axis, both stability margins can be increased. Because the goal in this situation would be to maximize the desired stability margin while maintaining a particular point in the inertial frame (e.g. a grasping task), in order to take advantage of this it is best that the system have some floating base so that the manipulator can reorient itself in its joint space without changing its inertial-space position. These regions of higher robustness, because they indicate passivity of the flexible modes, allow for higher feedback gain to be used in the control loop. The higher feedback gain enables the use of more aggressive controllers that could have more desirable temporal performance.

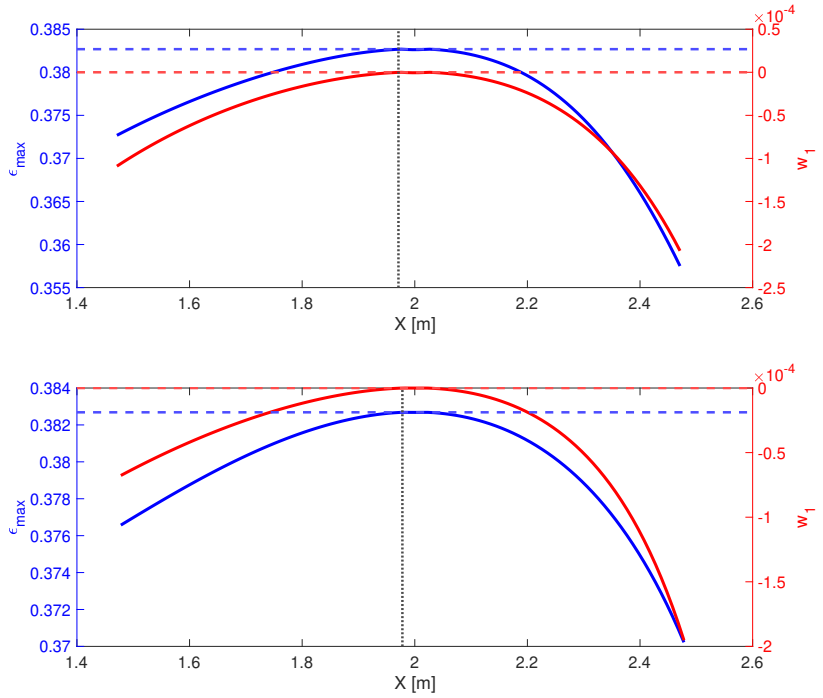

Figure 4.5: NCF stability (blue) and modal-space passivity index (red) along a slice of the workspace of a planar RR manipulator with a single rotational flexibility under Jacobian (a) transpose and (b) inverse control. Slice is drawn in black dotted line on Figure 4.2.

4.3 The RP Manipulator

As with the RR manipulator, we can look at the workspace of an RR manipulator, again with a single rotational flexible mode, with diagram shown in Figure 4.6. Despite having the same overall system structure, (Equation 4.3), it can be seen that the shape of the stability surfaces differs between the RR and RP manipulators. Shown in Figure 4.7, these surfaces take on a flatter appearance once the length of the prismatic slider begins to dominate the size of the system. Furthermore, we can see that when the manipulator is folded over its flexible base (when the end-point is at a negative x value).

The region of decreased robustness in the right-half plane of the workspace occurs due to the ratio of mass/inertia of manipulator to the base. When the base is more massive than the

The local neighborhood surrounding the drawn posture in the workspace figure can also be analyzed, Figure 4.8. This figure, like in the RP manipulator, highlights that within

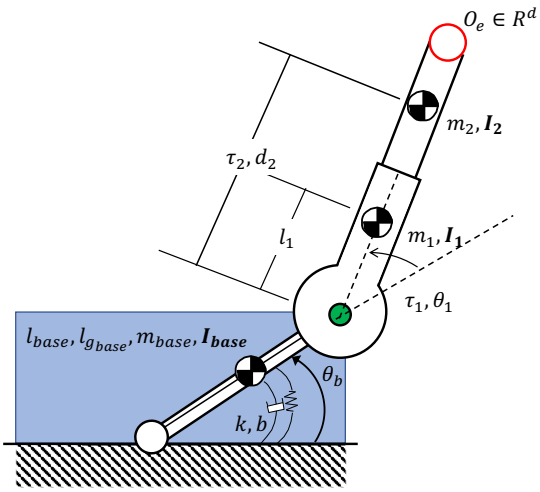

Figure 4.6: Geometric diagram of RP manipulator with single flexibility in its base, shown by generic volume in blue.

small areas of high robustness, the NCF stability margin and the modal passivity index follow roughly the same path. While the black regions in this figure are *regions* as opposed to *curves*, it should be noted that these regions appear due proximity to the ideal robustness values. Because the systems discussed are linear, uncontrollability and unobservability happen along specific curves within the workspace (not regions), and as such the ideal robustness should exist along a curve.

Within these neighborhoods the inner product condition can also be examined, shown in Figure 4.9. The 0 contour for this structure runs along the boundary shown on the edge of the black region in Figure 4.8, as expected, but also runs perpendicular or nearly perpendicular to it.

Looking at the workspace at a wider-scale, along the dotted path running through the robust posture, we can see that there comes a point where both stability margins maximize. It would be in this outer region where it would be advantageous to operate the RP manipulator.

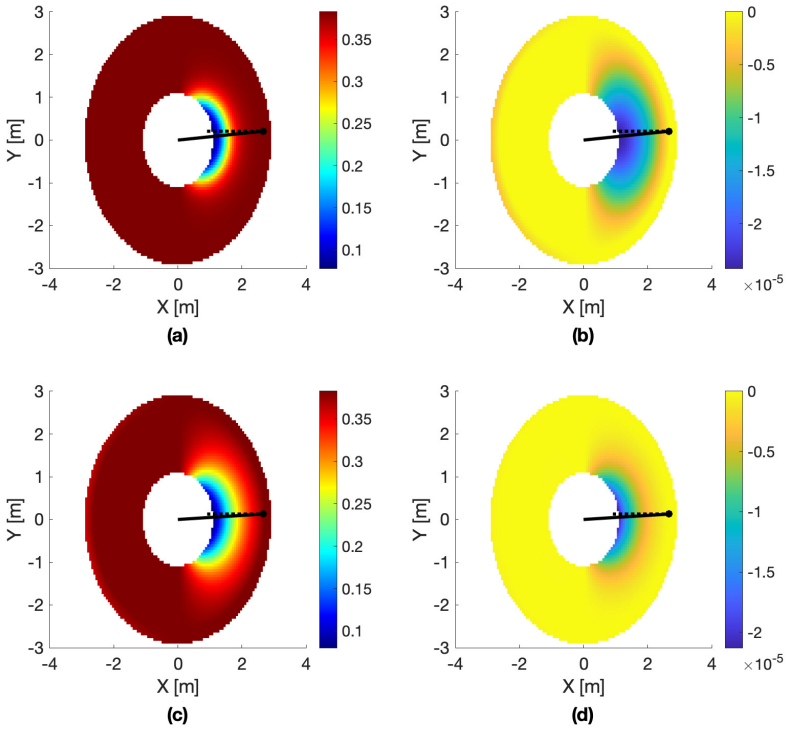

Figure 4.7: NCF Stability (red) and modal passivity index (yellow) across the workspace of a planar RP manipulator with a single rotational flexibility under Jacobian (a-b) transpose and (c-d) inverse control. Posture shown is highly robust.

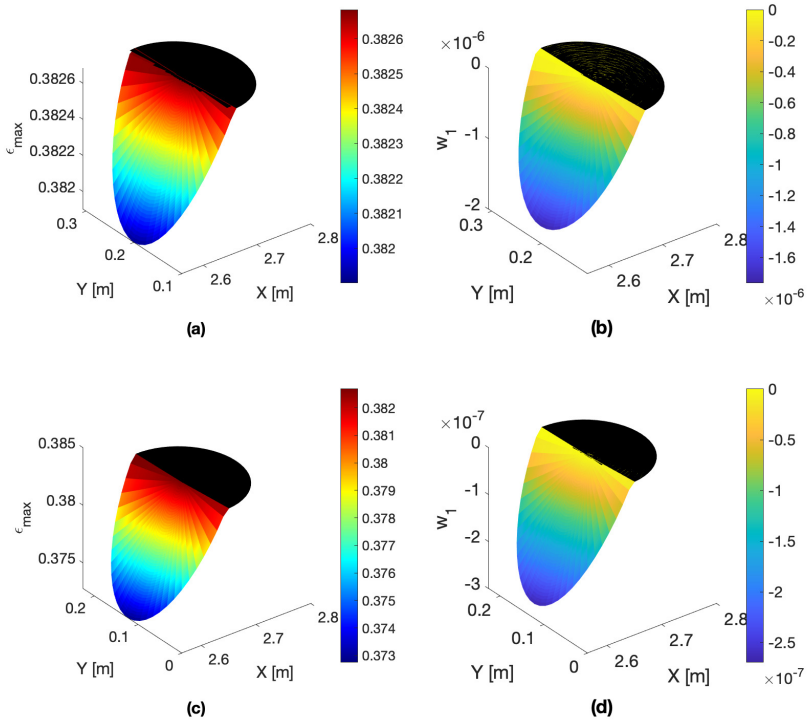

Figure 4.8: NCF Stability (red) and modal passivity index (yellow) around a chosen end-point of a planar RP manipulator with a single rotational flexibility under Jacobian (a-b) transpose and (c-d) inverse control. Posture shown is highly robust and drawn in Figure 4.7. Black regions are postures close to the ideal stability margins for each metric.

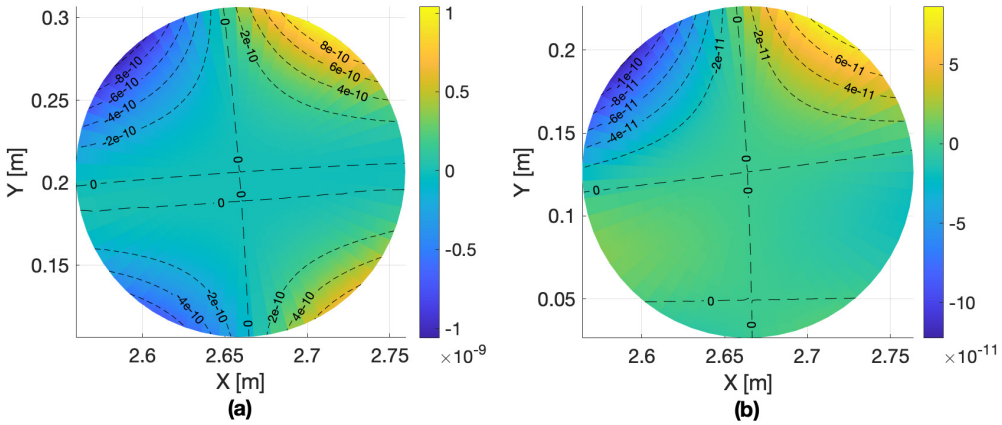

Figure 4.9: Inner product condition to remain in a robust posture around a chosen end-point of a planar RP manipulator with a single rotational flexibility under Jacobian (a) transpose and (b) inverse control. Posture shown is highly robust and drawn in Figure 4.7. When this metric is 0 the manipulator will remain in a robust posture at that location.

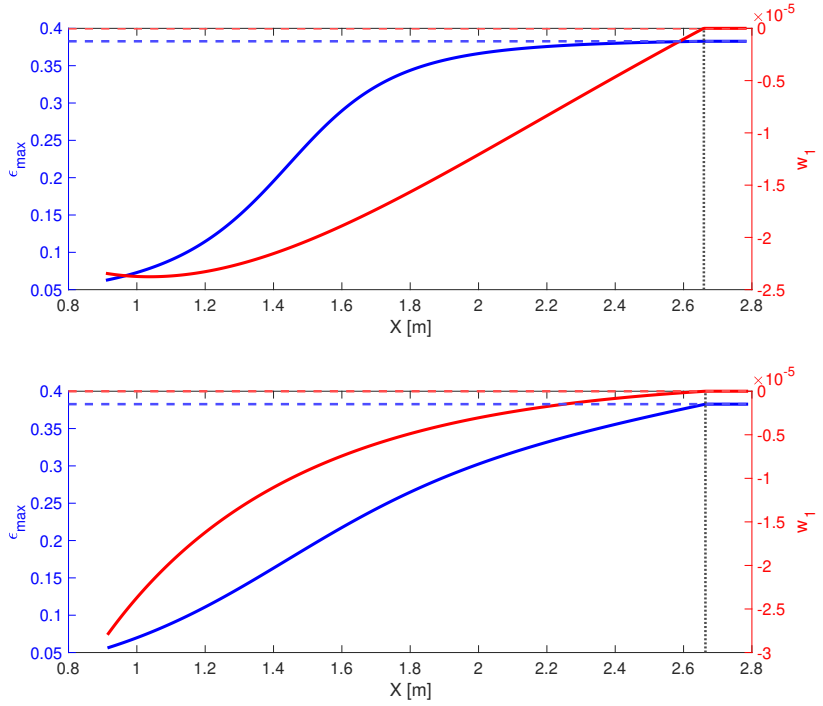

Figure 4.10: NCF stability (blue) and modal-space passivity index (red) along a slice of the workspace of a planar RP manipulator with a single rotational flexibility under Jacobian (a) transpose and (b) inverse control. Slice is drawn in black dotted line on Figure 4.7.

4.4 Parallel-Drive Manipulator

Lastly, take for instance the parallel-drive planar manipulator upon a base with rotational flexibility, illustrated in Figure 4.11. This manipulator, like the others will be described by the same overall system construction. The difference here, is that rather than having two links in its rigid manipulator, the parallel-drive manipulator has four. This allows for the selection of links to cancel the off-diagonal elements in its mass matrix, allowing for the decoupling of the dynamics in the rigid portion of the manipulator.

As with the previous two manipulator structures, its workspace can be characterized

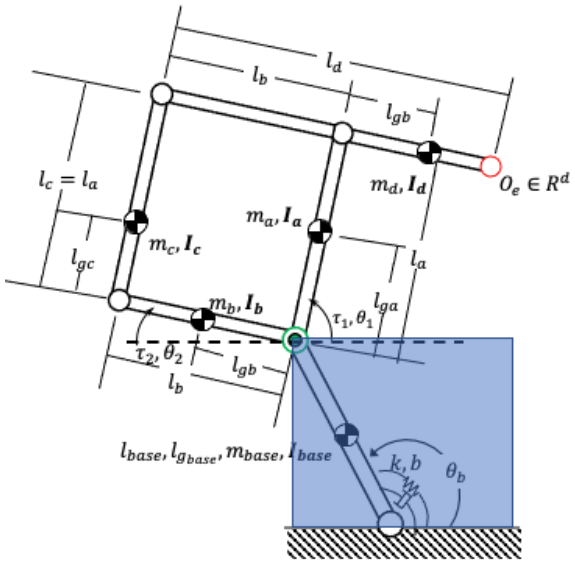

Figure 4.11: Geometric diagram of parallel-drive manipulator with single flexibility in its base, shown by generic volume in blue.

and regions of high robustness can be inspected. These figures, similar to those of the preceding structures, can be seen in Figure 4.12, Figure 4.13, and Figure 4.14. Interestingly, because it is possible to decouple the planar dynamics of this manipulator, it is possible to exceed the rigid-system value of the NCF stability margin. This is demonstrated in Figure 4.13 by the stability surface going above the black region. While we see an NCF robustness higher than that of a rigid system, it the modal space stability index, w_1 remains below its maximum. Furthermore, as with the the previous manipulators, the inner product

condition is satisfied for the parallel-drive manipulator. Slices for the stability metrics also demonstrate that the manipulator can take advantage of planar redundancy to better pose the robot to maximize stability Figure 4.15.

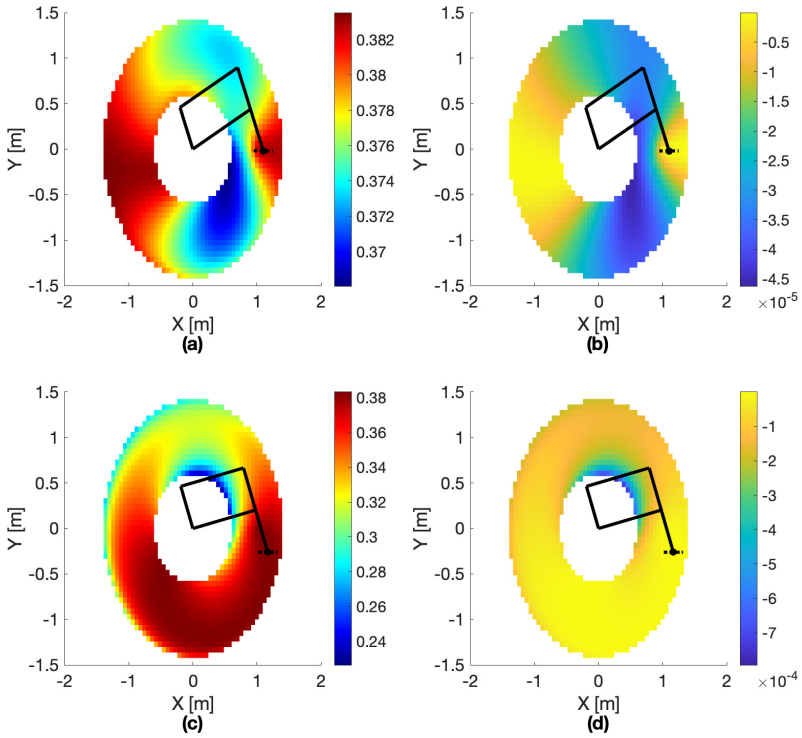

Figure 4.12: NCF Stability (red) and modal passivity index (yellow) across the workspace of a planar parallel-drive manipulator with a single rotational flexibility under Jacobian (a-b) transpose and (c-d) inverse control. Posture shown is highly robust.

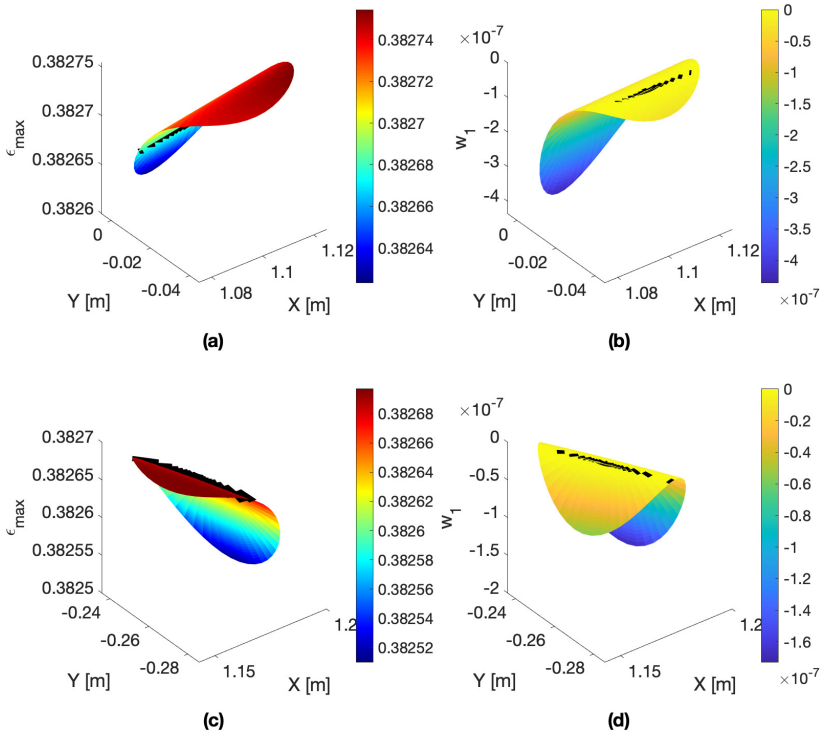

Figure 4.13: NCF Stability (red) and modal passivity index (yellow) around a chosen endpoint of a planar parallel-drive manipulator with a single rotational flexibility under Jacobian (a-b) transpose and (c-d) inverse control. Posture shown is highly robust and drawn in Figure 4.7. Black regions are postures close to the ideal stability margins for each metric.

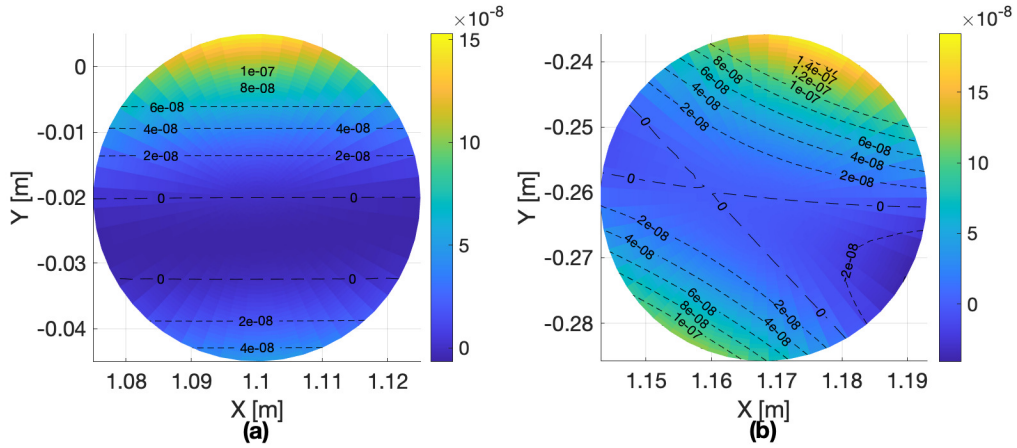

Figure 4.14: Inner product condition to remain in a robust posture around a chosen endpoint of a planar parallel-drive manipulator with a single rotational flexibility under Jacobian (a) transpose and (b) inverse control. Posture shown is highly robust and drawn in Figure 4.12. When this metric is 0 the manipulator will remain in a robust posture at that location.

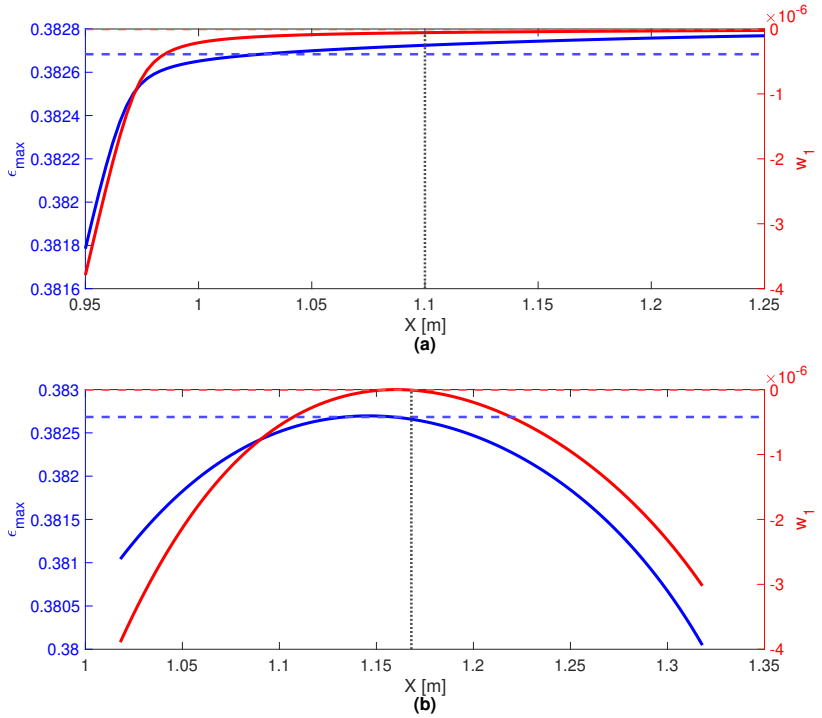

Figure 4.15: NCF stability (blue) and modal-space passivity index (red) along a slice of the workspace of a planar parallel-drive manipulator with a single rotational flexibility under Jacobian (a) transpose and (b) inverse control. Slice is drawn in black dotted line on Figure 4.12.

4.5 Flexible Link Manipulators

Until this point the discussed manipulators were rigid with flexible bases. The base flexibility, while preventing the use of high feedback gain in some postures, does not necessarily preclude the exsitence of passive postures. Flexibility in links, however, creates a situation where the motion in the system induces oscillation in that flexibility. For obvious reasons, this prevents passive postures in the manipulator.

Overall, the system structure matches those of the previous systems, but geometrically the systems differ. An example of a system like this is given in Figure 4.16.

Looking first at the case where the first link is flexible, the stability margins across its

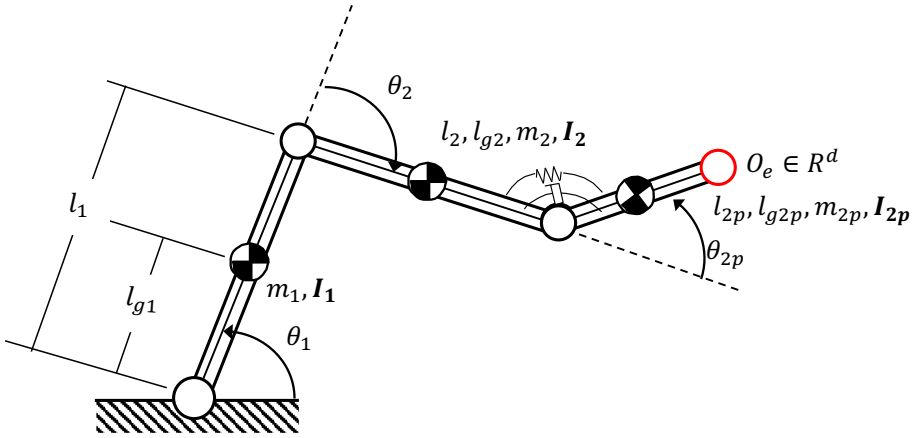

Figure 4.16: Diagram of a planar RR manipulator with a flexibility in its second link.

workspace can be seen in Figure 4.17. Firstly, between the two sets of controller structures, the idea that a manipulator with in-link flexibility has no passive postures is illustrated by the scale on the w_1 indices in (b) and (d). The workspace of the manipulator under each controller does not approach the condition for passivity in either case at any posture. The NCF stability margins for this system highlight that the most robust postures are the traditional velocity singularities of a fully rigid RR manipulator. Within the scope of this work, this information can still be used. Rather than operating the manipulator in the center of its workspace, the control designer can prioritize operating the manipualtor so that its endpoint is nearer to its inner and outer extents. Obviously there are risks to this as operating

a system near its singularities as control in these regions become unpredictable.

The other case for flexible-link RR manipulators is the case where the second link

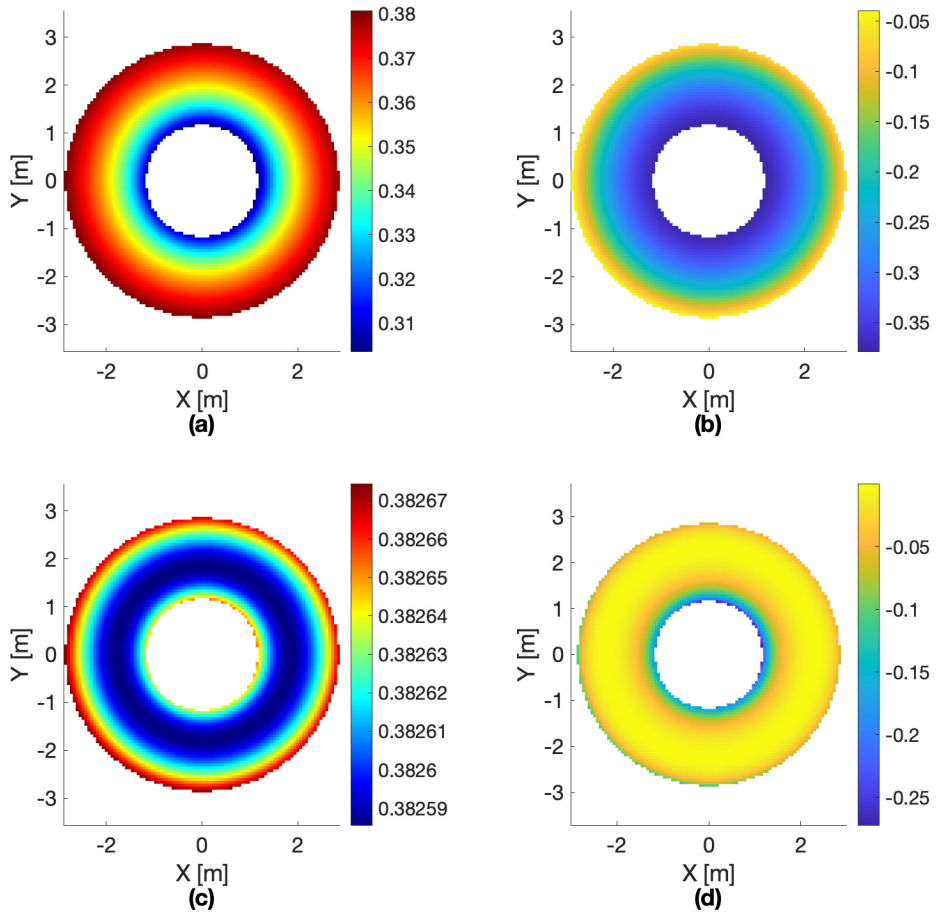

Figure 4.17: NCF Stability (red) and modal passivity index (yellow) across the workspace of an RR manipulator with link-1 flexibility under Jacobian (a-b) transpose and (c-d) inverse control.

is flexible. The link-2 flexibility stability margins have a different shape than the link-1 case. Illustrated in Figure 4.18 there is a "peak" in each stability margin within the usable region of the workspace. When the second link is orthogonal to the first, the manipulator can move in such a way that end-point wrenches that are colinear with the second link do not induce oscillation in the link (only motion from the first joint). Despite this, the overall scale in these stability margins betray this concept. The NCF stability is near zero for both

controllers, which indicates that there do not exist postures that are robust to external disturbances. By the same measure, the modal passivity indices also demonstrate that there are no postures where the flexibility in the second link is passive.

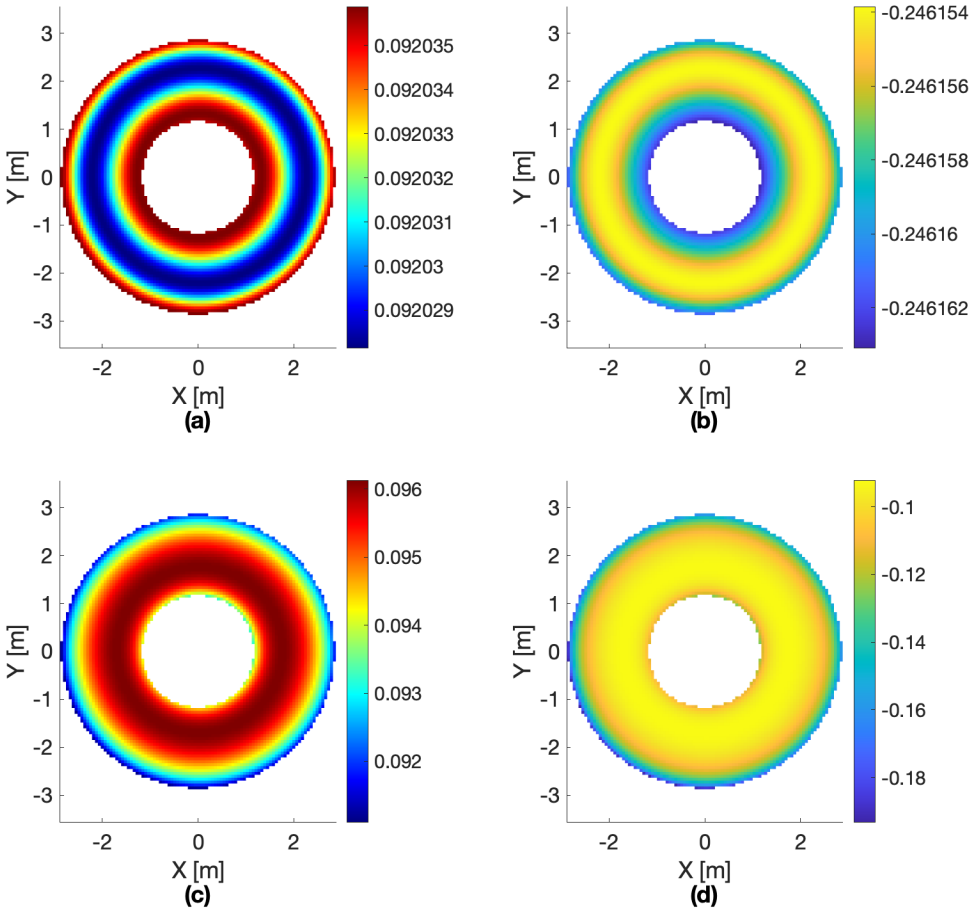

Figure 4.18: NCF Stability (red) and modal passivity index (yellow) across the workspace of an RR manipulator with link-2 flexibility under Jacobian (a-b) transpose and (c-d) inverse control.

4.6 Contribution of Work

The work in this chapter amounts to the demonstration of the stability margins from the preceding chapter as applied to various manipulator structures. Utilizing canonical manip-

ulator examples the application of the NCF and modal-passivity stability metrics are shown to be valid and provide the same information regardless of manipulator structure. When considering redundant systems with these dynamics, it is shown that the generated surfaces can feasibly be sliced to determine the optimal posture about a particular task-space location. The foray into flexible-link manipulators demonstrates that these systems are not robust to induced oscillations from their flexibility not just as a binary, but categorically across their workspaces.

CHAPTER 5

POSTURE-DEPENDENT STABILIZATION FOR REDUNDANT MANIPULATORS WITH BASE FLEXIBILITY

5.1 Problem Statement

The development of first-responder robotics and related technologies have grown considerably as the problems needing to be solved have become more complex [72, 73, 74, 75, 76, 77]. It is clear that the effectiveness of these technologies increases if done *before* an incident, but what about in the short term? This can easily be solved through the retrofitting of existing hardware with control solutions. To address the hardware reliability issues, interfaces can be developed that turn existing construction equipment into mobile robotic manipulators as shown in Figure 5.1. During a collaboration, one of the groups developed wirelessly-operated mechanical interfaces that operates the controls of the conventional excavator for this express purpose [78, 79, 80].

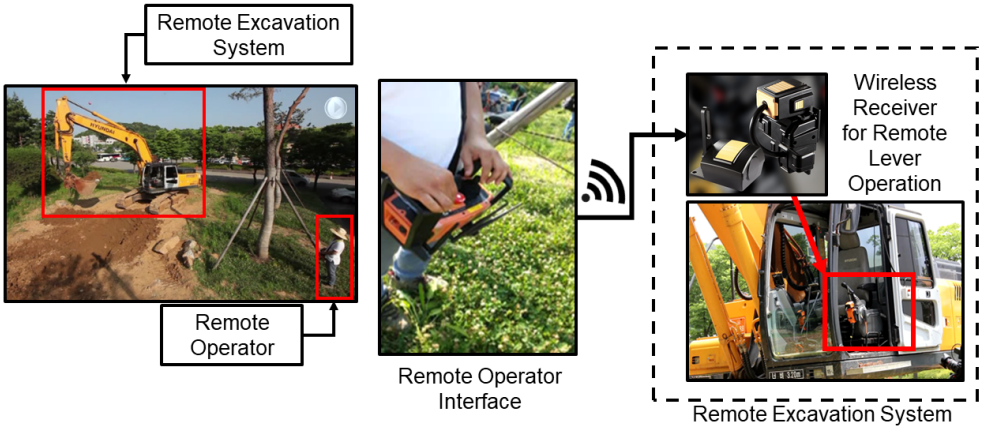

Figure 5.1: Ghost(R) Remote Excavator Control System: Remote operator interface is used to transmit commands to the Ghost(R) system attached to each lever on the remote excavation system. Photos courtesy of ROHAU.

Motion of the upper mechanism of the retrofitted excavator (mobile manipulator) dynamically induces the undercarriage flexibility, resulting in errors in end-point positioning.

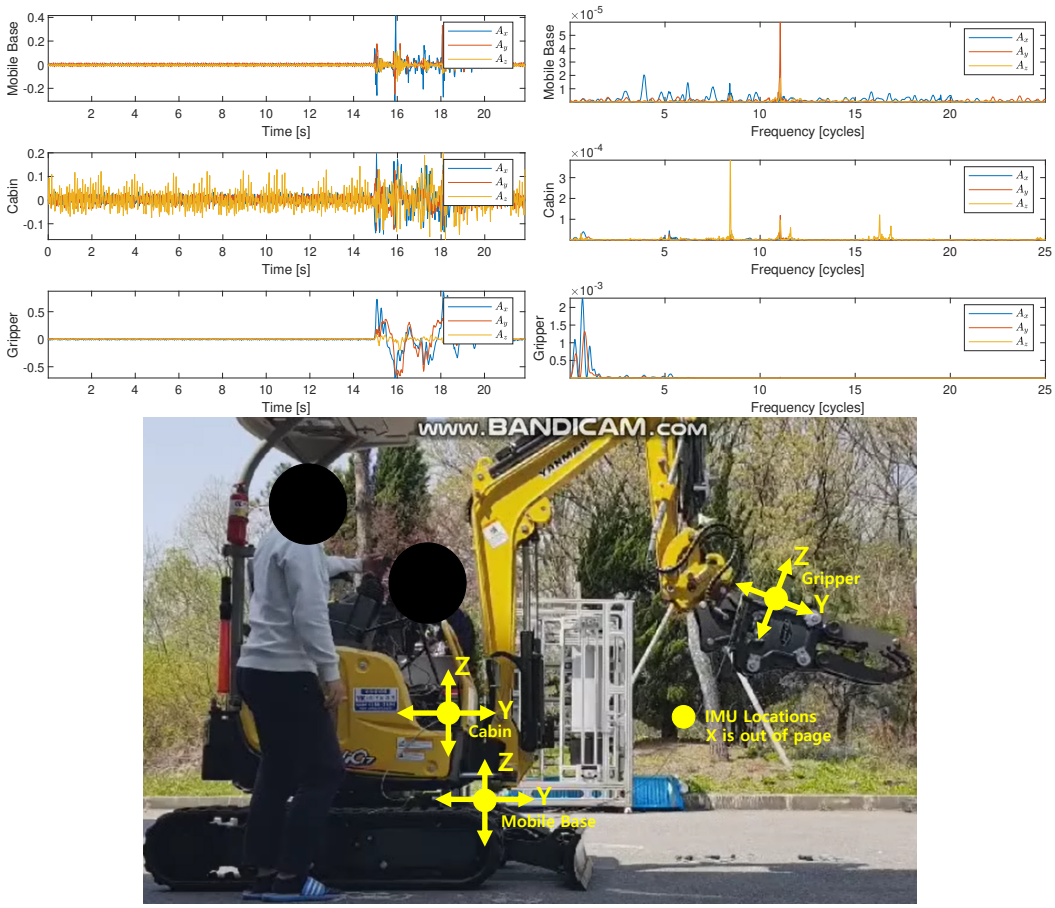

Figure 5.2: Accelerometer data resulting from cabin swing on an excavation system. Curves presented are raw accelerometer data for the x,y, and z axes as well as the frequency spectra of those vibrations.

The undercarriage oscillation and resultant end-point error must be effectively suppressed to accurately position the end-point. Brief high-speed motion testing of a small excavator yielded accelerometer data that demonstrated these induced oscillations upon rotation of the cabin, shown in Figure 5.2. The chattering seen is largely high frequency, however the gripper retains low-frequency oscillation, which is likely to be within the control bandwidth of the system and affect end-point control.

Due to lack of actuation and sensing hardware, end-point feedback control will be done without measuring or modeling of induced base oscillations for practical advantages. To improve robustness of such simple controller implementation, configuration-based stability analysis of a manipulator with an oscillatory base is performed. Once stability margins of

the manipulator workspace have been characterized, it is possible to determine the position of the undercarriage and the posture of the arm such that the task-space feedback control has greater robustness to induced oscillation while maintaining the same position in the task-space.

5.2 Manipulator Model, Dynamics, and Feedback Control

5.2.1 Model

The presented excavator can be, instantaneously, considered to be a two-degree-of-freedom (2DOF) planar manipulator on a base that is flexible in three directions, shown in Figure 5.3, where θ_1 is the base rotation, θ_2 and θ_3 are manipulator joint angles. In the following analysis, the position of the end-point of the arm is considered, and its orientation is not considered. Generally, excavators have an additional degree of freedom between the

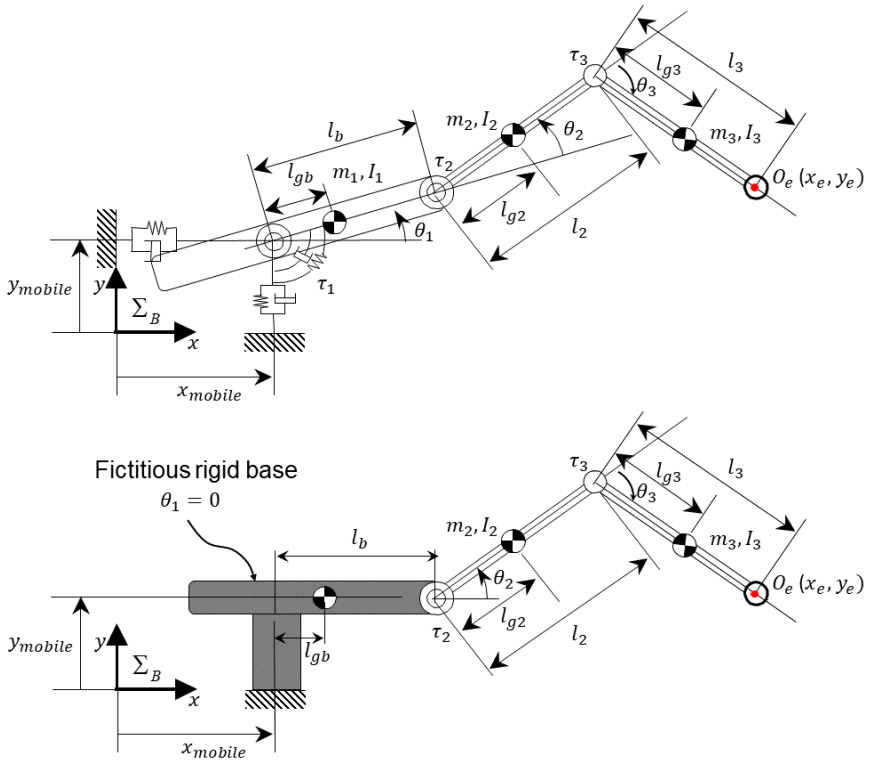

Figure 5.3: Planar manipulator with flexible (used for modeling) and rigid bases (used for control purposes)

arm and bucket which can be used to compensate for orientation, but that will be ignored in this analysis.

Given geometries shown in Figure 5.3, the end-point $\boldsymbol{O}_e = [x_e, y_e]^T$ is represented by a function of a total of five displacements: $\boldsymbol{O}_e = \boldsymbol{r}(x_{mobile}, y_{mobile}, \theta_1, \theta_2, \theta_3)$. Note that θ_1 is passively produced by undercarriage oscillation and is therefore not a control input. In addition, the Jacobian matrix that maps joint angular velocities to end-point velocities is given as

$$\boldsymbol{J} = \begin{bmatrix} 1 & 0 & -l_1 S_1 - l_2 S_{12} - l_3 S_{123} & -l_2 S_{12} - l_3 S_{123} & -l_3 S_{123} \\ 0 & 1 & l_1 C_1 + l_2 C_{12} + l_3 C_{123} & l_2 C_{12} + l_3 C_{123} & l_3 C_{123} \end{bmatrix} \tag{5.1}$$

The trigonometric functions are defined to simplify the description such as $S_a = \sin(\theta_a)$ and $C_{ab} = \cos(\theta_a + \theta_b)$.

5.2.2 Dynamics

The dynamics of the planar manipulator can be described by: $\boldsymbol{\tau} = \boldsymbol{M}(\boldsymbol{q})\ddot{\boldsymbol{q}} + \boldsymbol{H}(\boldsymbol{q}, \dot{\boldsymbol{q}}) + \boldsymbol{N}(\boldsymbol{q}, \boldsymbol{q_0}, \dot{\boldsymbol{q}}) + \boldsymbol{G}(\boldsymbol{q})$. $\boldsymbol{\tau}$ is is the joint torque vector for the system, consisting of $\left[\boldsymbol{\tau}_p^T, \boldsymbol{\tau}_a^T\right]^T$, which are the passive joint torques and the actuator effort torques for the driven joints; the matrix $\boldsymbol{M}(\boldsymbol{q})$ is the inertia matrix for the system; and $\boldsymbol{H}(\boldsymbol{q}, \dot{\boldsymbol{q}})$ is the collection of Coriolis factors and centrifugal terms for the manipulator. $\boldsymbol{N}(\boldsymbol{q}, \boldsymbol{q_0}, \dot{\boldsymbol{q}})$ is the general viscoelastic term and $\boldsymbol{G}(\boldsymbol{q})$ is the gravity term. The state vector, $\boldsymbol{q} = \left[\boldsymbol{q}_p^T \;\; \boldsymbol{q}_a^T\right]^T$, contains state information for all of the joints in the system, containing $\boldsymbol{q}_p = [x_{mobile}, y_{mobile}, \theta_1]^T$ and $\boldsymbol{q}_a = [\theta_2 \;\; \theta_3]^T$. Note that the horizontal position of the undercarriage center, x_{mobile} is a variable, but assumed to be fixed when the system is in motion, therefore is not included in the dynamic equation.

5.2.3 Rigid Body Jacobian

In many practical implementations, manipulators are considered completely rigid and resonant frequencies are significantly higher than the control bandwidth. One of the simplest class of manipulator end-point feedback controllers can be obtained from its Jacobian matrix, derived only from kinematic information, in the form of its inverse or transpose, where dynamic close-loop stability is guaranteed for rigid systems.

Oscillations due to its flexible undercarriage may be within the control bandwidth and thus introduce oscillatory or unstable responses. As a practical approach, one may still want to use the rigid-body assumption and examine stability and performance limits when applied to a flexible-base manipulator without increasing the complexity of feedback control. Figure 5.3 (bottom) illustrates this concept where the base deformation is strategically neglected. The rigid body Jacobian, $\boldsymbol{J}_v$, can be found by only considering the motion of the two links in the manipulator chain $\boldsymbol{J}_v = \begin{bmatrix} -l_2 S_{12} - l_3 S_{123} & -l_3 S_{123} \\ l_2 C_{12} + l_3 C_{123} & l_3 C_{123} \end{bmatrix}$.

5.2.4 Feedback Control

A method to control the manipulator is to specify joint velocities: $\dot{\boldsymbol{q}}_{ad} = \boldsymbol{J}_v(\boldsymbol{q}_a)^{-1}\boldsymbol{f}(\boldsymbol{O}_{ed}, \boldsymbol{O}_e)$, with control structure detailed in Figure 5.4. Obtained $\dot{\boldsymbol{q}}_{ad}$ is directly converted into joint torques, $\boldsymbol{\tau}_a = \begin{bmatrix} 1 & 0 \\ & \\ 0 & 1 \end{bmatrix} \dot{\boldsymbol{q}}_{ad}$.

5.2.5 Manipulator System Modeling

Local asymptotic stability of the nonlinear system can be evaluated by a linearized model about a particular desired end-point position. Recall that the undercarriage oscillation is passive therefore $\boldsymbol{\tau}_p = 0$ and a linearized model can be written as: $\begin{bmatrix} 0 & \boldsymbol{\tau}_a^T \end{bmatrix}^T = \boldsymbol{M}\ddot{\boldsymbol{q}} + \boldsymbol{D}\dot{\boldsymbol{q}} + \boldsymbol{K}(\boldsymbol{q} - \boldsymbol{q}_d)$ is obtained, where $\boldsymbol{q}_d$ is the desired joint states for the manipulator;

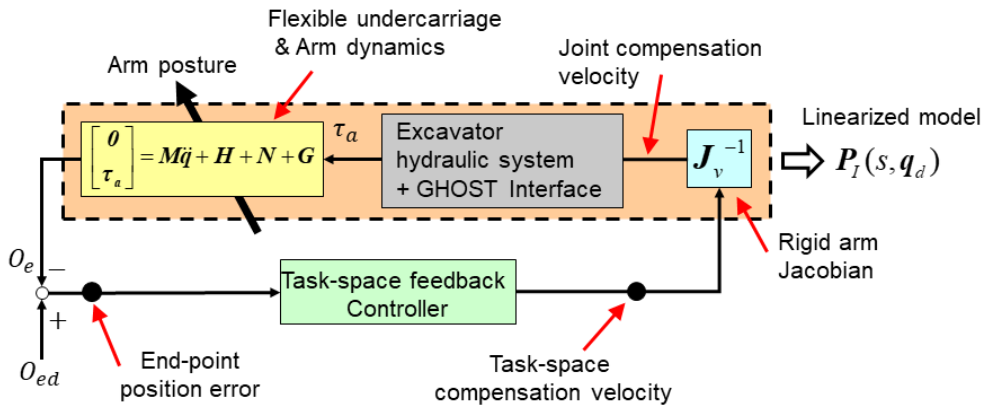

Figure 5.4: Block diagrams illustrating the control structure for Jacobian Inverse control

$\boldsymbol{D}$ is the viscosity matrix of the system; and $\boldsymbol{K}$ is the stiffness matrix for the system. Defining $\boldsymbol{x} = \left[\dot{\boldsymbol{q}}^T, (\boldsymbol{q} - \boldsymbol{q}_d)^T\right]^T$ and $\boldsymbol{y} = \boldsymbol{r}(\boldsymbol{q}) - \boldsymbol{r}(\boldsymbol{q}_d)$, a two-input two-output state-space representation in the work coordinate system is obtained as: $\dot{\boldsymbol{x}} = \boldsymbol{A}\boldsymbol{x} + \boldsymbol{B}\boldsymbol{f}$ and $\boldsymbol{y} = \boldsymbol{C}\boldsymbol{x}$, with

$$\boldsymbol{A} = \begin{bmatrix} -\boldsymbol{M}^{-1}\boldsymbol{D} & -\boldsymbol{M}^{-1}\boldsymbol{K} \\ \boldsymbol{I} & \boldsymbol{O} \end{bmatrix} \tag{5.2}$$

$$\boldsymbol{B}_I = \begin{bmatrix} \boldsymbol{M}^{-1} \begin{bmatrix} \boldsymbol{O}^{3\times 2} \\ \boldsymbol{I}^{2\times 2} \end{bmatrix} \\ \boldsymbol{O}^{(3+2)\times 2} \end{bmatrix} \boldsymbol{J}_v^{-1} \tag{5.3}$$

$$\boldsymbol{C} = \begin{bmatrix} \boldsymbol{O} & \boldsymbol{J} \end{bmatrix} \tag{5.4}$$

where $\boldsymbol{J} = \partial \boldsymbol{r}/\partial \boldsymbol{q}^T \in \Re^{2\times(3+2)}$, $\boldsymbol{J}_v = \partial \boldsymbol{r}_v/\partial \boldsymbol{q}_a^T \in \Re^{2\times 2}$ are Jacobian matrices. The plant for this system can be realized from the state-space form as:

$$\boldsymbol{P}_I(s, \boldsymbol{q}_d) = \boldsymbol{C}(s\boldsymbol{I} - \boldsymbol{A})^{-1}\boldsymbol{B}_I \tag{5.5}$$

Note that $\boldsymbol{P}_I$ is the linearized plant dynamics seen from the task-space controller when the Jacobian Inverse control is applied.

5.2.6 Modal Analysis

By using modal analysis, $\boldsymbol{P}(s)$ can be represented as a linear combination of n rigid modes and m vibration modes. Matrix $\boldsymbol{A}$ has in total $2(n+m)$ poles where $2n$ of these poles are zero, corresponding to the rigid modes, and $2m$ conjugate complex poles correspond to the vibration modes.

Let $\lambda_0 = 0$,λ_i ,$\bar{\lambda}_i$ $(i = 1 \cdots, m)$ be $2m+1$ distinct eigenvalues of $\boldsymbol{A}$. λ_0 , λ_i and $\bar{\lambda}_i$ correspond to the rigid modes and the ith vibration modes respectively. $\boldsymbol{U}$ and $\boldsymbol{V} = \boldsymbol{U}^{-1}$ are defined from the modal decomposition/ Jordan normal form of A and is the orthogonality transformation between the state matrix and its modal-space. Note that $\boldsymbol{v}^*$ denotes the conjugate transpose (or Hermitian transpose) of $\boldsymbol{v}$. By applying $\boldsymbol{U}, \boldsymbol{V}$ to $\boldsymbol{A}$ with $n = 2$ rigid body modes and $m = 3$ flexible modes, [81], of $\boldsymbol{P}(s)$ for Jacobian inverse control is given below.

$$\begin{aligned}
\boldsymbol{P}_I(s) &= \sum_{j=1}^{n} \frac{\boldsymbol{C}\boldsymbol{u}_{2j-1}\boldsymbol{v}_{2j}^*\boldsymbol{B_I}}{s^2} \\
&\quad + \sum_{i=1}^{m} \left(\frac{\boldsymbol{C}\boldsymbol{u}_{2(n+i)-1}\boldsymbol{v}_{2(n+i)-1}^*\boldsymbol{B_I}}{s-\lambda_i} + \frac{\boldsymbol{C}\boldsymbol{u}_{2(n+i)}\boldsymbol{v}_{2(n+i)}^*\boldsymbol{B_I}}{s-\bar{\lambda}_i} \right) \qquad (5.6) \\
&= \frac{1}{s^2}\boldsymbol{R}_{0,I} + \sum_{i=1}^{m} \frac{1}{s^2 + 2\zeta_i\hat{\omega}_i s + \hat{\omega}_i^2}\boldsymbol{R}_i \\
\boldsymbol{R}_{0,I} &= \sum_{j=1}^{n} \boldsymbol{C}\boldsymbol{u}_{2j-1}\boldsymbol{v}_{2j}^*\boldsymbol{B_I} = \boldsymbol{J}_v^T \hat{\boldsymbol{M}}^{-1} \boldsymbol{J}_v^{-1} \qquad (5.7) \\
\boldsymbol{R}_i &= -2\mathrm{Re}\left(\bar{\lambda}_i(\boldsymbol{C}\boldsymbol{u}_{2(n+i)-1})(\boldsymbol{v}_{2(n+i)-1}^*\boldsymbol{B_I})\right),\ i \geq 1 \qquad (5.8)
\end{aligned}$$

In (Equation 5.6)-(Equation 5.8), $\boldsymbol{R}_0$ corresponds to the rigid body modes where $\boldsymbol{R}_0$ is a positive definite matrix. $\hat{\boldsymbol{M}} = [M_{kl}] \in \Re^{n\times n}(m+1 \leq k, l \leq m+n)$ is a partial matrix of $\boldsymbol{M}$. $\boldsymbol{R}_i$ is called a residue matrix. Note that $\boldsymbol{R}_i$ is positive-semi-definite and rank$(\boldsymbol{R}_i) = 1$ at most from (Equation 5.8). In addition, $\hat{\omega}_i = |\lambda_i|$, $\zeta_i = -\mathrm{Re}(\lambda_i)/\,|\lambda_i|$ is obtained where ζ_i and $\hat{\omega}_i$ represent the damping coefficient and the natural frequency, respectively. It is

also of note that the outer product $(\boldsymbol{u}_{2j-1}\boldsymbol{v}_{2j}^{*})$ yields the spectral projector of the $2j^{th}$ mode of the system, and is equivalent in concept to $\boldsymbol{\Omega}_i$ of the previous chapter.

5.3 Robustness Metrics

Link parameters of the excavator are found in Table 5.1 and are derived from the geometry of a 3D model assuming the material is isotropic steel. The viscoelastic parameters are chosen so that the modal frequency range is similar to that of the data shown in Figure 5.2.

Table 5.1: Dynamic parameters

Name	Value	Unit	Name	Value	Unit
l_b	0.541	m	l_{gb}	0.563	m
l_1	1.918	m	l_{g1}	1.067	m
l_2	1.097	m	l_{g2}	0.613	m
m_b	5291.5	kg	I_b	1020.7	kgm^2
m_1	766.6	kg	I_1	214.9	kgm^2
m_2	458.2	kg	I_2	93.6	kgm^2
k_x	$4x10^7$	Nm^{-1}	b_x	50	Nsm^{-1}
k_y	$4x10^7$	Nm^{-1}	b_y	50	Nsm^{-1}
k_θ	$1.112x10^6$	Nm^{-1}	b_θ	25	Nsm^{-1}
θ_{1d}	1.2451 rad				

Robustness analysis is performed to determine the configurations of a manipulator that are robust to undercarriage oscillation and, therefore, are stable. Numerically calculating the NCF robustness (section 3.4) of the plant across its workspace it becomes possible to characterize the robustness of the plant, ε_{max}, at all of its achievable postures.

Similarly, the manipulator workspace can be described through its passivity-based robustness using the w_i passivity indices from section 3.3. These measures indicate the distance from the current robot configuration to a robust arm configuration (RAC) [54]. The

linearized system in this configuration is positive real, and therefore passive [54]. The regions where each of these flexible modes is in-phase is shown in Figure 5.5. MIMO systems such as the one considered in this chapter have no guarantee for a total in-phase design [82, 83]. However, being that the third mode is at a much higher natural frequency, it can be seen in Figure 5.5(d) that for the manipulator described by the parameters in Table 5.1 that the manipulator workspace has many configurations where its first two flexible modes are in-phase with one another.

As shown in Figure 5.6, NCF stability is calculated across the workspace where higher

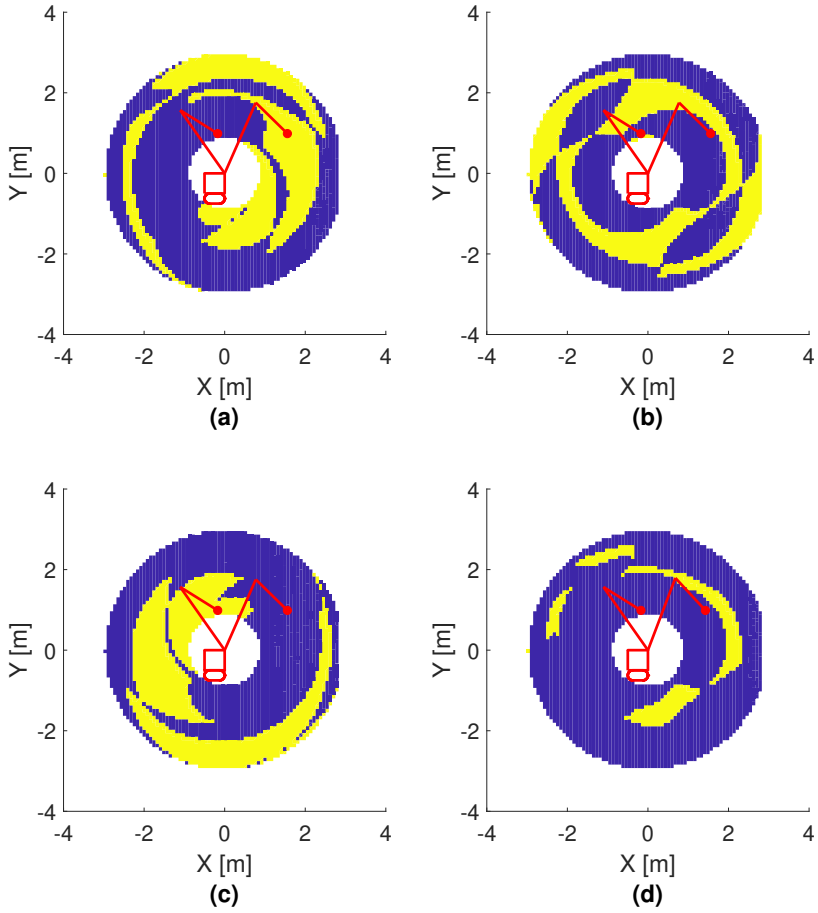

Figure 5.5: In-phase regions (shown in yellow) for a manipulator workspace under Jacobian inverse control. (a) First, (b) second, (c) third flexible mode, and (d) the total in-phase region for the first and second modes; the union of (a) and (b). Manipulator configurations shown in red are found in Table 5.2. Coordinates are in the rigid-manipulator workspace.

values are indicative of more robust configurations (with Figure 5.7 showing regions of

high NCF robustness). While the robustness is dependent on both the plant model and the servo gain used in the analysis, there is a clear difference in performance between locations with high and low stability margin. Similarly, in Figure 5.8, a surface can be generated for each flexible mode in the system using the modal passivity index, with approximate RAC postures shown in Figure 5.9. It can be seen that features in the modal-based robustness surfaces appear in the coprime factorization surfaces. The relationship between the comprime factor-based robustness metric and the modal stability indices can be seen in the GAP metric [84] between the rigid body excavator system and the total flexible system, shown in Figure 5.10 for both Jacobian transpose and inverse control. The disparity in scale between the two control architectures can likely be attributed to the difference in strucutre of the Jacobian inverse control compared to transpose control and the gain limitations inverse control has to maintain stability [85] (also, although likely to a lesser extent, transpose control has an amount of guaranteed asymptotic stability [86]). However, the regions of low robustness correspond to high GAP in the workspace, making these robust postures ones where the flexible system "close" to the desired rigid one. Utilizing the relationship between the two robustness metrics established in the previous chapter it becomes possible to only use the modal analysis w_i metric to perform posture optimization [87].

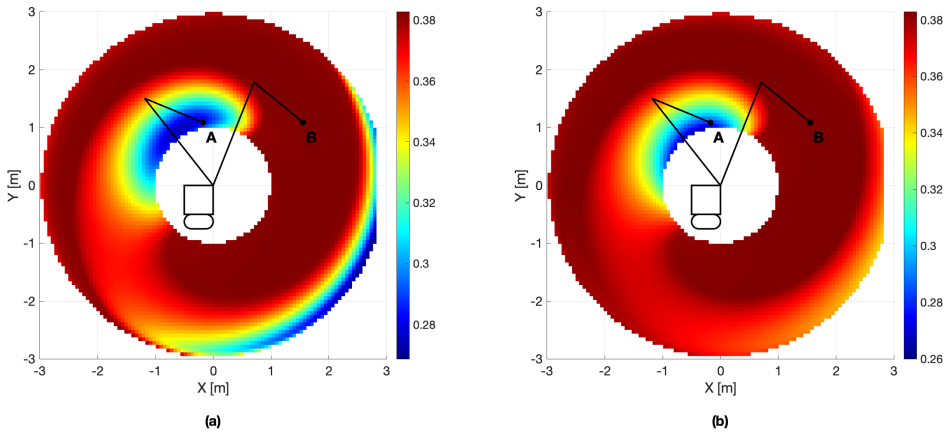

Figure 5.6: ε_{max} calculated across the manipulator workspace.(a) is the curve associated with Jacobian transpose control and (b) is associated with Jacobian inverse control.

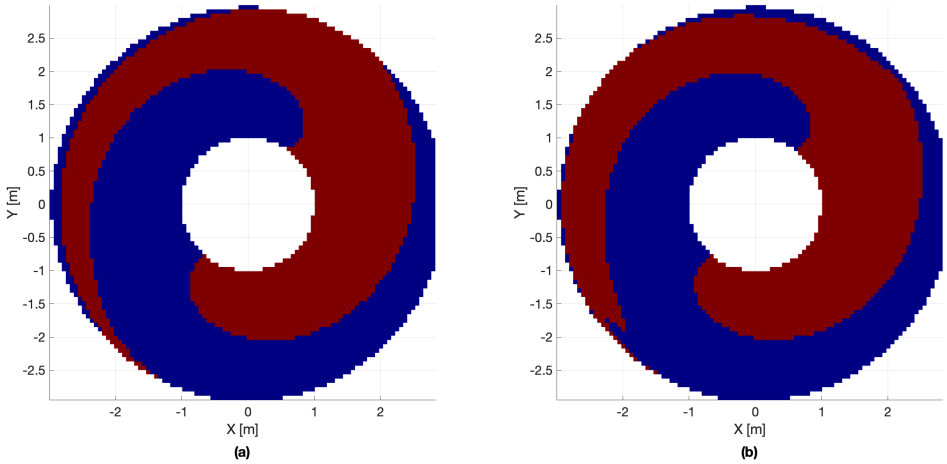

Figure 5.7: Regions of high NCF robustness for Jacobian (a) transpose and (b) inverse control, shown in red.

5.4 Manipulator Configuration Optimization

Due to the manipulator being on a mobile base, there is a planar redundancy between the x axis position in world frame and the x axis position of the manipulator end-point in the manipulator's workspace. It is then possible to reconfigure the position of the manipulator's mobile base in order to put the manipulator's goal position in a position with a higher stability margin. The variation of stability margin with end-point position for a given y_{ed} is shown in Figure 5.11. Mathematically, this redundancy can be represented as

$$\tilde{\boldsymbol{q}}_{\boldsymbol{d}} = \underset{\boldsymbol{q}_{\boldsymbol{d}} \in \{\Theta : y_e = y_d\}}{\operatorname{argmax}} V(\boldsymbol{q}_{\boldsymbol{d}}) \tag{5.9}$$

where Θ is a set of arm configurations that realizes $\boldsymbol{O}_{ed}$ [54]. Here, the objective function $V(\boldsymbol{q}_{\boldsymbol{d}})$ is defined as

$$V(\boldsymbol{q}_{\boldsymbol{d}}) = \sum_{i=1}^{m} \alpha_i w_i(\boldsymbol{q}_{\boldsymbol{d}}) \tag{5.10}$$

To maximize computational ease (as compared to the calculations for the NCF stability margin), the use of w_1 will be used to optimize the base position under Jacobian nullspace control for redundant manipulators. From Figure 5.11 it can be seen that the

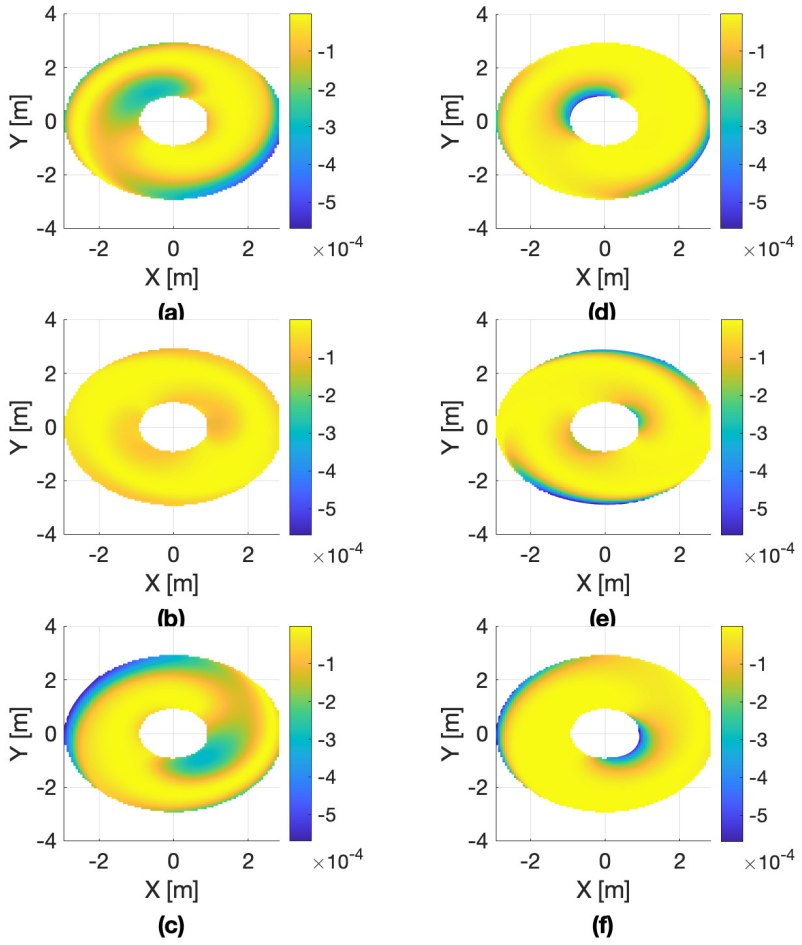

Figure 5.8: w_i Robustness metric for the flexible modes of the manipulator system under Jacobian (a)-(c) transpose control and (d)-(f) inverse control. Each row corresponds to successive flexible modes. With mean natural frequencies of: 3.0872 Hz, 13.1392 Hz, and 22.4394 Hz respectively.

curves for ε_{max} and w_1 follow the same general shape, so there is not a clear performance increase between using one or the other. The update law for the redundant base parameters $[x_{mobile,d},\ \theta_{2d},\ \theta_{3d}]$ is:

$$\Delta \boldsymbol{q_d} = \boldsymbol{S}(\boldsymbol{I} - \boldsymbol{J}_B^{+}\boldsymbol{J}_B)\boldsymbol{k}_\xi \boldsymbol{\xi},\ \boldsymbol{S} = \left[\begin{array}{c|c} 1 & \boldsymbol{O}_{3x2} \\ \hline \boldsymbol{O}_{4x1} & \boldsymbol{I}_{2x2} \end{array}\right] \tag{5.11}$$

$\boldsymbol{k}_\xi$ is a positive gain matrix used to selectively damp the augmentation of the nullspace for each coordinate, and $\boldsymbol{\xi}$ is the gradient of the objective function, (Equation 5.10). The Jacobian used to map the redundant parameters to the manipulator end-point, $\boldsymbol{J}_B$, is defined as $\boldsymbol{J}_B \in \Re^{2x3} = \begin{bmatrix} 1 & \\ 0 & \boldsymbol{J}_v \end{bmatrix}$.

While the use of a weighted sum of flexible modes will violate the concavity of the objective function, binary weights can be used to select which of the flexible modes is being optimized against. In the case of the proposed system in this study, the first flexible mode is at a very low frequency, so we will use the following α parameters: $\alpha_1 = 1$, $\alpha_2 = 0$, $\alpha_3 = 0$ for $m = 3$ and $n = 2$. For the given objective function its gradient $\boldsymbol{\xi}$ is given by:

$$\xi = \frac{\partial}{\partial \boldsymbol{q_B}^T}\left(\sum_{i=1}^{m}\alpha_i w_i(\boldsymbol{q})\right) = \left[\frac{\partial}{\partial x_{mobile}}\left(\sum_{i=1}^{m}\alpha_i w_i(\boldsymbol{q})\right)\frac{\partial}{\partial \theta_2}\left(\sum_{i=1}^{m}\alpha_i w_i(\boldsymbol{q})\right)\right. \\ \left.\frac{\partial}{\partial \theta_3}\left(\sum_{i=1}^{m}\alpha_i w_i(\boldsymbol{q})\right)\right]^T \tag{5.12}$$

Executing the gradient of the objective function for a particular parameter $q_l \in \boldsymbol{Sq_d}$, yields:

$$\frac{\partial V(\boldsymbol{q})}{\partial q_l} = \sum_{i=1}^{m}\alpha_i \frac{\partial w_i(\boldsymbol{q})}{\partial q_l} \tag{5.13}$$

with

$$\frac{\partial w_i(\boldsymbol{q})}{\partial q_l} = \sum_{a=1}^{n}\left(\sum_{b=1}^{n}\left(\frac{\partial[\boldsymbol{R}_i + \boldsymbol{R}_i^T]_{ab}}{\partial q_l}\nu_b\right)\nu_a\right) \tag{5.14}$$

where $[\boldsymbol{R}_i + \boldsymbol{R}_i^T]_{ab}$ is the element in the a^{th} row and b^{th} column of the matrix given by $\boldsymbol{R}_i + \boldsymbol{R}_i^T$, and $\nu \in \Re^n$ is the eigenvector associated with $\lambda_{min}(\boldsymbol{R}_i + \boldsymbol{R_i}^T)$. Derivation of this gradient is shown in Appendix C.

5.5 Results

Simulations of the nonlinear manipulator system were conducted in Matlab (Mathworks) using an RK4 numerical integrator. The integration step of the MATLAB simulation was selected to be 0.005 second (i.e., 200 Hz), which is significantly higher than the resonant frequencies of the flexible system and its closed-loop control bandwidth. Changing the end-point position in the workspace, one can improve the stability of the end-point control of the manipulator system as illustrated in Figure 5.11. Applying both ε_{max} and w_i stability margins to two discrete points in the manipulator workspace, shown in Table Table 5.2, we can see an improvement in convergence and when going from a position of low robustness to high robustness. The results of optimizing the mobile base position with Jacobian inverse control are shown in Figure 5.12 using two discrete positions, shown in Table 5.2 based on their w_1, shown in Figure 5.8(d). It can be seen that there is better performance for the optimized position that has a higher robustness.

Table 5.2: Controller Stability Margins Optimization Positions. *See Figure 5.5 for workspace end-point positions and postures

$\boldsymbol{Posture}$	$\boldsymbol{A}$	$\boldsymbol{B}$
$\boldsymbol{x_{desired}}$	0.00m (inertial) -0.1733m (workspace)*	0.00m (inertial) 1.32687m (workspace)*
$\boldsymbol{y_{desired}}$	1.60m (inertial) 1.0870m (workspace)*	1.60m (inertial) 1.0870m (workspace)*
$\boldsymbol{x_{mobile}}$	0.00m	-1.50m
$\boldsymbol{\varepsilon_{max}}$	0.2869	0.3826
$\boldsymbol{w_1}$	-0.2969×10^{-3}	-0.0209×10^{-4}
$\boldsymbol{w_2}$	-0.0308×10^{-3}	-0.0683×10^{-4}
$\boldsymbol{w_3}$	-0.001×10^{-3}	-0.3105×10^{-4}

The same phenomena can be seen when moving the manipulator mobile base to change the position of the end-point in the workspace without changing its position in the inertial coordinate space. This can be seen in Figure 5.13. Moving the manipulator base according to the trajectory generated through nullspace augmentation, shown in Figure 5.13, does

excite some base oscillation and end-point error. However, by moving the system from a configuration of low robustness to one of high robustness, manipulator stability can be achieved.

5.6 Contribution of Work

The use of the coprime factorization-based stability margin and modal decomposition based stability margin allows for end-point feedback control robust to model variation in base oscillations. When employed alongside the redundancy introduced by the mobile base of the excavator, configuration optimization is able to position the end-point of the excavator at the desired target position while still utilizing a robust arm configuration without explicitly including the undercarriage flexibility in the controller. As long as the configuration for the manipulator is chosen to have a high stability margin against induced undercarriage oscillation, the feedback system is stable and does not excite unstable vibration modes.

This work has been published in the inaugural issue of *Letters in Dynamic System Control*, [88].

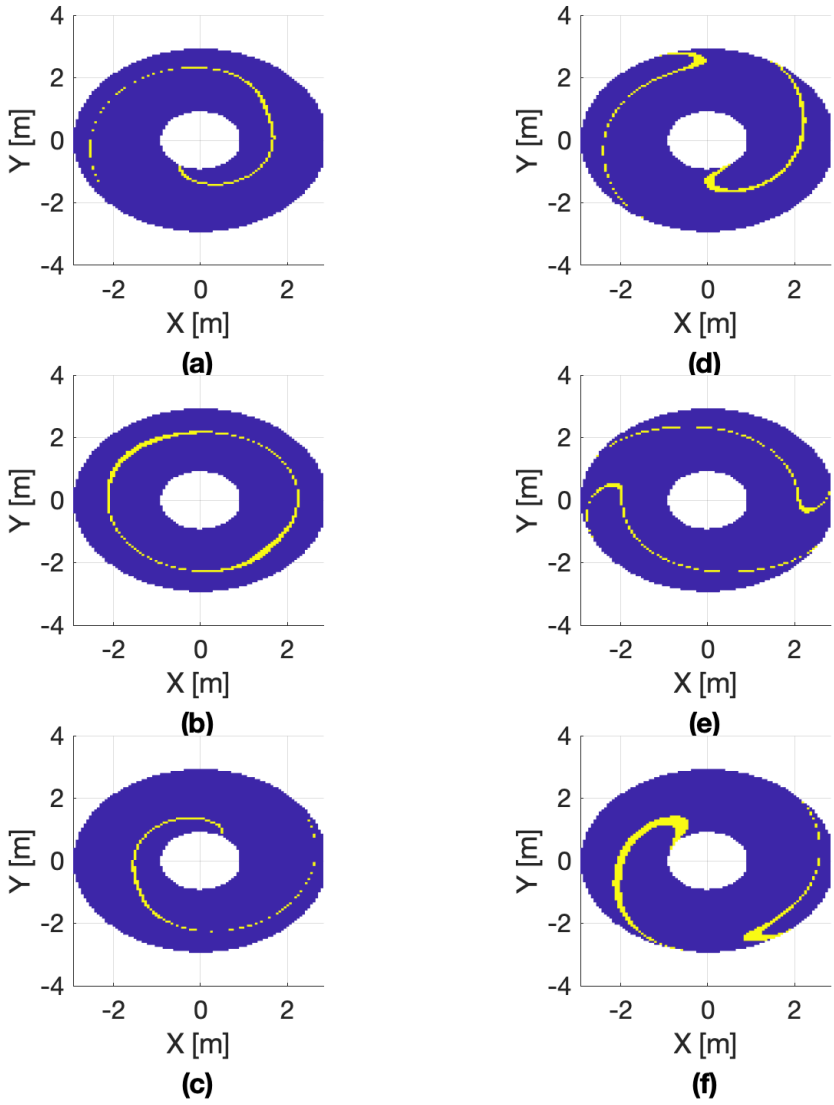

Figure 5.9: Approximate robust arm configuration curves curves for the flexible modes of the manipulator system under Jacobian (a)-(c) transpose control and (d)-(f) inverse control. Each row corresponds to successive flexible modes. With mean natural frequencies of: 3.0872 Hz, 13.1392 Hz, and 22.4394 Hz respectively.

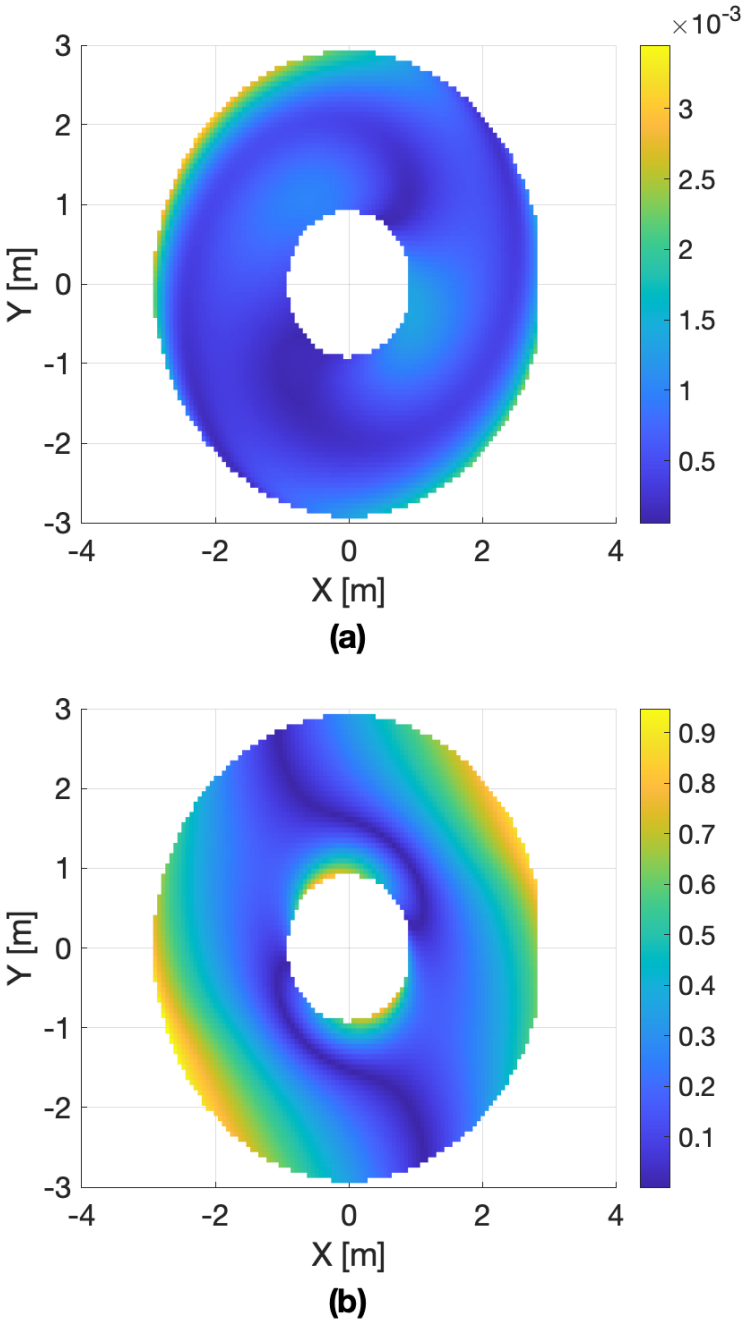

Figure 5.10: GAP metric for Jacobian (a) transpose and (b) inverse control.

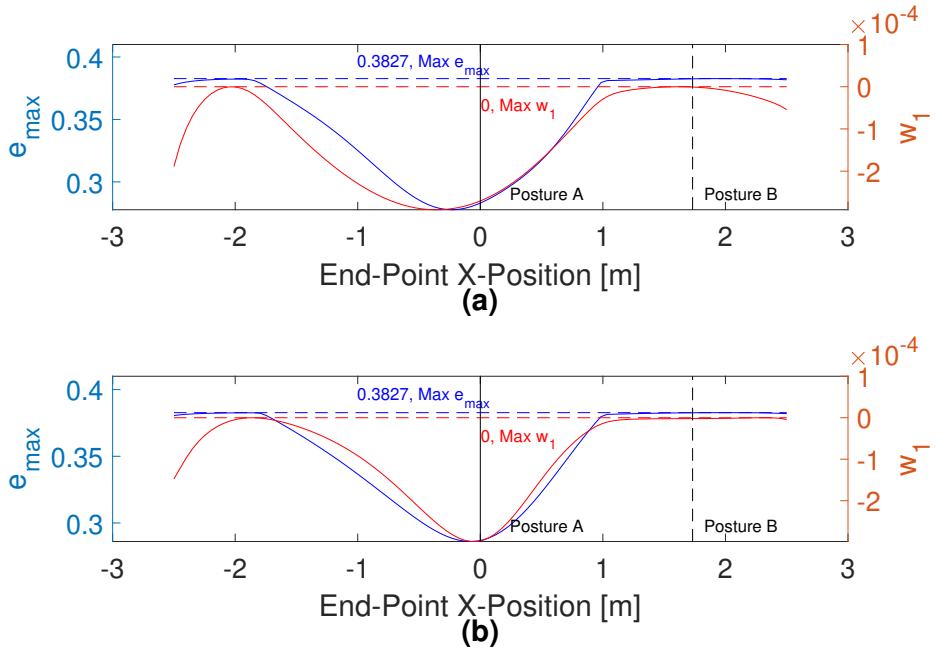

Figure 5.11: Optimization curves for (a) Jacobian transpose control and (b) Jacobian inverse control along the desired y_d. Due to the presence of the second and third flexible modes, ε_{max} is always less than its maximum of 0.3827.

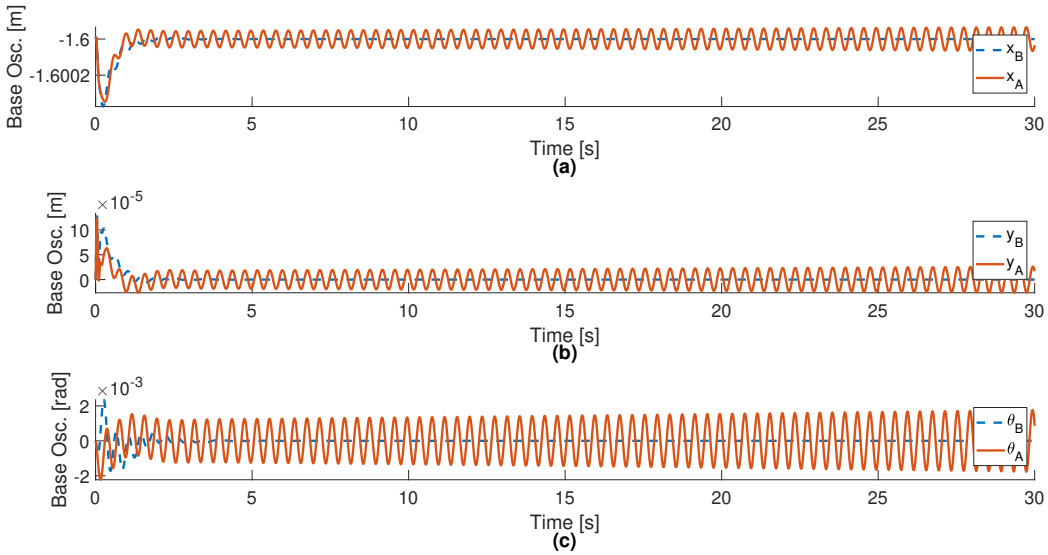

Figure 5.12: Base oscillations for the chosen optimization positions using Jacobian inverse controller. (a) is x axis oscillation, (b) is y axis oscillation, and (c) is the angular oscillation of the manipulator base.

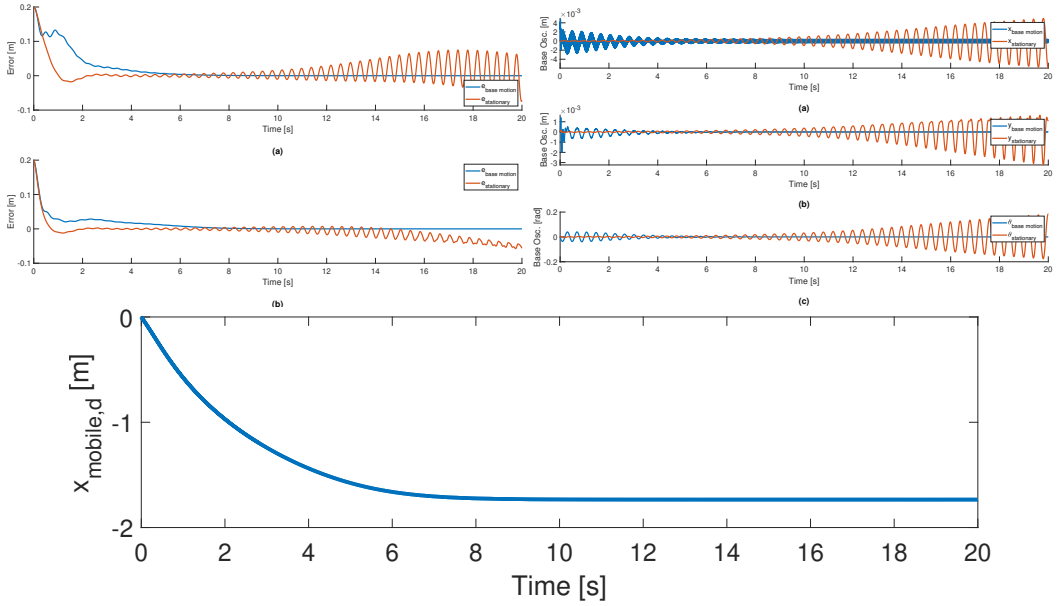

Figure 5.13: End-point position error (center) and base oscillation (right) using Jacobian inverse controller with and without base position adjustment. Base position adjustment changing from posture A to posture B using the base trajectory shown left during end-point positioning (shown in blue). Without base position adjustment (shown in red) end-point positioning around Posture A.

CHAPTER 6

DEGENERATE MOBILE ROBOT INVERSE KINEMATICS

6.1 Problem Description

The class of robots addressed in this chapter are termed degenerate by the definition in section 2.3, but are also required to be over-actuated. This requirement comes from the need for the system to be instantaneously configurable and from the power transmission ability four driven wheels provides. The foundational difference between the use of these degenerate structures and the classical offset structures that the lack of longitudinal offset in the wheel structure prevents the decoupling of the two components of the system angular velocity - the reorientation of the wheel with respect to the world frame and with the robot frame - at the velocity level. Further, the redundancy in zero-caster offset wheel structure prevents the independent selection of the angle of the wheel with respect to the world frame and the robot. This is evident in a loss of rank in the wheel Jacobians and suggests a change of state variables and use of a nonlinear solution.

Using an analytical inverse kinematics solution, the singularities from the matrix-inversion solution are avoided and the joint states for the wheel structures are solvable. While robots of similar structure have been designed, [89], considerations in their methodologies focus on generating specific modes of operation rather than solving the inverse kinematics for the system.

6.2 Mobile Robot Platform Model and Kinematics

6.2.1 Psuedo-Omnidirectional, Nonholonomic Drive Mobile Robot Platform

The development of a reconfigurable pseudo-omnidirectional mobile platform is presented in this section Figure 6.1. Omnidirectionality and reconfigurability are enabled through a

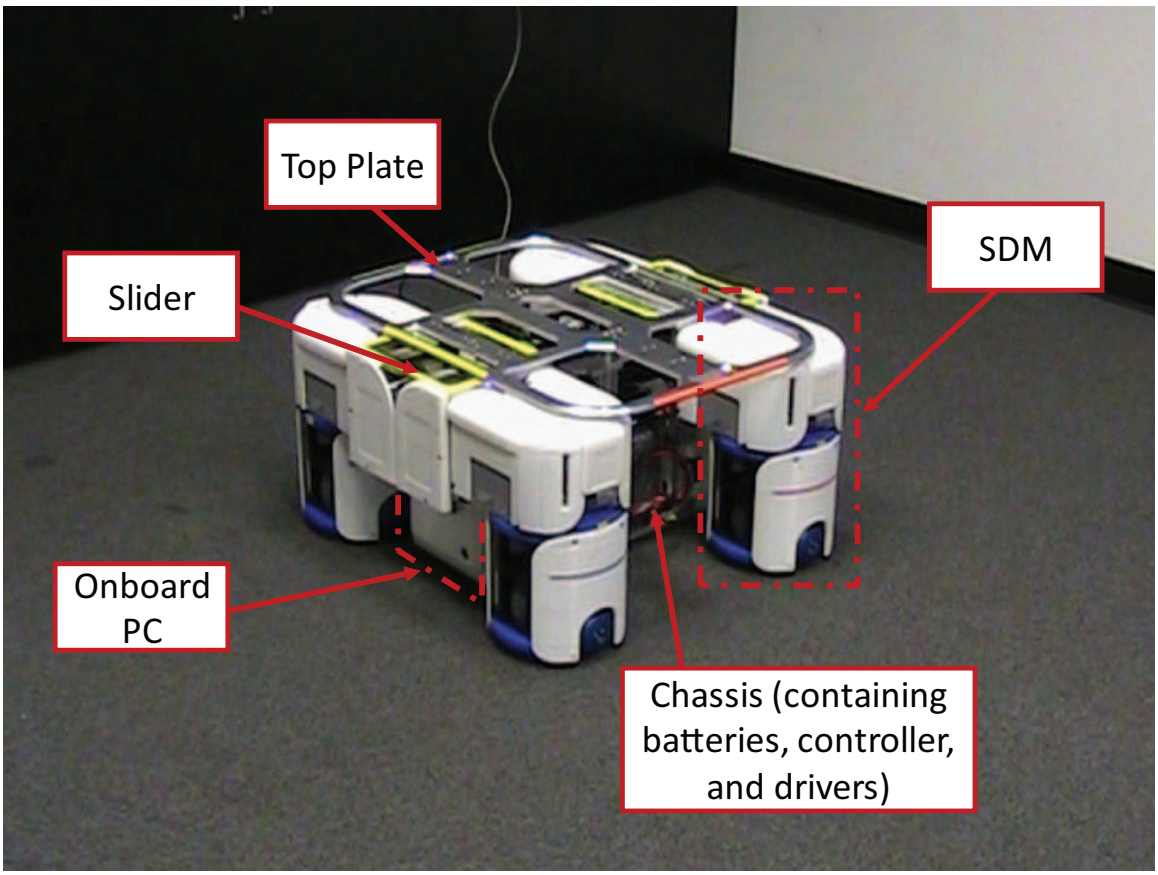

Figure 6.1: The reconfigurable pseudo-omnidirectional mobile platform

transforming chassis and four uniquely developed synchronous drive modules (SDM).

The development of the reconfigurable chassis with lateral transformation highlights the necessity of wheel structures that can reorient themselves without needing to move in the plane (unlike in traditional caster wheels [90]). If one considers thse use of wheel structures that do not satisfy this property, it is clear that as the chassis attempts to expand, there is a chance for the system to bind mechanically and damage the chassis.

The robot platform consists of four wheel modules that behave, dynamically, similar to a centered-orientable wheels mounted on two sliding mechanisms that change the footprint of the robot. These wheel structures are controlled locally with proportional-integrating controllers to orient and set the speed of the wheel structure with one "primary" and one "secondary" wheel like in [91]. Simplifying the interface of these wheel modules is possible thorugh treating them like centered, orientable conventional wheels.

Synchronous Driving Module (SDM)

The developed SDM is categorized as a centered orientable concentional wheel. The *zero* caster offset property makes the robot pseudo-omnidirectional, requiring reorientation of the wheel structures The choice of the SDM design and the key components are shown in Figure 6.2. Also, a simplified illustration of the SDM mechanism is presented in Figure 6.3.

The size of an SDM is 208.8 mm $\times$ 248.5 mm $\times$ 380.7 mm. Each SDM consists of the upper static part and the lower rotary part. The mounting bracket in the upper back of the module is fixed to the main chassis so the upper SDM doesn't move relative to the platform. The lower SDM is free to rotate about the central vertical axis (i.e., zero caster offset). Instead of a single motor generating torque about the rotating axis as widely seen in the conventional wheel design, this particular SDM uses two synchronous and independently driven wheels driving in the opposite directions at the same speed (one driving forward, the other driving backward) to perform the steering. Because the ground condition is indoors and known, to minimize stress on the shafts of the harmonic drive, the center wheel is passive and takes the majority of the load without possibility of slip from the drive wheels. As a result of introducing this mechanism, the SDM can re-orient itself without inducing any moment to the chassis, which minimizes disturbances to the positioning accuracy of the chassis with the conventional powered caster wheels.

Each active side wheels is independently driven by a servo motor (Sanyo Denki, Japan, R2GA04008DCS01, rated output: 80W) with an embedded incremental encoder. A load cell located at the top of the SDM is integrated to measure vertical loading force to the wheels. The Elmo Gold DC Whistle (Elmo, Israel) supporting EtherCAT communication protocol is selected as the motor driver.

SDM Validation

Tracking a square-corner path without orienting the chassis is shown in Figure 6.4. Re-orientation of a wheel is achieved by rotating two active wheels to the opposite direction

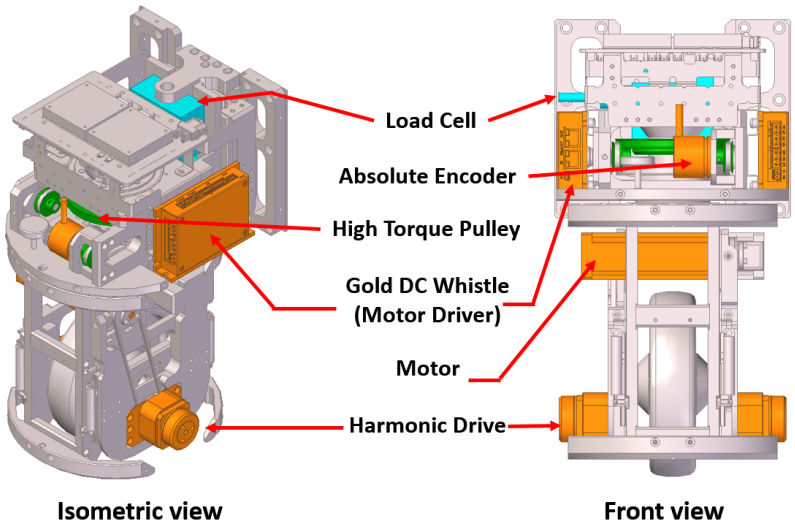

Figure 6.2: Rendering of Synchronous Drive Module, labeled, with drive wheels removed to highlight harmonic drive mechanism.

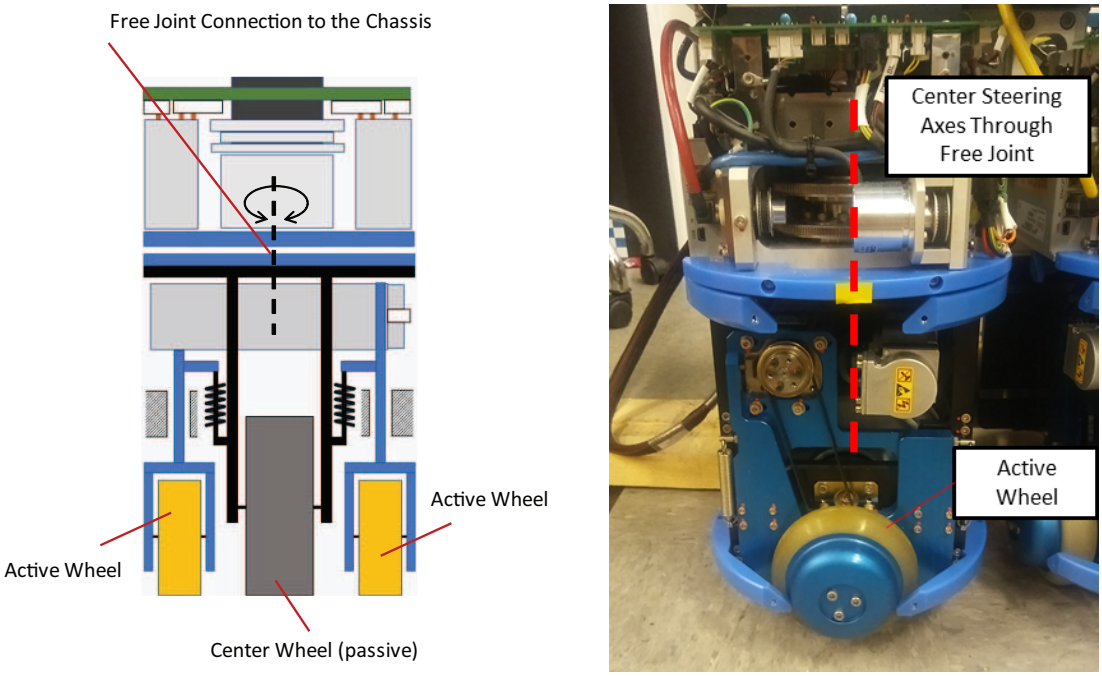

Figure 6.3: SDM Schematic and Profile (Rotated by 90° counterclockwise)

to each other, inducing vertical rotation in the lower part of the wheel module. Since the vertical rotational axis is a free joint, no torque associated with the reorientation of the wheel is transmitted, minimizing unwanted disturbance to the chassis. While similar wheel mechanisms have been developed [52], they employ a driven steering axis that could exert a reaction torque on the chassis. While the proposed mechanism cannot revolve indefinitely due to limitations of the absolute encoder, intelligent choice of system trajectory could minimize the need to reorient the whole mechanism.

An Optitrack motion capture system was used to capture the world-frame motion of the robot. Figure 6.5 shows linear velocities, angular velocity, and one of the wheels steering angle, corresponding to each of the scenes shown in Figure 6.4. In Scene 3, the robot chassis was stationary, and the wheels were re-oriented (the steering angle was programmed to come back to the neutral angle first, and then move to a desired angle). During the wheel reorientation, the chassis merely created angular velocity of 0.0012 ± 0.0015 rad/s. Even for the entire square-corner path tracking, from Scene 1 to 5, the angular velocity was -0.0025 ± 0.0662 rad/s. In other words, the chassis's orientation was kept almost unchanged throughout the motion.

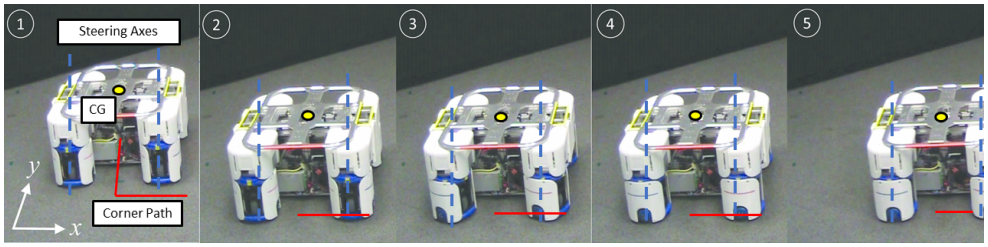

Figure 6.4: Reorientation of wheels and tracking of a square corner test trajectory

Reconfigurable Chassis

The movable parts of the chassis are two aluminum slider assemblies sliding on the linear guides on the top of the main chassis as in Figure 6.6. Each slider is independently driven by a servo motor (Sanyo Denki, Japan, R2GA04008DCP00E01, rated output: 80W) along a ball screw with a screw nut bracket attached to the slider. This sliding mechanism works

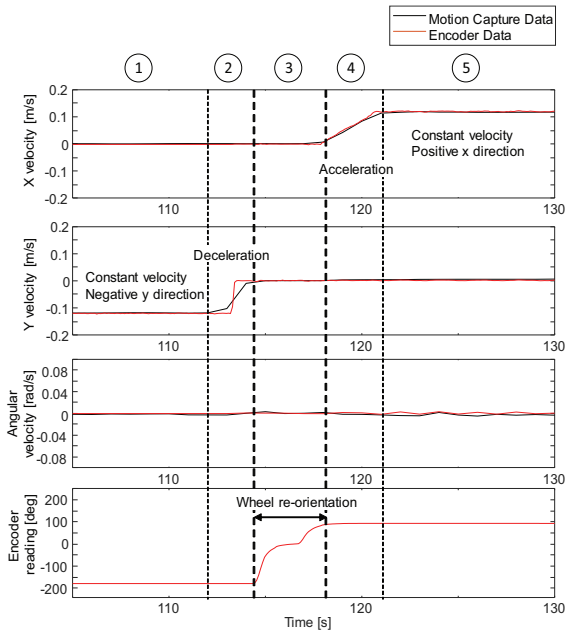

Figure 6.5: Wheel orientation and captured chassis motion when tracking a square corner path. Scene numbers correspond to Figure 6.4.

as a prismatic joint to allow 1 degree of freedom (DOF) motion, illustrated in Figure 6.7. Each slider has a maximum displacement of 100 mm which adds up to a total of 200 mm lateral reconfiguration range.

The SDMs are mounted on the sliders as shown in Figure 6.9. Each slider holds two SDMs on each side with one facing front and the other facing rear. Four SDMs are labeled as Module 1 through Module 4, and two sliders are Slider 1 and Slider 2. To perform the chassis reconfiguration when the mobile platform is stationary, Module 1 and Module 2 are aligned towards the left, whereas Module 3 and Module 4 are aligned towards right. Each SDM pair drives at the same velocity as the attached slider to complete the extension or retraction motion. To reconfigure the chassis while the mobile platform is in motion, the slider velocity is added to the current SDM motion using the described kinematic formulation.

Table 6.1: Robot Geometry Parameters

Variable	Value	Description
r	50 [mm]	Wheel Radius
l	240 [mm]	Robot Half-Width
a	270.5 [mm]	Robot Half-Length

Mobile Platform Structure

The mobile platform has four driving modules as the majority of conventional mobile robots do. A cubic frame designed as the main chassis of the platform where four SDMs can be attached to consists of one base plate, six aluminum extrusions, and one top plate. System hardware such as motion controller, onboard PC, power distribution panel, and lead-acid batteries are compactly organized within the open space of the chassis. As shown in Figure 6.6 and Figure 6.8, two linear guides are installed on the top plate to enable the chassis reconfiguration.

The size of the main chassis is 264 mm $\times$ 483 mm $\times$ 387.5 mm. The overall platform length (747 mm) and the minimum width (483 mm) are determined by the size and placement of four batteries, whereas the height (406.5 mm) is determined by the height of the SDM.

The goal of introducing reconfigurability to the robot platform was to give the operator or control system the ability to center the robot's contact pad with the ground under the load of the robot. This would minimize the tipping risk involved in moving large loads about a confined warehouse space. The choice to include two sets of expansion mechanisms over a single one was made to increase the available degrees of freedom to compensate a misplaced load.

6.2.2 Reduced Modeled Mobile Robot Platform

In the previous section, the SDM wheel modules were described to function similarly to the centered, orientable conventional wheels. For this one can treat the platform as having the

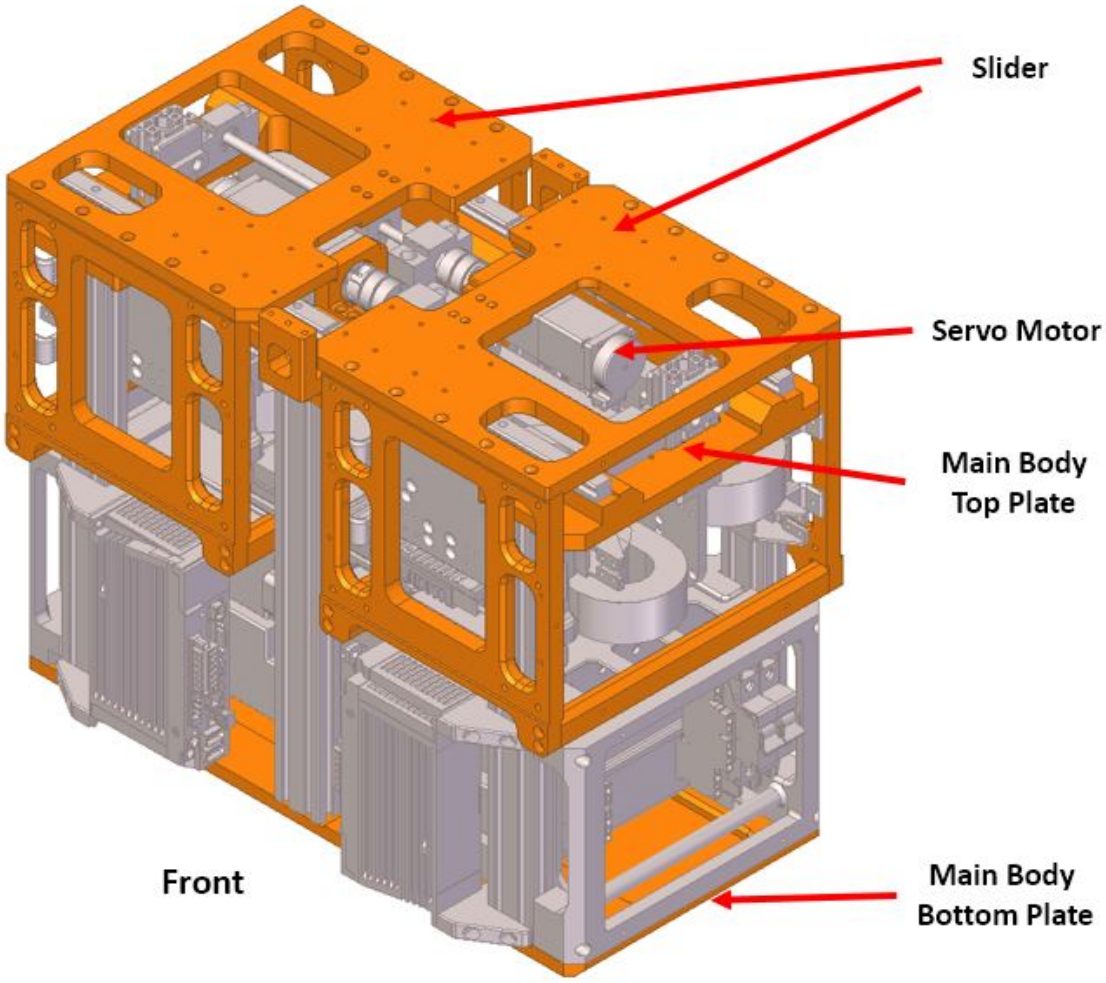

Figure 6.6: Movable Sliders on the main chassis

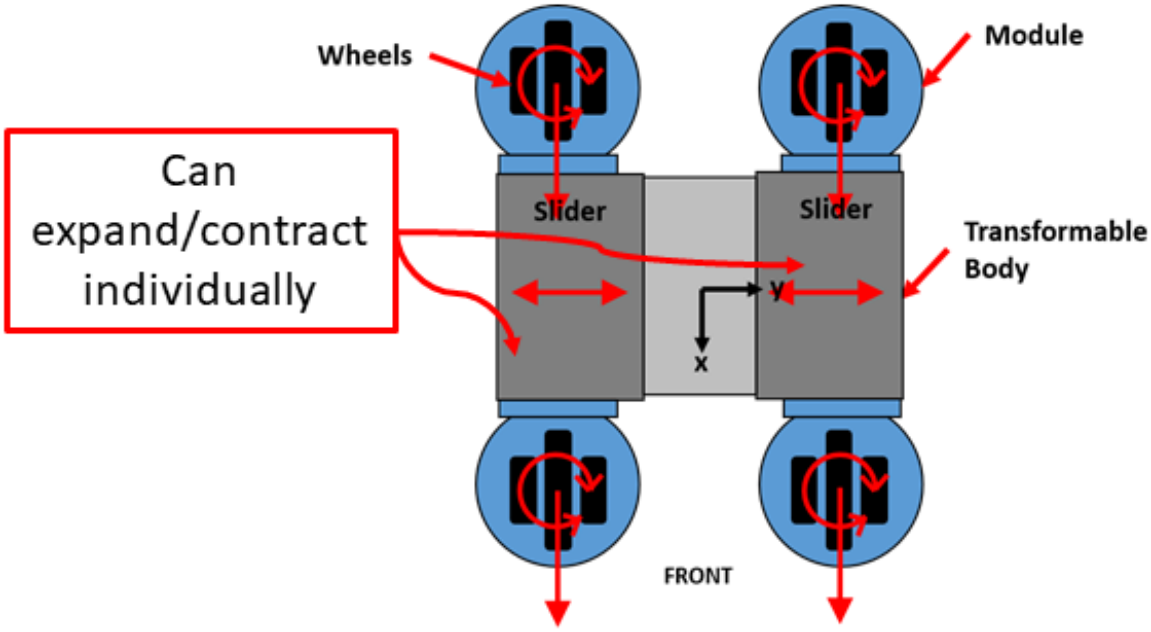

Figure 6.7: General function of robot expansion mechanism

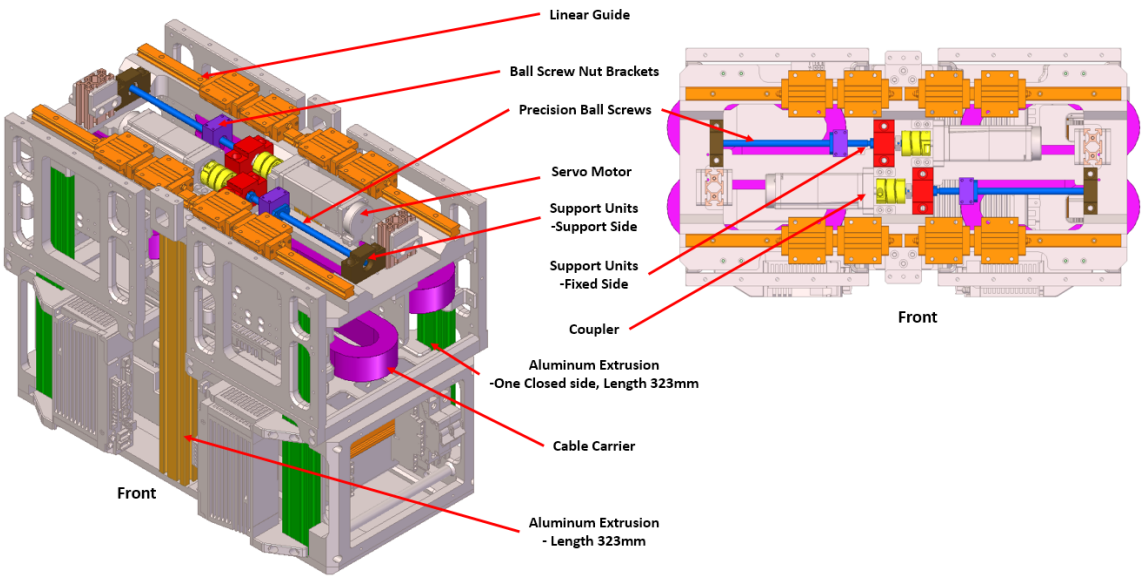

Figure 6.8: Components on the main chassis

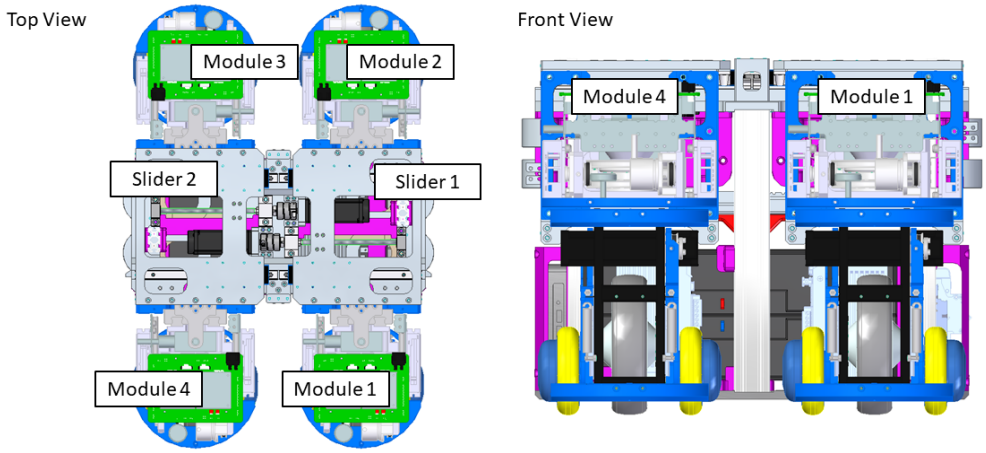

Figure 6.9: Rendering detailing the enumeration of both the drive modules and the sliding mechanisms

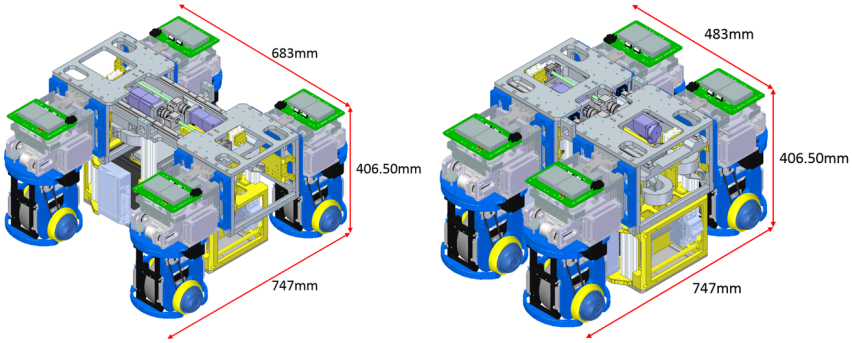

Figure 6.10: Mobile platform dimension: extended and retracted

same model as the platofrm shown in Figure 6.11. The orientation of the robot in inertial coordinates ($\{W\}$ frame) is denoted by ψ and is the angle of the robot-i vector ($\{RB\}$ frame) to the inertial-I vector. This example is a consideration of the robot designed in Section II under no transformation and reducing each SDM to a centered, orientable wheel.

Each of the robot's wheels is centered on a corner of the robot's chassis, shown in Figure 6.11. The chassis is $2l$ wide and $2a$ long, with wheels of radius r that are offset from the steering interface by h distance. Each wheel has a local, body-fixed coordinate system that is coplanar with the wheel plane which is offset from the robot coordinate system by φ_i radians, denoted by the $\hat{W}_m$ prefix, where m is the wheel number.

The proposed analysis will be done so as to derive a set of equations to generate goal

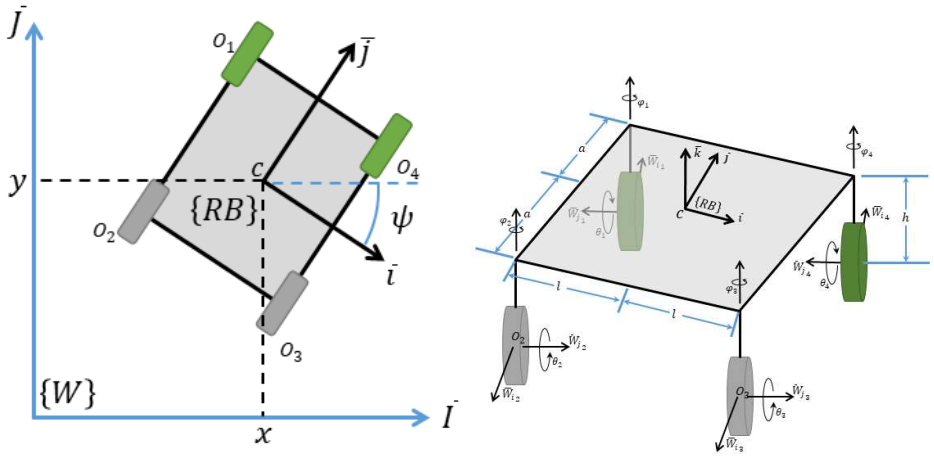

Figure 6.11: The inertial reference frame and body-fixed coordinate frames for the mobile robot

values for the steering angle and drive speed of each wheel as functions of the robot's desired planar velocity, $\mathbf{v_c} = \begin{bmatrix} v_x & v_y & \omega \end{bmatrix}^T$ so that they may be used as set points for local controllers at the wheel-level that ensures the positioning and speed of each wheel. Incidentally, this creates a lack of control over the rate of change of the steering direction of each wheel, so even if the desired parameters from the inverse kinematic method could be successfully retrieved using inverse Jacobian methods, post-processing would need to be conducted in order to retrieve the data that is useful to the control of this robot.

6.2.3 Kinematic Analysis

Kinematic analysis is conducted on a degenerate mobile robot shown in Figure 6.11. On this robot the controllable parameters are the steering angles of its wheels, denoted by φ_i, and the rotational speed of its wheels, $\dot{\theta}_i$. The goal of this analysis is to derive closed form solutions to each of these values so that they may be used in conjunction with a low-level servo controller that will be orienting and setting the wheel speeds.

Following the method employed by Yi, the analysis will begin using open chain kinematics to relate the wheel mechanism kinematics to the robot-center velocity [39]. The point of contact between the wheel and the ground can be instantaneously modeled as a higher-order pair that allows for rotation and translation with a single link between the steering axis of the wheel to the robot-center [37].

Each of the wheels makes an open kinematic chain with the center of the robot, therefore the system can be treated as a set of four parallel manipulators. The result is a set of vector equations for each of the wheel structures (omitted for space). ω_i, the robot angular velocity, can be defined as the sum of the rate of change of the steering angle, φ_i and the rate of change of the angle of the wheel with respect to the inertial frame. η_i, therefore $\omega_i = \dot{\eta}_i + \dot{\varphi}_i$. The result of substituting this for each wheel into the parallel-chain velocity equations is a set of matrix equations that represent the relationships between the kinematic variables in the system:

$$\begin{bmatrix} v_x \\ v_y \\ \omega \end{bmatrix} = \begin{bmatrix} -r\sin\varphi_1 & a & a \\ r\cos\varphi_1 & l & l \\ 0 & 1 & 1 \end{bmatrix} \begin{bmatrix} \dot{\theta}_1 \\ \dot{\eta}_1 \\ \dot{\varphi}_1 \end{bmatrix} \tag{6.1}$$

$$\begin{bmatrix} v_x \\ v_y \\ \omega \end{bmatrix} = \begin{bmatrix} r\sin\varphi_2 & -a & -a \\ -r\cos\varphi_2 & l & l \\ 0 & 1 & 1 \end{bmatrix} \begin{bmatrix} \dot{\theta}_2 \\ \dot{\eta}_2 \\ \dot{\varphi}_2 \end{bmatrix} \tag{6.2}$$

$$\begin{bmatrix} v_x \\ v_y \\ \omega \end{bmatrix} = \begin{bmatrix} r\sin\varphi_3 & -a & -a \\ -r\cos\varphi_3 & -l & -l \\ 0 & 1 & 1 \end{bmatrix} \begin{bmatrix} \dot{\theta}_3 \\ \dot{\eta}_3 \\ \dot{\varphi}_3 \end{bmatrix} \tag{6.3}$$

$$\begin{bmatrix} v_x \\ v_y \\ \omega \end{bmatrix} = \begin{bmatrix} -r\sin\varphi_4 & a & a \\ r\cos\varphi_4 & -l & -l \\ 0 & 1 & 1 \end{bmatrix} \begin{bmatrix} \dot{\theta}_4 \\ \dot{\eta}_4 \\ \dot{\varphi}_4 \end{bmatrix} \tag{6.4}$$

It can be seen that the matrix equations (Equation 6.1) through (Equation 6.4) should map the wheel parameters – each mechanism's rates of rotation about its axes – to the desired robot velocity. Normally at this point Yi suggests the selection of actuated joints as independent variables so that the forward kinematics of the system can be derived for the remaining joint variables [39]. While this is a useful method for deriving the kinematics of a redundantly actuated mobile robot, the controllable joint parameters are the steering angle, φ_i, and the drive speed of each wheel mechanism, $\dot{\theta}_i$, so developing a relationship for the steering rates of the wheel mechanisms would not serve the necessary purpose. For this, the kinematic relationships themselves can individually be examined in order to derive the working relationship between the robot velocity and the parameters of interest because the wheel mechanisms are decoupled from one another. This is to say that the selection of variables φ_1 and $\dot{\theta}_1$ have little impact on the selection of the variables φ_2 and $\dot{\theta}_2$ insofar as each pair of variables satisfies the system of equations represented in (Equation 6.1) and (Equation 6.2).

In order to find a pair of variables to satisfy any of the matrix equations, the system needs to be corrected so as to properly parallel the actuated mechanics of the robotic system. The rate at which the wheel mechanism rotates within the inertial frame can be described as the sum of two rates of rotation $\dot{\eta}_i$ and $\dot{\varphi}_i$. The former, being the angular displacement between the drive direction of the wheel mechanism and the inertial coordinate frame, is non-actuated due to zero-length caster-offset in the mechanism and exists as a

consequence of the robot's planar motion within the inertial reference frame. For this, it becomes impossible to decouple the steering rate of the wheel mechanism, $\dot{\varphi}_i$, from $\dot{\eta}_i$; this is further evident in the redundant columns in the kinematic relationships shown in (Equation 6.1) through (Equation 6.4). Furthermore, the rotation rate of the wheel relative to the robot-frame, $\dot{\varphi}_i$, is unrelated to the rotational speed of the robot based on the kinematic relations above, therefore the redundant columns in these relations can be removed and the systems can be reshaped as shown in (Equation 6.5) - (Equation 6.8) [47]. This allows for the inverse kinematics relationship between the robot twist and the desired wheel mechanism parameters to be actualized.

$$\begin{bmatrix} v_x \\ v_y \end{bmatrix} = \begin{bmatrix} -r\sin\varphi_1 & a \\ r\cos\varphi_1 & l \end{bmatrix} \begin{bmatrix} \dot{\theta}_1 \\ \omega \end{bmatrix} \tag{6.5}$$

$$\begin{bmatrix} v_x \\ v_y \end{bmatrix} = \begin{bmatrix} r\sin\varphi_2 & -a \\ -r\cos\varphi_2 & l \end{bmatrix} \begin{bmatrix} \dot{\theta}_2 \\ \omega \end{bmatrix} \tag{6.6}$$

$$\begin{bmatrix} v_x \\ v_y \end{bmatrix} = \begin{bmatrix} r\sin\varphi_3 & -a \\ -r\cos\varphi_3 & -l \end{bmatrix} \begin{bmatrix} \dot{\theta}_3 \\ \omega \end{bmatrix} \tag{6.7}$$

$$\begin{bmatrix} v_x \\ v_y \end{bmatrix} = \begin{bmatrix} -r\sin\varphi_4 & a \\ r\cos\varphi_4 & -l \end{bmatrix} \begin{bmatrix} \dot{\theta}_4 \\ \omega \end{bmatrix} \tag{6.8}$$

6.2.4 Inverse Kinematics Solutions

Proceeding with the linear equations shown in (Equation 6.5)-(Equation 6.8), singularities (where the determinate of the matrix portion equals to 0) can be identified at configurations that place the drive axes of diagonal pairs of wheels colinear and passing through the geometric center of the robot platform. Mechanically, this would occur when $\varphi_1 =$

$\varphi_3 = \arctan\left(-\frac{a}{l}\right)$ or when $\varphi_2 = \varphi_4 = \arctan\left(\frac{a}{l}\right)$, shown for φ_1 in Figure 6.12. This couples the planar x-axis and y-axis velocities of the wheel mechanisms, locking the robot into traveling along those diagonals in the case of only one pair in singularity, or force the robot into rotation in the case of both pairs in singularity. At any of these angles the inverse-matrix based solution for inverse kinematics does not exist. Note that the preceding

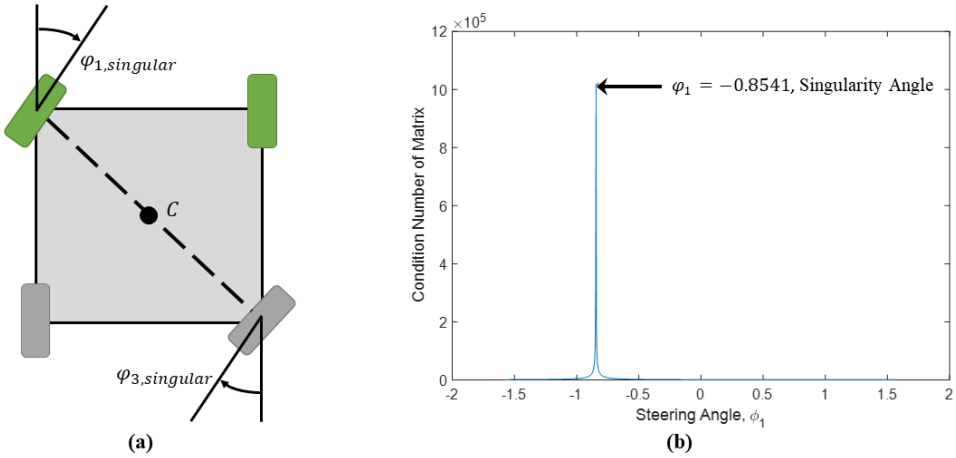

Figure 6.12: Singularity condition for $\varphi_1 = \varphi_3 = \arctan\left(\frac{-a}{l}\right)$. (a) is graphical representation of singularity, and (b) shows the condition number of the matrix (Equation 6.5). As the singularity angle is approached, the condition number peaks.

formulation is well-known in mobile robotics literature. The joint-variable solution of this system requires consideration.

Upon re-arranging the systems as pairs of linear equations, they are solved pair-wise to obtain the inverse kinematics solution:

$$\dot{\theta}_1 = \pm\frac{1}{r}\sqrt{(v_x - a\omega)^2 + (v_y - l\omega)^2} \tag{6.9}$$

$$\dot{\theta}_2 = \pm\frac{1}{r}\sqrt{(v_x + a\omega)^2 + (v_y - l\omega)^2} \tag{6.10}$$

$$\dot{\theta}_3 = \pm\frac{1}{r}\sqrt{(v_x + a\omega)^2 + (v_y + l\omega)^2} \tag{6.11}$$

$$\dot{\theta}_4 = \pm\frac{1}{r}\sqrt{(v_x - a\omega)^2 + (v_y + l\omega)^2} \tag{6.12}$$

$$\varphi_1 = \mp 2\arctan\frac{\pm 2(l\omega - v_y) + 2\sqrt{(v_x - a\omega)^2 + (v_y - l\omega)^2}}{2(v_x - a\omega)} \tag{6.13}$$

$$\varphi_2 = \mp 2 \arctan \frac{\pm 2(l\omega - v_y) + 2\sqrt{(v_x + a\omega)^2 + (v_y - l\omega)^2}}{2(v_x + a\omega)} \tag{6.14}$$

$$\varphi_3 = 2 \arctan \frac{2(v_y - l\omega) \mp 2\sqrt{(v_x + a\omega)^2 + (v_y + l\omega)^2}}{2(v_x + a\omega)} \tag{6.15}$$

$$\varphi_4 = 2 \arctan \frac{2(v_y - l\omega) \mp 2\sqrt{(v_x + a\omega)^2 + (v_y - l\omega)^2}}{2(v_x - a\omega)} \tag{6.16}$$

These direct solutions joint-variable solutions allow for the resolution of joint parameters along the singularity angles from the inverse-matrix based solution. For velocity commands that would require the platform be put in a singularity state, the direct solutions will resolve to correct sets of joint angles. Note that while this formulation is successful in identifying the inverse kinematics of a degenerate mobile robot system, it only works for quasi-static system descriptions. Consideration of second-order dynamics will require more consideration into the transit of each of the desired system states.

6.3 Results

6.3.1 Qualitative Evaluation of Solutions

As detailed above in (Equation 6.9) to (Equation 6.16), when the 2×2 systems are solved with an equation solver, the result is sets of two bifurcating equations that represent the positive and negative solutions of the steering angle and the drive speed of the centered, orientable wheel.

In left of Figure 6.13(a,c) it is seen that as the desired velocity tends along each of the XY-axes the function saturates at 0 radians or $-\frac{\pi}{2}$ radians to align the wheel with the j and i axes of the robot body respectively.This surface has the range of 0 to $-\frac{\pi}{2}$ radians (Z-axis top-to-bottom), which is acceptable given the orientation of the wheel reference frame, this would orient the wheel into the first quadrant of the robot coordinate frame and allow the wheel to properly align itself with the desired translational velocity. The "negative" solution, shown on right of Figure 6.13, shows the same geometry, but the scale goes from

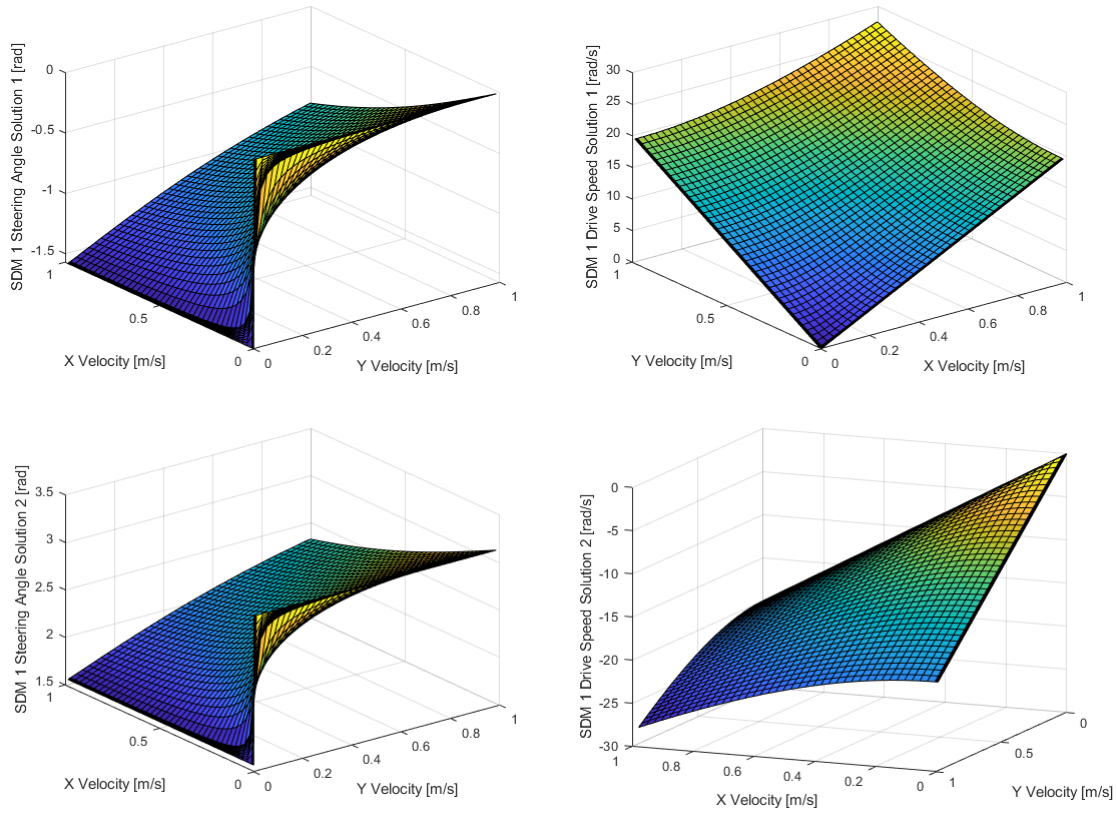

Figure 6.13: Steering Angle and Drive-Speed Solutions for Wheel 1 of Example Robot under Strict Translation (Left: postive pair of solutions, Right:negative pair of solutions) ($\omega = 0$)

$\frac{\pi}{2}$ to π radians (Z-axis bottom-to-top). This suggests that for the same input velocity the output steering angle would be in the third quadrant along the same reference angle as the positive solution, but on the opposite angle (a π radian offset).

In Figure 6.13(b,d) it can be seen that for a strict robot translation the surface forms an upward facing infinite cone that describes the required rate of rotation of wheel 1 for a given translation command (a monotonically increasing, concave surface). When considering this as a possible drive-speed solution to match with a steering angle solution, it can be seen that each solution for the steering angle is not compatible with each solution for the wheel drive-speed. For example, the solution shown in Figure 6.13(d) would not generate the goal velocity if used with the positive steering angle solution shown in Figure 6.13(a). For this it becomes essential that the solutions are matched properly pairwise in order to provide an

accurate motion solution.

6.3.2 Quantitative Results of Experimentation

Data was collected with the Optitrack system at about 16 samples a second. Encoder data was sampled at the speed of the robot's control loop, about 10Hz. The path followed by the robot is shown in Figure 6.14; this was processed to get the robot's planar twist by means of numerical differentiation. The robot planar velocity was reconstructed using the collected encoder data.

From the provided figure, the planar mobility of the robot can be qualitatively assessed.

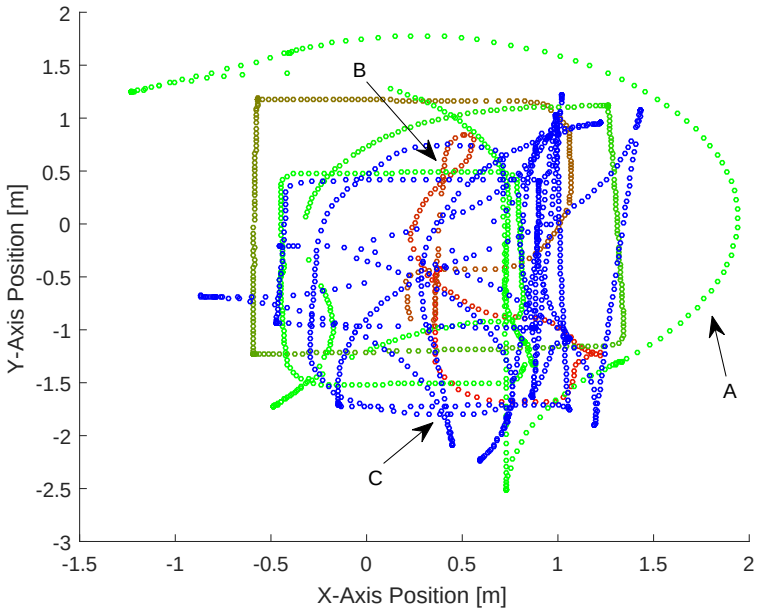

Figure 6.14: Motion Capture of Robot Motion Under Control, Color Varies with Time as Red $\rightarrow$ Green $\rightarrow$ Blue

Point "A" on Figure 6.14 refers to the ICR-based motion the robot is capable of. As the robot moves about the curve its orientation remains consistent with its direction of travel. This is similar to the point of interest "C" where the cusp shown in blue is the result of the robot changing directions and ICR locations instantaneously, illustrating the ability for this robot to change directions of travel without turning around and without utilizing

omnidirectional motion. While the robot can change its direction of travel instantaneously using the ICR-based motions, the point of interest "B" shows a closed loop made by the robot when it was traveling while maintaining orientation toward the negative-Y direction.

The resulting velocity and angular velocity profiles are shown in Figure 6.15. While

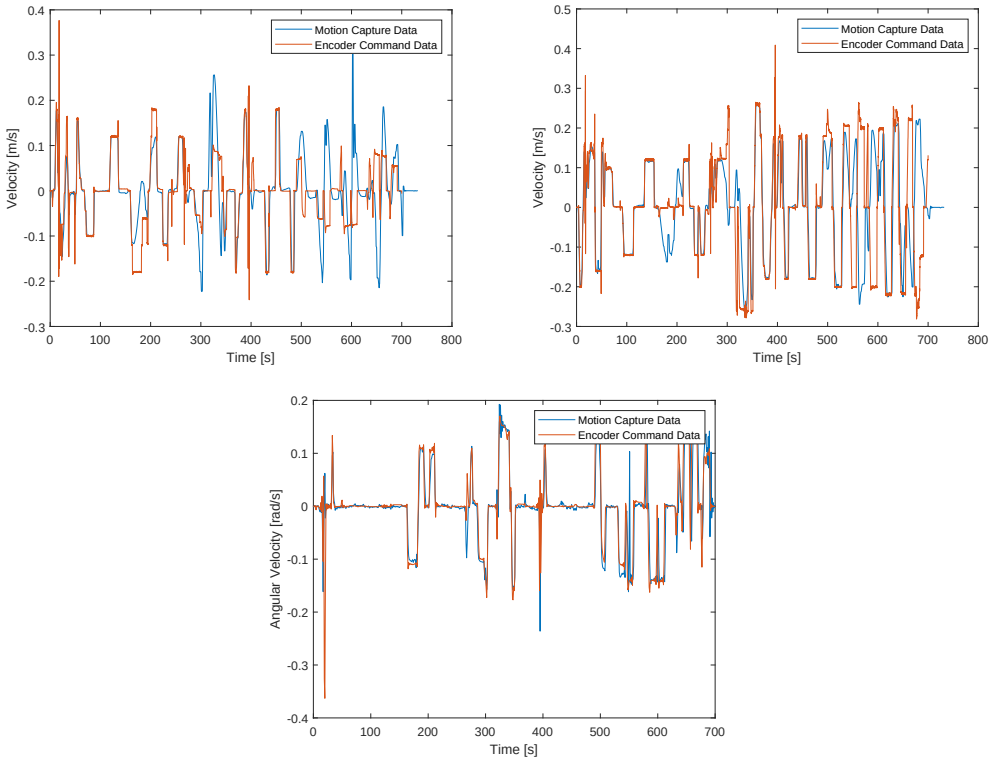

Figure 6.15: X, Y, and Angular Velocities of the Robot and the Motion Capture

numerical comparisons would yield inconclusive results, it is important to note that the waveforms have similar patterns, but are shifted in time from one another, which can be attributed to mismatches in purported data rate wduring reconstruction. In order to provide some metric for the likeness of the two data sets, a cross correlation was computed for each pair of velocity profiles. The zero-lag correlation value for each set of signals is a metric of the similarity between the reconstructed velocity command from the encoder data matches the commanded velocity. The presence of non-zero lag magnitude on the cross-correlation plots implies that there is a difference in sampling time between the two signals.

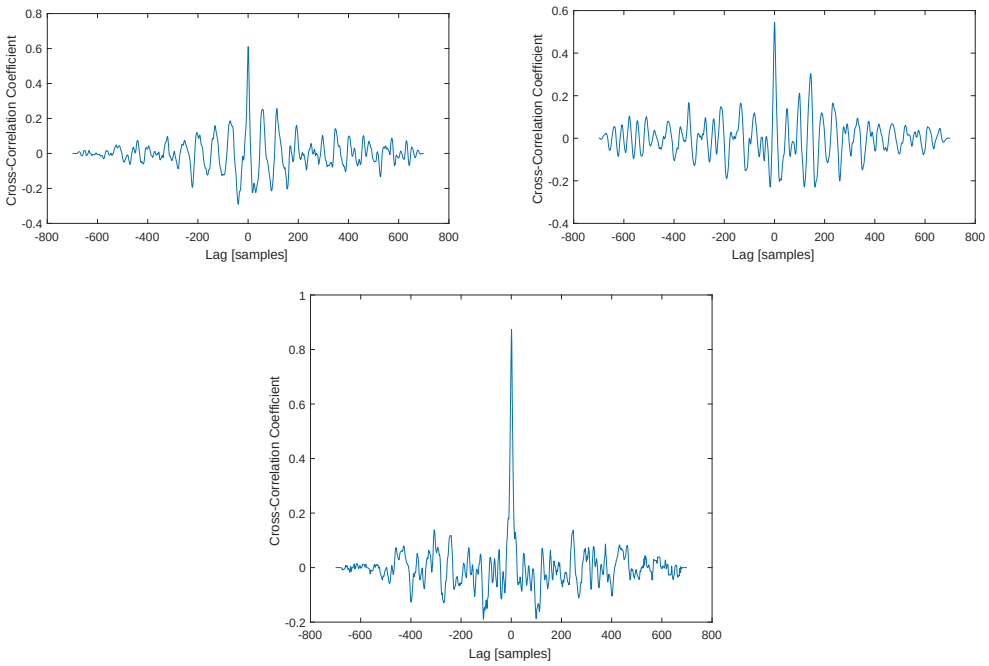

Figure 6.16: Cross Correlation of the Commanded and Captured X,Y, and Angular Velocities, sampled at about 10 Hz.

From the cross-correlation in angular velocity shown in right Figure 6.16, it can be seen that there is a strong, positive correlation at zero lag with a cross-correlation coefficient of 0.873m, where 1.0 is a total positive correlation. This implies that there is some variation between the two signals, but as the two are shifted relative to one another, there is less correlation. This ultimately implies that the signals are consistent with one another.

The top row of Figure 6.16 are the cross correlations for the x and y velocity respectively. In each, the maximum zero-lag cross correlation coefficient is 0.604 and 0.545, indicating there is correlation between the signals. The wider bands as the lag is shifted off of zero indicate there is mismatch in the data rate for either of the signals that is causing them to have a high correlation at a nonzero lag. This spike at zero still holds statistical significance as it indicates that there is a similarity in waveform shape between the signals with no shift in time.

6.3.3 Extrapolation to More Degrees of Freedom

The method employed in the kinematic analysis is readily expandable to robots with N wheel modules or branches in that the other branches are considered to be more parallel connections between the ground and the center of the robot [37]. While the size of the total system grows with the addition of more wheels, it can be seen that the complexity of the problem remains the same as each additional wheel, assuming it is the same single link wheel mechanism as with the robot in this paper; the number of 2×2 systems increases but the size of the systems remains the same. Even if the additional wheels have some form of extra link between the center of the robot and the wheel contact point, the system will grow in complexity proportional to the number of links and would present itself as more terms in the velocity equations and would increase the domain of solutions to the system (which could then be limited by other factors or parameters).

Being that this method uses first order dynamics to construct a system of equations that relates the velocity of a single wheel structure to the velocity of the center of the robot, it is possible to use the construction of moving reference frames in order to capture the motion of parts of the robot with respect to the chassis or some other stationary part of the robot. In describing a reference frame as the addition of some linear velocity term (either a linear velocity or the effect of a rotation at some distance), it becomes as simple as subtracting the non-joint term to create some augmented robot twist that has now taken into account the motion of the parts of the robot so that the remaining velocity can be made up by the motion of the wheel module.

6.4 Contribution of Work

This work is an expansion on pre-existing inverse kinematics methods for mobile robots that is tolerant to singularities that would arise from degenerate wheel structures being the

primary form of locomotion for the robot. This analytical approach allows for a closed form description of robot configuration parameters for an otherwise unsolvable kinematic system. The direct solution provided in this work does not have the singularity problems the inverse-matrix based solution does.

This work has been published in *Mechanism and Machine Theory*, [92].

CHAPTER 7
CONCLUDING REMARKS

In this thesis, degenerate mobile robot inverse kinematics were analyzed and the underlying concept of stabilizing a system with flexible modes is addressed. A candidate degenerate mobile robotic platform is introduced and its inverse kinematics were solved analytically so as to avoid numerical singularity found with matrix methods. These inverse kinematics were experimentally validated using motion capture experiments. Introduced as a composite mobile manipulator system, the mobile robotic base, dynamically, is abstracted away to an equivalent flexible base. The robustness of the manipulator is described using two metrics: the normalized-coprime factor stability margin and the modal passivity index. The former describes energy transmission through a balanced description of the system and therefore can determine a system's resilience to external disturbance. The latter is a measure of a particular mode's passivity. Between these two values it is shown that it is possible to determine postures that are robust to the induced oscillations in the flexible base.

Numerical experiments highlighted the gap in knowledge regarding the application of these metrics to manipulator systems. As such, the conditions defining when a system is in a robust posture were found, as well as those to remain in a robust posture. A constant value for rigid systems is found for the NCF stability margin and found that for SISO flexible systems this is the minimum value for minimum phase systems. Application of these metrics to a manipulator system reveals the utility of redundancy in the composite system that allows the system to pose itself in a more robust posture while maintaining the same end-point position.

The research described in this dissertation can be summarized in the list below.

- Theory surrounding the minimum NCF stability margin for robust configurations of the the manipulator. Conditions that generate the robust configuration are quanti-

fied as well as perturbations in the end-point that keep the manipulator in a robust posture. The NCF stability margin for rigid systems is proven to be constant to be equal to $\frac{1}{\sqrt{4+2\sqrt{2}}}$. This value was shown to be the minimum NCF stability margin for flexi-rigid systems in robust postures. The special case involving simultaneous diagonalization of modes in the system is presented and analyzed, with consideration for asymmetrical rigid modes.

- Several case studies highlighting the use of the aforementioned properties were presented for the RR, RP, and parallel-drive manipulators mounted upon flexible bases. The case of a flexible link within a rigid system is explained to never be passive due to internal dynamics.

- Stability margins were used with Jacobian inverse nullspace augmentation to pose the mobile manipulation system in a locally optimal posture so it can complete its positioning task while maintaining low amounts of induced base oscillation. Closed form solutions for the gradient of the modal space stability index with respect to the state variables are derived and used for the objective function in the nullspace augmentation.

- The transformable degenerate pseudo omnidirectional wheeled mobile robotic platform is introduced and it its shown that existing matrix methods will not solve its inverse kinematics. Due to this the inverse kinematics are solved analytically and used to define the necessary wheel states to satisfy the desired twist. Motion capture experiments are performed to validate the generated motion commands given to the platform. A high cross correlation between the captured robot motion and provided velocity commands shows that the generated inverse kinematics are valid solutions.

7.1 Future Work

7.1.1 Extensions to Other Systems

The context of the work in this thesis focuses on the aggregate flexible-rigid system generated through mounting a rigid system upon a wheeled mobile base (presumably with some suspension, thus creating the flexible base). The redundancy here is provided by the wheeled base, and in this work we showed that we can use this to better pose the manipulator to increase its robustness. Extending this concept to other systems would look at systems with virtual elastic bases: namely a manipulator on a UAV or a manipulator on satellite. The virtual flexibility originates from position control of the base in space; as the base is perturbed either by the environment or by excited motion, the position controller will correct it, introducing an oscillation through the system akin to the base flexibility seen in this work. While the frequency of the virtual flexibility of this oscillation may already be outside the control bandwidth for the manipulator, there are some situations where this may not be the case and control like this would be valuable. Investigation as to the validity of the modally decomposed transfer function for this application would need to be conducted as the dynamics for these systems are inherently nonlinear.

7.1.2 Extensions to Motion Control

Recent work in motion planning uses Riemmanian geometry to generate an optimal path through a known environment in accordance with various policies [93, 94]. These policies can be anything from a cost function to a potential field relaying obstacles in the local environment. Implementing the stability margins presented in this work along with RMP will allow for the optimal tracking through the "robustness field" in a similar fashion to the Jacobian inverse nullspace augmentation work conducted with the remote excavation system, but will enable the use of other control schemes aside from the Jacobian inverse control.

7.1.3 Further Analysis of Flexible System NCF Stability Margin Solution

The work conducted in this thesis took a numerical approach to the solution of the flexible system NCF stability margin. For the SISO case a good approximation was found and was used to get an idea of how the solution looked, however there was no real progress made for the MIMO case. The NCF stability margin requires the solution of two algebraic Riccati equations and the quadratic nature of these equations makes a closed form solution often difficult. For that it may be beneficial to look at the geometry of the equations [95] or revisiting any of the invariant subspace solution methods using Sylvester's Law of Inertia [96, 97] to help estimate the spectra of the Hermitian (perhaps even the Gershgorin circle theorem may be of assistance).

Appendices

APPENDIX A

ROBUST STABILITY MARGIN BY NORMALIZED COPRIME FACTOR DESCRIPTIONS

Given a plant $\tilde{\mathbf{P}}(\mathbf{s}) \triangleq k_r\mathbf{P} = \tilde{\mathbf{M}}^{-\mathbf{1}}\tilde{\mathbf{N}}$, where k_r is a scalar servo gain ($k_r > 0$) (as k_r increases, the analysis is performed with higher gain). A system with variation of its left coprime factors is considered. The transfer function is defined as: $\mathbf{T}_{zw}(s) \triangleq \begin{bmatrix} \mathbf{K}_c(s) \\ \mathbf{I} \end{bmatrix} \left(\mathbf{I} + \tilde{\mathbf{P}}(s)\mathbf{K}_c(s)\right)^{-1}) \begin{bmatrix} \mathbf{I} & \tilde{\mathbf{P}}(s) \end{bmatrix}$, where $\mathbf{K}_c$ is the stabilizing controller for $\tilde{\mathbf{P}}(s)$. The robust stability margin, ε_{max}, is

$$\varepsilon_{max} \triangleq \left(\inf_{\mathbf{K}_c(s)} \left\| \mathbf{T}_{zw}(s) \right\|_\infty \right)^{-1} = \sqrt{1 - \left\| \begin{bmatrix} \tilde{\mathbf{N}} & \tilde{\mathbf{M}} \end{bmatrix} \right\|_H^2} \tag{A.1}$$

where $\|A\|_H$ is the Hankel norm of A. Where robustness to modeling error is high when ε_{max} is large [59].

APPENDIX B

NUMERICAL VERIFICATION OF SELECTED RESULTS

B.1 Verification of Rigid System NCF Stability Margin

The presented solutions in chapter 3 for the GCARE and GFARE can easily be verified using the icare command in Maltab (Mathworks). Consider the following cases of rigid manipulator system with with parameters

1. $\boldsymbol{R}_0 = 4$, with $\boldsymbol{F} = \sqrt{\boldsymbol{R}_0}^{-1} = 0.5$
2. $\boldsymbol{R}_0 = \begin{bmatrix} 23.6758 & -5.0429 \\ -5.0429 & 4.6265 \end{bmatrix}$, with $\boldsymbol{F} = \sqrt{\boldsymbol{R}_0}^{-1} = \begin{bmatrix} 0.220286 & 0.0805138 \\ 0.0805138 & 0.524423 \end{bmatrix}$

B.1.1 Case 1: SISO

Given the system structure in (Equation 3.41)-(Equation 3.45), the state space representation of the SISO case is:

$$\boldsymbol{A} = \begin{bmatrix} 0 & 1 \\ 0 & 0 \end{bmatrix} \tag{B.1}$$

$$\boldsymbol{B} = \begin{bmatrix} 0 \\ 2 \end{bmatrix} \tag{B.2}$$

$$\boldsymbol{C} = \begin{bmatrix} 2 & 0 \end{bmatrix} \tag{B.3}$$

The solution to the GFARE, $\boldsymbol{Z}$, analytically is:

$$\boldsymbol{Z} = \begin{bmatrix} \sqrt{\mathbf{2}}\boldsymbol{F}(\boldsymbol{R}_0\boldsymbol{R}_0^T)^{\frac{1}{4}}\boldsymbol{F}^T & \boldsymbol{F}(\boldsymbol{R}_0\boldsymbol{R}_0^T)^{\frac{1}{2}}\boldsymbol{F}^T \\ \boldsymbol{F}(\boldsymbol{R}_0\boldsymbol{R}_0^T)^{\frac{1}{2}}\boldsymbol{F}^T & \sqrt{\mathbf{2}}\boldsymbol{F}(\boldsymbol{R}_0\boldsymbol{R}_0^T)^{\frac{3}{4}}\boldsymbol{F}^T \end{bmatrix} = \begin{bmatrix} 0.70711 & 1.0 \\ 1.0 & 2.8284 \end{bmatrix} \tag{B.4}$$

Using the icare command:

$$[\boldsymbol{Z}_{icare}, \sim, \sim] = \text{icare}(\boldsymbol{A}^T, [], \boldsymbol{B}\boldsymbol{B}^T, [], [], [], -\boldsymbol{C}^T\boldsymbol{C}) \tag{B.5}$$

$$\boldsymbol{Z}_{icare} = \begin{bmatrix} 0.70711 & 1.0 \\ 1.0 & 2.8284 \end{bmatrix} \tag{B.6}$$

And finally, the matrix sign function [65]. Defining the Hamiltonian matrix for the GFARE and its matrix sign:

$$\begin{aligned} \boldsymbol{H}_f &= \begin{bmatrix} \boldsymbol{A}^T & -\boldsymbol{C}^T\boldsymbol{C} \\ -\boldsymbol{B}\boldsymbol{B}^T & -\boldsymbol{A} \end{bmatrix} \\ &= \begin{bmatrix} 0 & 0 & -4.0 & 0 \\ 1.0 & 0 & 0 & 0 \\ 0 & 0 & 0 & -1.0 \\ 0 & -4.0 & 0 & 0 \end{bmatrix} \end{aligned} \tag{B.7}$$

$$\text{sign}(\boldsymbol{H}_f) = \boldsymbol{H}_f \left(\sqrt{\boldsymbol{H}_f^2}\right)^{-1} = \begin{bmatrix} \boldsymbol{S}_{f11} & \boldsymbol{S}_{f12} \\ \boldsymbol{S}_{f21} & \boldsymbol{S}_{f22} \end{bmatrix} \tag{B.8}$$

The solution to the GFARE is given by [98] (Thm 2.2):

$$\boldsymbol{Z}_{sign} = -\boldsymbol{S}_{f21}\left(\boldsymbol{S}_{f22} - \boldsymbol{I}\right))^{-1} = \begin{bmatrix} 0.70711 & 1.0 \\ 1.0 & 2.8284 \end{bmatrix} \tag{B.9}$$

It is clear that these three solutions match for the SISO case. Repeating the above for the GCARE:

$$\boldsymbol{X} = \begin{bmatrix} \sqrt{\boldsymbol{2}}\boldsymbol{F}^{-T}(\boldsymbol{R}_0\boldsymbol{R}_0^T)^{-\frac{1}{4}}\boldsymbol{F}^{-1} & \boldsymbol{F}^{-T}(\boldsymbol{R}_0\boldsymbol{R}_0^T)^{-\frac{1}{2}}\boldsymbol{F}^{-1} \\ \boldsymbol{F}^{-T}(\boldsymbol{R}_0\boldsymbol{R}_0^T)^{-\frac{1}{2}}\boldsymbol{F}^{-1} & \sqrt{\boldsymbol{2}}\boldsymbol{F}^{-T}(\boldsymbol{R}_0\boldsymbol{R}_0^T)^{-\frac{3}{4}}\boldsymbol{F}^{-1} \end{bmatrix} = \begin{bmatrix} 2.8284 & 1.0 \\ 1.0 & 0.70711 \end{bmatrix} \tag{B.10}$$

Using the icare command:

$$[\boldsymbol{X}_{icare}, \sim, \sim] = \text{icare}(\boldsymbol{A}, [], \boldsymbol{C}^T\boldsymbol{C}, [], [], [], -\boldsymbol{B}\boldsymbol{B}^T) \tag{B.11}$$

$$\boldsymbol{X}_{icare} = \begin{bmatrix} 2.8284 & 1.0 \\ 1.0 & 0.70711 \end{bmatrix} \tag{B.12}$$

Using the matrix sign:

$$\begin{aligned} \boldsymbol{H}_c &= \begin{bmatrix} \boldsymbol{A} & -\boldsymbol{B}\boldsymbol{B}^T \\ -\boldsymbol{C}^T\boldsymbol{C} & -\boldsymbol{A}^T \end{bmatrix} \\ &= \begin{bmatrix} 0 & 1.0 & 0 & 0 \\ 0 & 0 & 0 & -4.0 \\ -4.0 & 0 & 0 & 0 \\ 0 & 0 & -1.0 & 0 \end{bmatrix} \end{aligned} \tag{B.13}$$

$$\text{sign}(\boldsymbol{H}_c) = \boldsymbol{H}_c\left(\sqrt{\boldsymbol{H}_c^2}\right)^{-1} = \begin{bmatrix} \boldsymbol{S}_{c11} & \boldsymbol{c}\boldsymbol{S}_{12} \\ \boldsymbol{S}_{c21} & \boldsymbol{S}_{c22} \end{bmatrix} \tag{B.14}$$

$$\boldsymbol{X}_{sign} = -\boldsymbol{S}_{c21}\left(\boldsymbol{S}_{c11} - \boldsymbol{I}\right))^{-1} = \begin{bmatrix} 2.8284 & 1.0 \\ 1.0 & 0.70711 \end{bmatrix} \tag{B.15}$$

B.1.2 Case 2: MIMO

Repeating the above section for the new system defined by the MIMO rigid mode and distribution factor in case 2:

$$\boldsymbol{A} = \begin{bmatrix} 0 & 0 & 1.0 & 0 \\ 0 & 0 & 0 & 1.0 \\ 0 & 0 & 0 & 0 \\ 0 & 0 & 0 & 0 \end{bmatrix} \tag{B.16}$$

$$\boldsymbol{B} = \begin{bmatrix} 0 & 0 \\ 0 & 0 \\ 4.8094 & -0.73838 \\ -0.73838 & 2.0202 \end{bmatrix} \tag{B.17}$$

$$\boldsymbol{C} = \begin{bmatrix} 4.8094 & -0.73838 & 0 & 0 \\ -0.73838 & 2.0202 & 0 & 0 \end{bmatrix} \tag{B.18}$$

The solutions for the GCARE and GFARE become:

$$\boldsymbol{Z} = \begin{bmatrix} 0.31153 & 0.11386 & 1.0 & 0 \\ 0.11386 & 0.74165 & 0 & 1.0 \\ 1.0 & 0 & 6.8016 & -1.0442 \\ 0 & 1.0 & -1.0442 & 2.857 \end{bmatrix} \tag{B.19}$$

$$\boldsymbol{Z}_{icare} = \begin{bmatrix} 0.31153 & 0.11386 & 1.0 & 0 \\ 0.11386 & 0.74165 & 0 & 1.0 \\ 1.0 & 0 & 6.8016 & -1.0442 \\ 0 & 1.0 & -1.0442 & 2.857 \end{bmatrix} \tag{B.20}$$

$$\boldsymbol{Z}_{sign} = \begin{bmatrix} 0.31153 & 0.11386 & 1.0 & 0 \\ 0.11386 & 0.74165 & 0 & 1.0 \\ 1.0 & 0 & 6.8016 & -1.0442 \\ 0 & 1.0 & -1.0442 & 2.857 \end{bmatrix} \tag{B.21}$$

$$\boldsymbol{X} = \begin{bmatrix} 6.8016 & -1.0442 & 1.0 & 0 \\ -1.0442 & 2.857 & 0 & 1.0 \\ 1.0 & 0 & 0.31153 & 0.11386 \\ 0 & 1.0 & 0.11386 & 0.74165 \end{bmatrix} \tag{B.22}$$

$$\boldsymbol{X}_{icare} = \begin{bmatrix} 6.8016 & -1.0442 & 1.0 & 0 \\ -1.0442 & 2.857 & 0 & 1.0 \\ 1.0 & 0 & 0.31153 & 0.11386 \\ 0 & 1.0 & 0.11386 & 0.74165 \end{bmatrix} \tag{B.23}$$

$$\boldsymbol{X}_{sign} = \begin{bmatrix} 6.8016 & -1.0442 & 1.0 & 0 \\ -1.0442 & 2.857 & 0 & 1.0 \\ 1.0 & 0 & 0.31153 & 0.11386 \\ 0 & 1.0 & 0.11386 & 0.74165 \end{bmatrix} \tag{B.24}$$

As demonstrated, there is a consistency in solution between three different solution methods of the ARE's for the rigid system, thus indicating the validity of the analytical solution.

B.2 Bode Plots for In-Phase Systems

The inclusion of an in-phase flexible mode will improve performance in a system beyond that of a purely rigid system. This is demonstrated clearly in the NCF stability margin (Figure 3.3). Furthermore, it is also demonstrable in a classical controls sense. Given an SISO flexible system $P(s)$:

$$P(s) = \frac{\kappa_0}{s^2} + \frac{\kappa_1}{s^2 + 2\zeta\omega_n s + \omega_n^2} \tag{B.25}$$

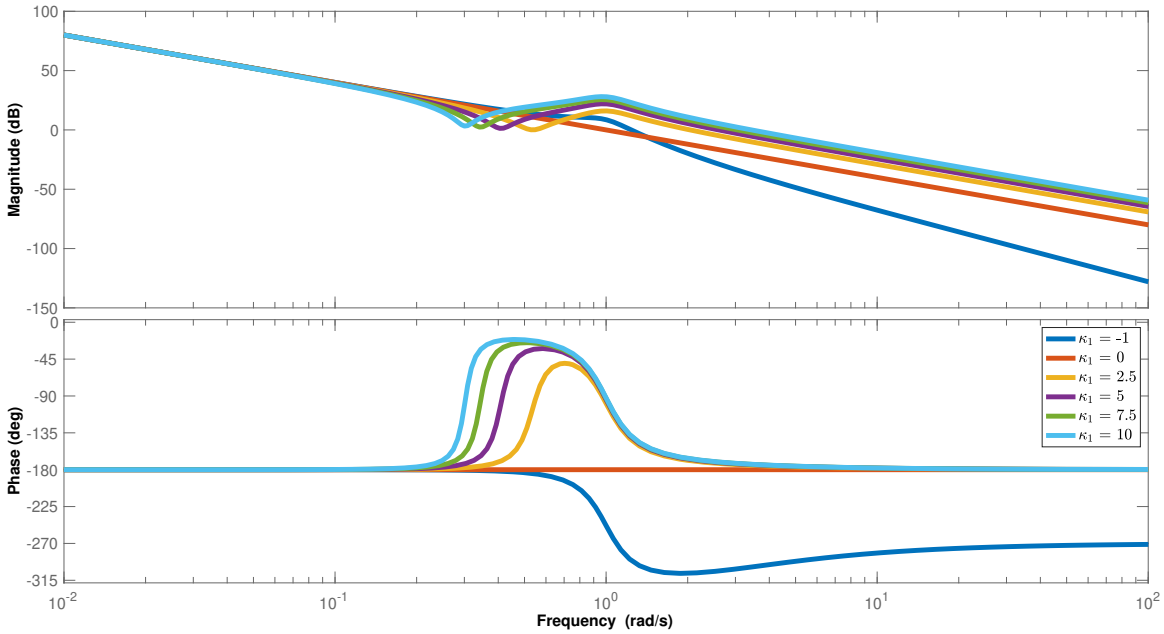

Figure B.1: Bode plots for SISO system with single flexible mode and parameters: $\kappa_0 = 1$; $\omega = 1$; $\zeta = 0.2$.

κ_1	ϕ_m
-1	-110.7801
0	0
2.5	11.0286
5	8.728
7.5	7.4609
10	6.6286

Table B.1: Phase Margin For $\kappa_0 = 1$; $\omega = 1$; $\zeta = 0.2$

with parameters: $\kappa_0 = 1$; $\omega = 1$; $\zeta = 0.2$, the bode plots for a range of κ_1 can be generated, shown in Figure B.1. With the phase margins of each of the system shown in Table B.1. Looking at the phase margins of each system, when $\kappa_1 > 0$, indicating an in-phase flexible mode, it has positive phase margin. This means that the in-phase flexible system can sustain more feedback gain than the rigid system before instability occurs. Conversely, the inclusion of an out-of-phase flexible mode will always be unstable when exposed to negative feedback.

APPENDIX C

DERIVATION OF GRADIENT OF MODAL STABILITY INDEX

Given the classic eigenvalue problem $\mathbf{G}\nu = \lambda\nu$, where $\mathbf{G} = \mathbf{R}_i + \mathbf{R}_i^T$, we can take the gradient of both sides with respect to $\mathbf{q}_B$: $\frac{\partial \mathbf{G}}{\partial \mathbf{q_B}}\nu + \mathbf{G}\frac{\partial \nu}{\partial \mathbf{q_B}} = \nu\frac{\partial \lambda}{\partial \mathbf{q_B}} + \lambda\frac{\partial \nu}{\partial \mathbf{q_B}}$. Enforcing ν to be a unit eigenvector, we can use the orthogonality of $\frac{\partial \nu}{\partial \mathbf{q_B}}$ and ν to reduce the number of terms in the equation. Taking the inner-product of each side with $\frac{\partial \nu}{\partial \mathbf{q_B}}$ yields $\frac{\partial \lambda}{\partial \mathbf{q_B}} = \left\langle \nu, \frac{\partial \mathbf{G}}{\partial \mathbf{q_B}}\nu \right\rangle$.

REFERENCES

[1] T. Jacobs, M. Hesse, and A. Verl, "Evaluation of wheel mechanisms for omnidirectional robot undercarriages," in *ISR/Robotik 2014; 41st International Symposium on Robotics*, Jun. 2014, pp. 1–7.

[2] Y. Yamada, K. Ookoudo, and Y. Komura, "Layout optimization of manufacturing cells and allocation optimization of transport robots in reconfigurable manufacturing systems using particle swarm optimization," vol. 2, Dec. 2003, 2049–2054 vol.2.

[3] S. Yamamoto, "Development of inspection robot for nuclear power plant," in *Robotics and Automation, 1992. Proceedings., 1992 IEEE International Conference on Robotics and Automation*, IEEE, 1992, pp. 1559–1566.

[4] IAEA. (May 2017). "Robotics challenge 2017."

[5] A. van der Schaft, *L2-Gain and Passivity Techniques in Nonlinear Control*. Springer International Publishing, 2017, p. 7.

[6] B. Anderson, "The small-gain theorem, the passivity theorem and their equivalence," *Journal of the Franklin Institute*, vol. 293, no. 2, pp. 105–115, Feb. 1972.

[7] W. M. Griggs, B. D. O. Anderson, and A. Lanzon, "A "mixed" small gain and passivity theorem for an interconnection of linear time-invariant systems," in *2007 European Control Conference (ECC)*, IEEE, Jul. 2007.

[8] N. Kottenstette and P. J. Antsaklis, "Relationships between positive real, passive dissipative, & positive systems," in *Proceedings of the 2010 American Control Conference*, IEEE, Jun. 2010.

[9] N. Kottenstette, M. J. McCourt, M. Xia, V. Gupta, and P. J. Antsaklis, "On relationships among passivity, positive realness, and dissipativity in linear systems," *Automatica*, vol. 50, no. 4, pp. 1003–1016, 2014.

[10] M. Vidyasagar, *Nonlinear Systems Analysis*. Society for Industrial and Applied Mathematics, Jan. 2002.

[11] K. ONO, "Design methodology to stabilize the natural modes of vibration of a swing-arm positioning mechanism," *ASME Adv. Info. Storage Syst.*, vol. 4, pp. 343–359, 1992.

[12] T. Yoshikawa and J. Ueda, "Task priority based mode shaping method for in-phase design of flexible structures aiming at high speed and accurate positioning," in *Pro-*

ceedings 2001 ICRA. IEEE International Conference on Robotics and Automation (Cat. No.01CH37164), vol. 2, 2001, 1806–1812 vol.2.

[13] J. Lin, C. Lin, and H.-S. Lo, "Pseudo-inverse jacobian control with grey relational analysis for robot manipulators mounted on oscillatory bases," *Journal of Sound and Vibration*, vol. 326, no. 3-5, pp. 421–437, 2009.

[14] T. Aoki, Y. Yamashita, and D. Tsubakino, "Vibration suppression for mass-spring-damper systems with a tuned mass damper using interconnection and damping assignment passivity-based control," *International Journal of Robust and Nonlinear Control*, vol. 26, no. 2, pp. 235–251, 2015.

[15] V. Nguyen, J. Johnson, and S. Melkote, "Active vibration suppression in robotic milling using optimal control," *International Journal of Machine Tools and Manufacture*, vol. 152, p. 103 541, May 2020.

[16] Y. Khulief, "Vibration suppression in using active modal control," *Journal of Sound and Vibration*, vol. 242, no. 4, pp. 681–699, 2001.

[17] A. Tzes and S. Yurkovich, "An adaptive input shaping control scheme for vibration suppression in slewing flexible structures," *IEEE Transactions on Control Systems Technology*, vol. 1, no. 2, pp. 114–121, Jun. 1993.

[18] M. Toda, "An h/sub /spl infin// control-based approach to robust control of mechanical systems with oscillatory bases," *IEEE Transactions on Robotics and Automation*, vol. 20, no. 2, pp. 283–296, Apr. 2004.

[19] M. Sato and M. Toda, "Robust motion control of an oscillatory-base manipulator in a global coordinate system," *IEEE Transactions on Industrial Electronics*, vol. 62, no. 2, pp. 1163–1174, Feb. 2015.

[20] X. Wang and B. Hou, "Sliding mode control of a 2-dof manipulator with random base vibration based on modified exponential reaching law," *Vibroengineering PROCEDIA*, vol. 10, pp. 247–252, 2016.

[21] G. Song and H. Gu, "Active vibration suppression of a smart flexible beam using a sliding mode based controller," *Journal of Vibration and Control*, vol. 13, no. 8, pp. 1095–1107, 2007.

[22] J. Lin and C.-C. Lin, "Hybrid fuzzy position/force control by adaptive network-based fuzzy inference system for robot manipulator mounted on oscillatory base," *Journal of Vibration and Control*, vol. 21, no. 10, pp. 1930–1945, 2015. eprint: https://doi.org/10.1177/1077546313503360.

[23] G. Song and B. N. Agrawal, "Vibration suppression of flexible spacecraft during attitude control," *Acta Astronautica*, vol. 49, no. 2, pp. 73–83, Jul. 2001.

[24] L. Li, G. Song, and J. Ou, "Nonlinear structural vibration suppression using dynamic neural network observer and adaptive fuzzy sliding mode control," *Journal of Vibration and Control*, vol. 16, no. 10, pp. 1503–1526, 2010.

[25] Y. Fang, J. Fei, and T. Hu, "Adaptive backstepping fuzzy sliding mode vibration control of flexible structure," *Journal of Low Frequency Noise, Vibration and Active Control*, vol. 37, no. 4, pp. 1079–1096, 2018.

[26] A. Bowling and O. Khatib, "Design of macro/mini manipulators for optimal dynamic performance," in *Proceedings of International Conference on Robotics and Automation*, IEEE, vol. 1, 1997, pp. 449–454.

[27] R. McGregor and L. Oshinowo, "Flight 6a: Deployment and checkout of the space station remote manipulator system (ssrms)," in *Proceedings of the 6th International Symposium on Artificial Intelligence, Robotics and Automation in Space (i-SAIRAS)*, 2001.

[28] S. Doi, Y. Wakabayashi, T. Matsuda, and N. Satoh, "Jem remote manipulator system," *Journal of the Aeronautical and space Sciences Japan*, vol. 50, no. 576, pp. 7–14, 2002.

[29] T. Yoshikawa, K. Hosoda, T. Doi, and H. Murakami, "Dynamic trajectory tracking control of flexible manipulator macro-micro manipulator system," in *Proceedings of the 1994 IEEE International Conference on Robotics and Automation*, IEEE Comput. Soc. Press.

[30] S. Abiko and K. Yoshida, "An adaptive control of a space manipulator for vibration suppression," in *2005 IEEE/RSJ International Conference on Intelligent Robots and Systems*, 2005, pp. 2167–2172.

[31] J. English and A. Maciejewski, "On the implementation of velocity control for kinematically redundant manipulators," *IEEE Transactions on Systems, Man, and Cybernetics - Part A: Systems and Humans*, vol. 30, no. 3, pp. 233–237, May 2000.

[32] B. Siciliano, "Kinematic control of redundant robot manipulators: A tutorial," *Journal of intelligent and robotic systems*, vol. 3, no. 3, pp. 201–212, 1990.

[33] K. Cetin, E. Tatlicioglu, and E. Zergeroglu, "An extended jacobian-based formulation for operational space control of kinematically redundant robot manipulators with multiple subtask objectives: An adaptive control approach," *Journal of Dynamic Systems, Measurement, and Control*, vol. 141, no. 5, 2019.

[34] G. Campion, G. Bastin, and B. D'Andrea-Novel, "Structural properties and classification of kinematic and dynamic models of wheeled mobile robots," in *[1993] Proceedings IEEE International Conference on Robotics and Automation*, IEEE, 1993, pp. 462–469.

[35] G. Campion and W. Chung, "Wheeled robots," in *Springer Handbook of Robotics*, Springer Berlin Heidelberg, 2008, pp. 391–410.

[36] B. Deepak and D. Parhi, "Kinematic analysis of wheeled mobile robot," vol. 5, pp. 96–111, Jan. 2011.

[37] E. Jung, B. Yi, and W. Kim, "Kinematic analysis and motion planning for a planar multiarticulated omnidirectional mobile robot," *IEEE/ASME Transactions on Mechatronics*, vol. 20, no. 6, pp. 2983–2995, Dec. 2015.

[38] E.-j. Jung, B.-J. Yi, and W. K. Kim, "Motion planning algorithms of an omnidirectional mobile robot with active caster wheels," *Intelligent Service Robotics*, vol. 4, no. 3, pp. 167–180, Jul. 2011.

[39] Byung-Ju Yi and Whee Kuk Kim, "The kinematics for redundantly actuated omnidirectional mobile robots," in *Proceedings 2000 ICRA. Millennium Conference. IEEE International Conference on Robotics and Automation. Symposia Proceedings (Cat. No.00CH37065)*, vol. 3, Apr. 2000, 2485–2492 vol.3.

[40] P. F. Muir and C. P. Neuman, "Kinematic modeling of wheeled mobile robots," Ph.D. dissertation, 1987, pp. 281–340. eprint: https://onlinelibrary.wiley.com/doi/pdf/10.1002/rob.4620040209.

[41] P. Muir, "Modeling and control of wheeled mobile robots," Ph.D. dissertation, Carnegie Mellon University, Pittsburgh, PA, Jul. 1988.

[42] A. S. ConceiÇÃo, A. P. Moreira, and P. J. Costa, "Practical approach of modeling and parameters estimation for omnidirectional mobile robots," *IEEE/ASME Transactions on Mechatronics*, vol. 14, no. 3, pp. 377–381, Jun. 2009.

[43] C. P. Connette, A. Pott, M. Hagele, and A. Verl, "Control of an pseudo-omnidirectional, non-holonomic, mobile robot based on an icm representation in spherical coordinates," in *2008 47th IEEE Conference on Decision and Control*, Dec. 2008, pp. 4976–4983.

[44] C. P. Connette, C. Parlitz, M. Hagele, and A. Verl, "Singularity avoidance for overactuated, pseudo-omnidirectional, wheeled mobile robots," in *2009 IEEE International Conference on Robotics and Automation*, Jun. 2009, pp. 4124–4130.

[45] *Articulated Wheeled Robots: Exploiting Reconfigurability and Redundancy*, vol. ASME 2008 Dynamic Systems and Control Conference, Parts A and B, Dynamic Systems and Control Conference, Jun. 2009, pp. 653–660. eprint: https://asmedigitalcollection.asme.org/DSCC/proceedings-pdf/DSCC2008/43352/653/4573914/653_1.pdf.

[46] M. Itoh, K. Nonaka, and K. Sekiguchi, "Experimental verification of model predictive tracking and steering control for the vehicle equipped with coaxial steering mechanisms," in *2016 IEEE/SICE International Symposium on System Integration (SII)*, Dec. 2016, pp. 768–773.

[47] W. Kim, B.-J. Yi, and D. J. Lim, "Kinematic modeling of mobile robots by transfer method of augmented generalized coordinates," *Journal of Robotic Systems*, vol. 21, no. 6, pp. 301–322, 2004. eprint: https://onlinelibrary.wiley.com/doi/pdf/10.1002/rob.20015.

[48] L. Ferriere, B. Raucent, and G. Campion, "Design of omnimobile robot wheels," in *Proceedings of IEEE International Conference on Robotics and Automation*, vol. 4, 1996, 3664–3670 vol.4.

[49] K.-S. Byun and J.-B. Song, "Design and construction of continuous alternate wheels for an omnidirectional mobile robot," *Journal of Robotic Systems*, vol. 20, no. 9, pp. 569–579, 2003. eprint: https://onlinelibrary.wiley.com/doi/pdf/10.1002/rob.10107.

[50] H. Asama, M. Sato, H. Kaetsu, K. Ozaki, A. Matsumoto, and I. Endo, "Development of an omni-directional mobile robot with 3 dof decoupling drive mechanism," *Journal of the Robotics Society of Japan*, vol. 14, no. 2, pp. 249–254, 1996.

[51] W. Chung, C.-b. Moon, C. Jung, and J. Jin, "Design of the dual offset active caster wheel for holonomic omni-directional mobile robots," *International Journal of Advanced Robotic Systems*, vol. 7, Dec. 2010.

[52] T. Jacobs, C. Connette, M. Haegele, and A. Verl, "Design of wheel modules for non-holonomic, omnidirectional mobile robots in context of the emerging control problems," in *ROBOTIK 2012; 7th German Conference on Robotics*, Jun. 2012, pp. 1–4.

[53] M. Wada and H. H. Asada, "Design and control of a variable footprint mechanism for holonomic omnidirectional vehicles and its application to wheelchairs," *IEEE Transactions on Robotics and Automation*, vol. 15, no. 6, pp. 978–989, Dec. 1999.

[54] J. Ueda, R. Oya, T. Ogasawara, and T. Yoshikawa, "Solution of human-like redundant manipulator mounted on flexible body for task-space feedback control," in *Proceedings 2003 IEEE/ASME International Conference on Advanced Intelligent Mechatronics (AIM 2003)*, vol. 2, Jul. 2003, 1429–1434 vol.2.

[55] D. McFarlane and K. Glover, *Robust controller design using normalized coprime factor plant descriptions*, ser. Lecture notes in control and information sciences. Springer, 1990, pp. 54, 67, 182, ISBN: 9783540518518.

[56] J. E. Prussing, "The principal minor test for semidefinite matrices," *Journal of Guidance, Control, and Dynamics*, vol. 9, no. 1, pp. 121–122, Jan. 1986.

[57] C. D. Meyer, *Matrix analysis and applied linear algebra*. SIAM, Society for Industrial and Applied Mathematics, 2004, p. 566.

[58] J. C. Doyle, K. Glover, P. P. Khargonekar, and B. A. Francis, "State-space solutions to standard h/sub 2/ and h/sub infinity / control problems," *IEEE Transactions on Automatic Control*, vol. 34, no. 8, pp. 831–847, 1989.

[59] D. McFarlane and K. Glover, "A loop-shaping design procedure using h/sub infinity / synthesis," *IEEE Transactions on Automatic Control*, vol. 37, no. 6, pp. 759–769, 1992.

[60] K. Glover, "Model reduction: A tutorial on hankel-norm methods and lower bounds on l 2 errors," *IFAC Proceedings Volumes*, vol. 20, no. 5, pp. 293–298, Jul. 1987.

[61] K. Zhou, J. C. Doyle, K. Glover, *et al.*, *Robust and optimal control*. Prentice hall New Jersey, 1996, vol. 40, p. 559.

[62] R. Horn, *Matrix analysis*. Cambridge New York: Cambridge University Press, 2013, 439, Theorem 7.2.6, ISBN: 978-0-521-54823-6.

[63] V. Kučera, "A review of the matrix riccati equation," *Kybernetika*, vol. 09, no. 1, pp. 42–61, 1973.

[64] A. Laub, "A schur method for solving algebraic riccati equations," *IEEE Transactions on Automatic Control*, vol. 24, no. 6, pp. 913–921, 1979.

[65] C. S. Kenney and A. J. Laub, "The matrix sign function," *IEEE Transactions on Automatic Control*, vol. 40, no. 8, pp. 1330–1348, 1995.

[66] R. Byers, "Solving the algebraic riccati equation with the matrix sign function," *Linear Algebra and its Applications*, vol. 85, pp. 267–279, 1987.

[67] V. I. Hasanov, "Perturbation theory for linearly perturbed algebraic riccati equations," *Numerical Functional Analysis and Optimization*, vol. 35, no. 12, pp. 1532–1559, Aug. 2014.

[68] J.-g. Sun, "Perturbation theory for algebraic riccati equations," *SIAM Journal on Matrix Analysis and Applications*, vol. 19, no. 1, pp. 39–65, Jan. 1998.

[69] C. Chun-hui and C. Junhui, "Perturbation analysis for solutions of algebraic riccati equations," *Journal of Computational Mathematics*, vol. 6, no. 4, pp. 336–347, 1988.

[70] M. LiBretto and J. Ueda, "Evaluating the normalized coprime factor-based stability metric for rigid systems," under review in Journal of Dynamic Systems, Measurement and Control, 2021.

[71] J. Ueda and T. Yoshikawa, "Mode-shape compensator for improving robustness of manipulator mounted on flexible base," *IEEE Transactions on Robotics and Automation*, vol. 20, no. 2, pp. 256–268, 2004.

[72] V. Kumar, D. Rus, and S. Singh, "Robot and sensor networks for first responders," *IEEE Pervasive computing*, vol. 3, no. 4, pp. 24–33, 2004.

[73] D. P. Stormont, "Autonomous rescue robot swarms for first responders," in *CIHSPS 2005. Proceedings of the 2005 IEEE International Conference on Computational Intelligence for Homeland Security and Personal Safety, 2005.*, IEEE, 2005, pp. 151–157.

[74] J. De Greeff, T. Mioch, W. Van Vught, K. Hindriks, M. A. Neerincx, and I. Kruijff-Korbayová, "Persistent robot-assisted disaster response," in *Companion of the 2018 ACM/IEEE International Conference on Human-Robot Interaction*, 2018, pp. 99–100.

[75] J. Rantakokko, J. Rydell, P. Strömbäck, P. Händel, J. Callmer, D. Törnqvist, F. Gustafsson, M. Jobs, and M. Gruden, "Accurate and reliable soldier and first responder indoor positioning: Multisensor systems and cooperative localization," *IEEE Wireless Communications*, vol. 18, no. 2, pp. 10–18, 2011.

[76] H. I. Perez-Imaz, P. A. Rezeck, D. G. Macharet, and M. F. Campos, "Multi-robot 3d coverage path planning for first responders teams," in *2016 IEEE International Conference on Automation Science and Engineering (CASE)*, IEEE, 2016, pp. 1374–1379.

[77] K. Nagatani, S. Kiribayashi, Y. Okada, S. Tadokoro, T. Nishimura, T. Yoshida, E. Koyanagi, and Y. Hada, "Redesign of rescue mobile robot quince," in *2011 IEEE International Symposium on Safety, Security, and Rescue Robotics*, IEEE, 2011, pp. 13–18.

[78] J. Lee, B. Kim, D. Sun, C. Han, and Y. Ahn, "Development of unmanned excavator vehicle system for performing dangerous construction work," *Sensors*, vol. 19, no. 22, 2019.

[79] J.-s. Lee, B. Kim, D.-i. Sun, C.-s. Han, and Y.-h. Ahn, "Modelling and controlling unmanned excavation equipment on construction sites," in *Computing in Civil En-*

gineering 2019: Data, Sensing, and Analytics, American Society of Civil Engineers Reston, VA, 2019, pp. 305–311.

[80] D.-i. Sun, S.-k. Lee, Y.-s. Lee, S.-h. Kim, J. Ueda, Y. K. Cho, Y.-h. Ahn, and C.-s. Han, "Assessments of intuition and efficiency: Remote control of the end point of excavator in operational space by using one wrist," in *Computing in Civil Engineering 2019: Data, Sensing, and Analytics*, American Society of Civil Engineers Reston, VA, 2019, pp. 273–280.

[81] C. Chen and C. A. Desser, "Controlability and observability of composite systems," *IEEE Transactions on Automatic Control*, vol. 12, no. 4, pp. 402–409, Aug. 1967.

[82] J. Ueda and T. Ogasawara, "Global rac-measure for redundancy solution of human-like manipulator mounted on flexible body," in *2004 IEEE/RSJ International Conference on Intelligent Robots and Systems (IROS) (IEEE Cat. No.04CH37566)*, vol. 4, Sep. 2004, 3930–3935 vol.4.

[83] W. Chen, D. Wang, S. Z. Khong, and L. Qiu, "Phase analysis of MIMO LTI systems," in *2019 IEEE 58th Conference on Decision and Control (CDC)*, IEEE, Dec. 2019.

[84] T. T. Georgiou, "On the computation of the gap metric," *Systems & Control Letters*, vol. 11, no. 4, pp. 253–257, Oct. 1988.

[85] C. Cheah, C. Liu, and H. Liaw, "Stability of inverse jacobian control for robot manipulator," in *Proceedings of the 2004 IEEE International Conference on Control Applications, 2004.*, IEEE.

[86] J. J. Craig, *Introduction to robotics: mechanics and control*. Pearson, 2018.

[87] J. Ueda and T. Yoshikawa, "Robust arm configuration of manipulator mounted on flexible base," *IEEE transactions on robotics*, vol. 20, no. 4, pp. 781–789, 2004.

[88] M. LiBretto, Y. H. Ahn, C. S. Han, Y. K. Cho, and J. Ueda, "Configuration optimization for end-point stabilization of redundant manipulators with base flexibility," *ASME Letters in Dynamic Systems and Control*, vol. 1, no. 2, Apr. 2020.

[89] Y. Luan, H. Wang, X. Li, W. Xu, R. Huang, and J. Lv, "Design of motion control system for omnidirectional four-drive mobile robot," in *2019 IEEE 8th Joint International Information Technology and Artificial Intelligence Conference (ITAIC)*, May 2019, pp. 1409–1413.

[90] R. Beniak and T. Pyka, "The effect of an off-centered orientable wheel on motion characteristics of a mobile robot," in *2018 23rd International Conference on Methods Models in Automation Robotics (MMAR)*, 2018, pp. 780–784.

[91] V. Ramanathan, "Control of a wheeled mobile robot with centered orientable wheels and an offset alpha sensor for radiation surveying applications," 2020.

[92] M. LiBretto, Y. Qiu, E. Kim, K. Pluckter, N. S. Yuk, and J. Ueda, "Singularity-free solutions for inverse kinematics of degenerate mobile robots," *Mechanism and Machine Theory*, vol. 153, p. 103 988, Nov. 2020.

[93] N. D. Ratliff, J. Issac, and D. Kappler, "Riemannian motion policies," *CoRR*, vol. abs/1801.02854, 2018. arXiv: 1801.02854.

[94] C.-A. Cheng, M. Mukadam, J. Issac, S. Birchfield, D. Fox, B. Boots, and N. D. Ratliff, "Rmpflow: A computational graph for automatic motion policy generation," *CoRR*, vol. abs/1811.07049, 2018. arXiv: 1811.07049.

[95] M. A. Shayman, "Geometry of the algebraic riccati equation, part i," *SIAM Journal on Control and Optimization*, vol. 21, no. 3, pp. 375–394, May 1983.

[96] J. Dancis, "A quantitative formulation of sylvester's law of inertia. III," *Linear Algebra and its Applications*, vol. 80, pp. 141–158, Aug. 1986.

[97] J. Carrell, *Groups, matrices, and vector spaces : a group theoretic approach to linear algebra*. New York, NY: Springer, 2017, ISBN: 978-0-387-79428-0.

[98] L. Linzhang and C. Pearce, "On the matrix-sign-function method for solving algebraic riccati equations," *Applied mathematics and computation*, vol. 86, no. 2-3, pp. 157–170, 1997.

VITA

Michael was born in New York and grew up in a Long Island suburb. From a young age he was indoctrinated into the world of science-fiction and was fascinated with things that moved seemingly on their own. Consumed by that magic, Michael took every chance he got to learn about the development and control of electromechanical systems.